Changes in clouds over the four decades using PATMOS-x v6.0: radiative effects and controlling factors.

by

Jongjin Seo

A dissertation submitted in partial fulfillment of

The requirements for the degree of

Doctor of Philosophy

(Atmospheric and Oceanic Sciences)

at the

UNIVERSITY OF WISCONSIN-MADISON

2025

Date of final oral examination: 5/7/2025

The dissertation is approved by the following members of the Final Oral Committee:

Tristan L'Ecuyer, Professor, Atmospheric and Oceanic Sciences

Foster Michael, Professor, Atmospheric and Oceanic Sciences

Daniel Vimont, Professor, Atmospheric and Oceanic Sciences

Ángel Adames Corraliza, Professor, Atmospheric and Oceanic Sciences

Daniel Wright, Professor, Civil and Environmental Engineering

Abstract

Changes in clouds over the four decades using PATMOS-x v6.0: radiative effects and controlling factors.

by Jongjin Seo

Satellite-Based global cloud data records are crucial for understanding the impact of regional weather changes and global climate variations due to the direct and indirect radiative forcing of clouds. In this dissertation, the PATMOS-x version 6.0 dataset, developed through a collaboration between NOAA National Center for Environmental Information and the University of Wisconsin-Madison, was used to investigate long-term changes in maritime clouds between 60°S to 60°N. This dataset provides reliable climate records from NOAA's POES and EUMETSAT's MetOp satellite series. To account for orbital drift and varying local overpass times between satellites, monthly mean cloud fractions were calculated using a generalized additive model with backfitting and observational weighting. The results show a decreasing trend in mean fractional cloudiness of 0.86% per decade, with the most significant decline occurring over the central equatorial Pacific Ocean at a rate of 4% per decade. In contrast, increasing trends in water clouds over the southeastern Pacific Ocean as well as midlatitude and in ice clouds over western Pacific Ocean were observed. These changes in cloud fractions are closely linked to variations in cloud top heights. Cloud top heights have increased over western Pacific Ocean at a rate of 0.4 km per decade due to increases in ice clouds while decreasing cloud top heights were observed in the southeastern Pacific Ocean and other marine stratocumulus dominated regions. Such variations in cloud fraction and cloud top heights significantly contribute to cloud radiative effects, influencing Earth's radiation budget. Recent studies suggest that ongoing global warming is associated with a reduction in planetary albedo, primarily driven by a decline in global cloud fractions. However, some regions, such as the southeastern Pacific Ocean, have shown increasing albedo, enhancing solar radiation reflection and mitigating surface warming. This trend in albedo is attributed to a rise in low cloud cover, which plays a key role in increasing albedo. For a more comprehensive understanding of the physical processes driving cloud formation in this region, this study utilizes two satellite-based observational datasets (PATMOS-x v6.0 and CERES EBAF), both of which show an increase in total cloud fractions (0.97% per decade), particularly a rise in water clouds

(1.63% per decade). This increase in strongly correlated with a strengthening of cloud induced cooling effects (−1.91 Wm^{-2} per decade). By applying the ridge regression method and the CCFs framework to the ERA5 reanalysis dataset, the analysis indicates that these changes are primarily driven by an increase in estimated inversion strength at a rate of 0.30 K per decade, reflecting enhanced atmospheric stability. This stabilization is attributed to a decrease in surface temperature (−0.10 K per decade) and an increase in atmospheric temperature at 700 hPa (0.21 K per decade).

Acknowledgments

I couldn’t finish this long journey alone, and I have so many people to thank. First and foremost, a huge thank you to my research advisor, Michael J. Foster, whose invaluable guidance and unwavering support have enabled me to explore my curiosity about climate change through satellite-based observations. Second, I must thank you to my academic advisor, Tristan L’Ecuyer, whose guidance has been invaluable in helping me navigate this journey. Also, I’d like to thank Coda Phillips and Andrew K. Heidinger for their endless patience in answering my scientific questions and lots of support to solve them.

Thank you to my committee members, Daniel Vimont, Ángel F. Adames Corraliza, and Daniel Wright. Thank you for believing in me and trusting that I would be able complete this work. I am grateful for the advice and feedback you’ve all provided, and I am most grateful for the fact that you all choose to support me and my research path, unconventional through I wanted it to be.

A huge thank you to everyone in AOS community and PATMOS-x science team who has supported me over my time in Madison. I also say thanks to Jonathan Gero, Timothy Wagner, and David Turner, who were my research advisors for my M.S. degree, helped me begin my life in Madison and supported me in completing my M.S. degree. To my AOS friends, Jerrold, Shane, Patrick, Terry, Meggi, and Doreen, thank you for your support and community these last few years. Especially, it was a joy to play tennis with Jerrold for many years. I’d like to thank the PATMOS-x science team, Tim, Steve, and Dave, for sharing their knowledge in remote sensing and climate.

I also want to thank to my Korean friends, Esther, Jaehyung, Jinwoo, and Minsoo, who helped me settle down in Madison. Especially, I cherish the great memories with Minsoo, including fishing, camping, and going on road trips together. Also, I’d like to thanks to my Korean friends in South Korea, Yuna, Jiwoo, HyunYong, HwaEun, LiKuem, Hyeonuk, SeungYeong, SeungKyun, and Hyoin. Last, I am deeply grateful to my family, TaeYeol, Gwangsuk, Miri, Mihyeon, JaeWon, Daegeun, Rakyeol, and Hunmin for their endless support and love.

Contents

List of Figures

List of Tables

Abbreviations

ACHA: AWG Cloud Height Algorithm

AR6: Sixth Assessment Report

AVHRR: Advanced Very High Resolution Radiometer

AWG: Algorithm Working Group

CALIOP: Cloud-Aerosol Lidar with Orthogonal Polarization

CALIPSO: Cloud-Aerosol Lidar and Infrared Pathfinder Satellite Observation

CCF: Cloud Controlling Factors

CDR: Climate Data Record

CERES: Clouds and the Earth’s Radiant Energy System Energy Balanced and Filled

CIMMS: Cooperative Institute for Meteorological Satellite Studies

CLARA-A3: the third edition of CM SAF cLoud Albedo, and surface Radiation dataset

CLAVR-x: Clouds from AVHRR Extended

CM SAF: EUMETSAT Satellite Application Facility on Climate Monitoring

CMIP6: Coupled Model Intercomparison Project Phase 6

COD: Cloud Optical Detph

CRE: Cloud Radiative Effect

DCOMP: Daytime Cloud Optical and Microphysical Properties

ECM: Enterprise Cloud Mask

ECMWF: European Centre for Medium-Range Weather Forecasts

EEI: Earth’s Energy Imbalance

EIS: Esitmated Inversion Strength

ENSO: El Niño-Southern Oscillation

ERA5: ECMWF Reanalysis v5

ERSST: Extended Reconstructed Sea Surface Temperature

GAM: Generalized Additive Model

GEOS: Goddard Earth Observing System

GMAO: Global Modeling and Assimilation Office

HadISST: Hadley Centre Global Sea Ice and Sea Surface Temperature

HIRS: High-Resolution Infrared Radiation Sounder

IESA: Integrated Earth System Analysis

IPCC: Intergovernmental Panel on Climate Change

ITCZ: Inter Tropical Convergence Zone

LTS: Lower Troposphere Stability

MBL: Marine Boundary Layer

MERRA-2: Modern-Era Retrospective analysis for Research and Application Version 2

NASA: National Aeronautics and Space Administration

NCAR: National Center for Atmospheric Research

NCEP: National Center for Environmental Prediction

NESDIS: National Environmental Satellite, Data, and Information Service

NOAA: National Oceanic and Atmospheric Administration

OLR: Outgoing Longwave Radiation

ORA: Office of Research and Applications

OSR: Outgoing Shortwave Radiation

PATMOS-x: Pathfinder Atmospheres-Extended

POES: Polar Operational Environmental Satellites

RMSE: Root Mean Squared Error

Soumi NPP: Soumi National Polar-orbiting Partnership

SST: sea surface temperature

TOA: Top-Of-Atmosphere

VIIRS: Visible Infrared Imaging Radiometer Suite

Chapter 1

Introduction

Clouds are a key component in shaping both regional weather patterns as well as global climate change though their direct and indirect effects (Ramanathan et al., 1989; Harrison et al., 1990) and it has been highlighted in the Intergovernmental Panel on Climate Change (IPCC) Sixth Assessment Report (AR6) in 2023. Changes in clouds including phase, height, and thickness can impact components of the atmosphere and environment such as thermodynamic structure, precipitation, regional weather pattern, interaction with aerosol, and ozone formation (Monod and Carlier, 1999; Matsui et al., 2004; Li et al., 2011; Tao et al., 2012; Rosenfeld et al., 2014; Bony et al., 2016). Moreover, clouds play discernible roles in the Earth's radiative balance through their radiative characteristics, called cloud radiative effects (CREs), which include heat exchange in the atmosphere between clouds and the surface by absorption and emission, in addition to regulating solar energy by reflecting and scattering, as shown in Figure 1.1 (Arking, 1991; Chen et al., 2000).

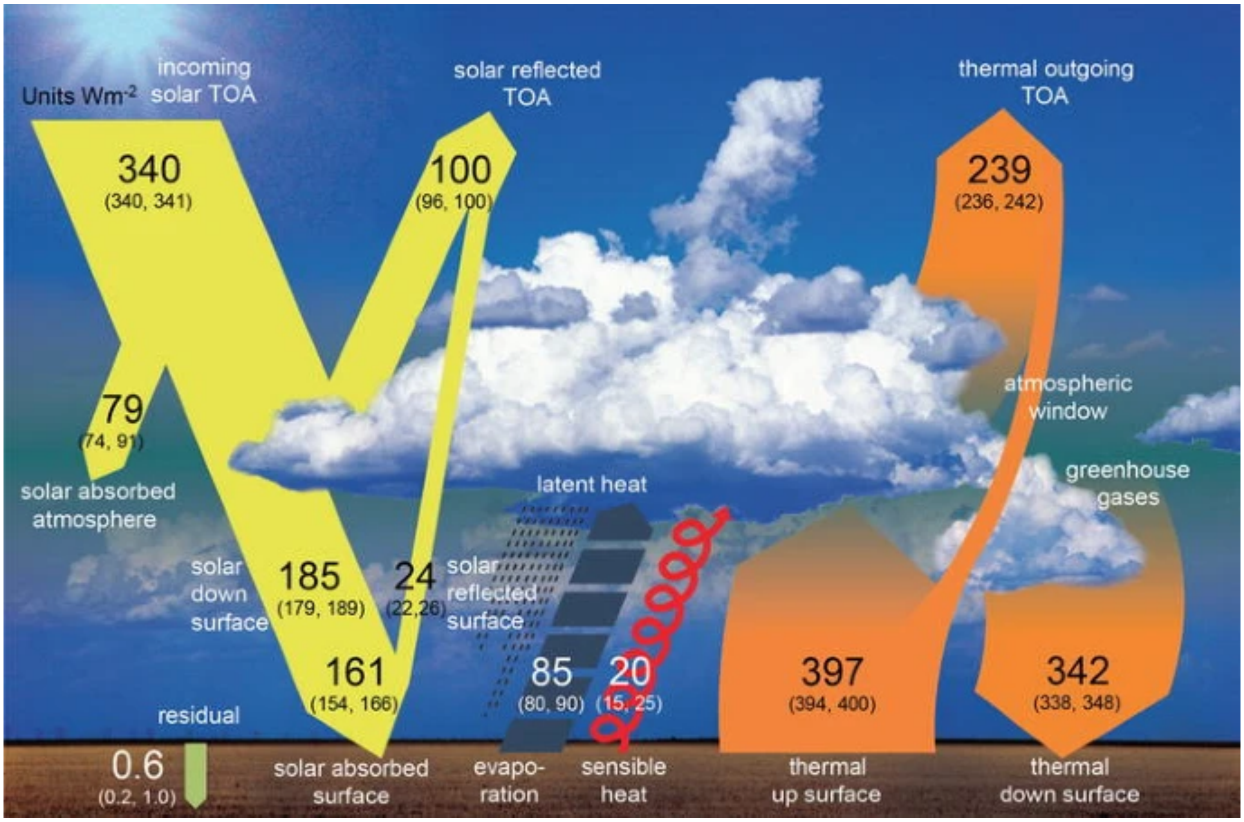

Figure 1.1: Figure 1 from Wild et al. (2013): "Schematic diagram of the global mean energy balance of the Earth. Numbers indicate best estimates for the magnitudes of the globally averaged energy balance components together with their uncertainty ranges, representing present day climate conditions at the beginning of the twenty first century. Units Wm^{-2}"

These attributes vary with cloud types due to their properties, as shown in Figure 1.2 (Chen et al., 2000; Matus and L'Ecuyer, 2017; Harrop and Hartmann, 2016; Fermepin and Bony, 2014). For example, high-altitude thin ice clouds have a net warming effects, acting as a thermal blanket by trapping outgoing longwave radiation from the Earth's surface (Hong et al., 2016), contributing to increases in surface and atmospheric temperature. Low-level thick clouds or water clouds such as maritime stratocumulus clouds play a dual role, trapping heat close to the Earth's surface during nighttime while providing a cooling effect during daytime due to reflection of incoming solar radiation (Stephens 2005; Klein et al., 2018). Variations of cloud properties have been accelerated through changes in atmospheric composition by human influences, which are large enough to exceed the bounds of natural variability (Karl and Trenberth, 2003). As a result, clouds have been recognized as crucial components in climate studies, making it necessary to improve our understanding of their characteristics, impacts, and changes.

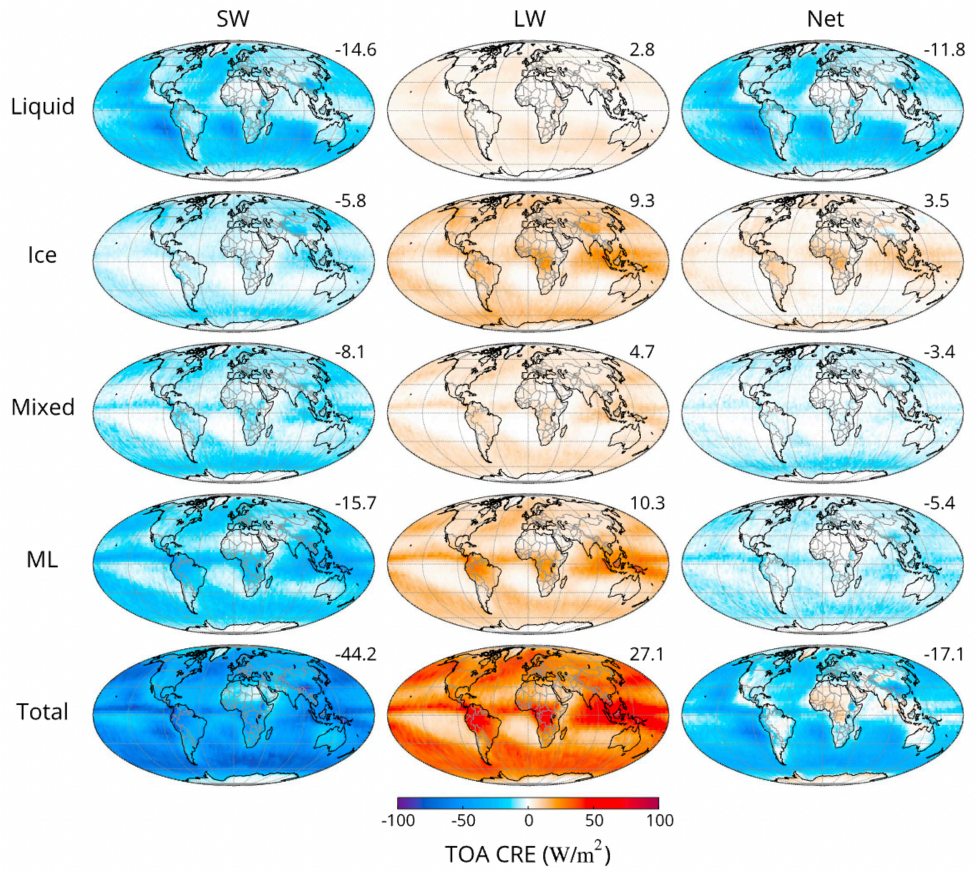

Figure 1.2: Figure 5 from Matus and L'Ecuyer (2017): "Annual average shortwave, longwave, and net cloud radiative effects at the top of atmosphere. Radiative effects are separated by water phase (liquid, ice, mixed, and multilayered) using R05 FLXHR-LIDAR, 2007 – 2010."

Many climate studies have investigated characteristics of clouds and changes in their properties connecting to the atmospheric variables using climate models. For example, the rise of convective cloud tops and decreases of tropical anvil cloud area over the ocean shown in a warmed climate condition (Bony et al., 2016). The shallow and low maritime clouds such as stratocumulus and trade cumulus increase in subtropical oceans (Bony and Dufresne, 2005; Brient et al., 2016). This change is controlled by atmospheric stability showing a strong relationship between inversion strength at the top of the planetary boundary layer and cloudiness (Wood and Bretherton, 2006) and it is strengthened with global warming. Therefore, these results are important to solve scientific questions about changes in clouds and their roles under global warming scenarios.

Simulating clouds and their radiative effects have been a long-standing challenge for climate modeling because of their inherent variability and the difficulties in fully understanding cloud formation and microphysical mechanisms (Hill et al., 2023). The uncertainty from clouds may arise because climate models employ a wide variety of parametrizations of the physical processes (Myers and Norris, 2016). Wright et al. (2020) examine differences among reanalysis high cloud products in tropics and found that all reanalysis datasets exhibit substantial biases in at least one radiative effect metric. Moreover, at the marine low cloud feedback, climate model results show important differences in regional pattern and magnitude compared satellite-based observations, as shown in Figure 1.3 (Myers et al. 2021), and it suggests importance of observation constraints to reduce uncertainty of climate sensitivity. Consequently, long-term cloud observations are necessary as complementary resources to assess the performance of climate models and validate our finding about clouds (Cesana and Chepfer, 2012; Suzuki et al., 2013; Li et al., 2018; Bender et al., 2019).

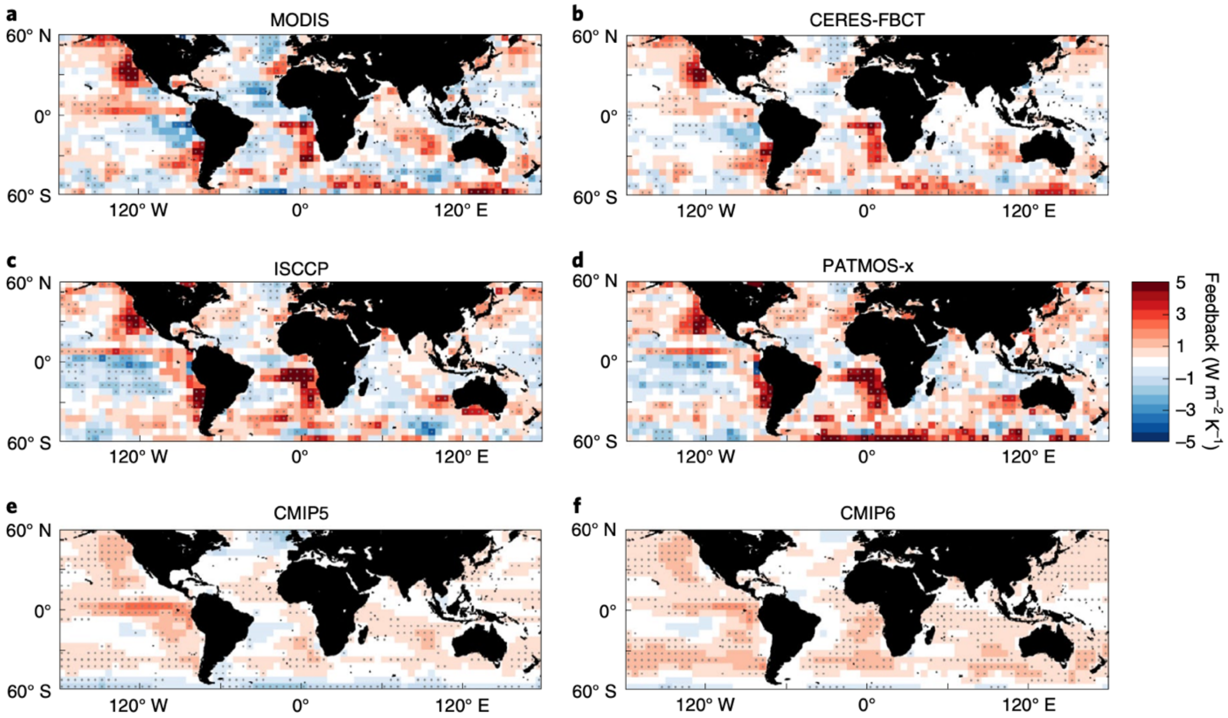

Figure 1.3: Figure 2 from Myers et al. (2021): “Marine low cloud feedback constrained by observations and simulated by global climate models. a-d, Marine low cloud feedback constrained by MODIS (a), CERES-FBCT (b), ISCCP (c) and PATMOS-x (d) satellite cloud observations. Stippling indicates statistical significance at the 90% confidence level based on observational uncertainty. e, f, Model-predicted marine low cloud feedback averaged over 7 CMIP5 models (e) and 11 CMIP6 models (f). Stippling indicates where 6 out of 7 and 10 out of 11 models of the respective ensembles agree on the sign of the feedback.”

Observing clouds has been conducted using diverse methods and measurements. Warren et al. (1998) investigated global distributions and changes in cloud cover and cloud phase over the ocean using observations from ships. Also, ground-based observations such as radar, lidar, ceilometer, and camera have been actively used in many cloud studies (Souza-Echer et al., 2006; Illingworth et al., 2007; Kazantzidis et al., 2012). These observations have the advantage of accuracy and reliability but are limited in spatial coverage and continuity of observations. In particular, these observations do not fully cover the ocean where clouds are crucial components in atmospheric and oceanic energy exchanges. Satellite-based remote sensing techniques facilitate global climate research the advantages of global coverage and stability through calibration and validation with other observations including in-situ, airborne, and ground-based remote sensing. Consequently, the National Oceanic and Atmospheric Administration (NOAA) initiated the Pathfinder Atmospheres-Extended (PATMOS-x) project to develop satellite-based climate data records (CDRs) of atmospheric cloud properties in collaboration with the Cooperative Institute for Meteorological Satellite Studies (CIMSS) at the University of Wisconsin-Madison (Stowe et al., 2002; Jacobowitz et al., 2003; Heidinger et al., 2014; Foster et al., 2023).

Since the 1980s, global observations of CREs have become possible with satellite measurements (Barkstrom, 1984; Loeb et al., 2018), and many studies have investigated their characteristics and variations based on cloud properties and regions using satellite-based observations (Cherian and Quaas, 2020; Ham et al., 2017; Hartmann and Berry, 2017). One of the long-term satellite-based CDRs for CREs is the Clouds and the Earth's Radiant Energy System Energy Balanced and Filled (CERES EBAF) Top-of-Atmosphere (TOA) Edition 4.0 dataset (Loeb et al., 2018), which has been used widely in CREs studies. Goessling et al. (2025) shows that recent global warming has been associated with an unusually large total TOA Earth's Energy Imbalance (EEI) due to a decrease in shortwave reflection by clouds, as shown in Figure 1.4. Recent studies suggest that this reduction in planetary albedo is driven by a decline in global cloud fractions (Tselioudis et al. (2024), Weaver et al. (2024), Loeb et al., (2024)). Notably, Figure 1.4 shows that the observations diverge from the full counterfactuals based on a two-layer model, in which ASR anomalies are assumed to be zero from the beginning of December 2020 onward, which is especially associated with low-level clouds. However, there are specific regions where albedo has increased, helping to reflect more solar radiation and mitigate surface warming. One notable example is the southeastern

Pacific Ocean, which serves as a representative region where enhanced cloud cover has contributed to higher albedo (Karlsson et al., 2023).

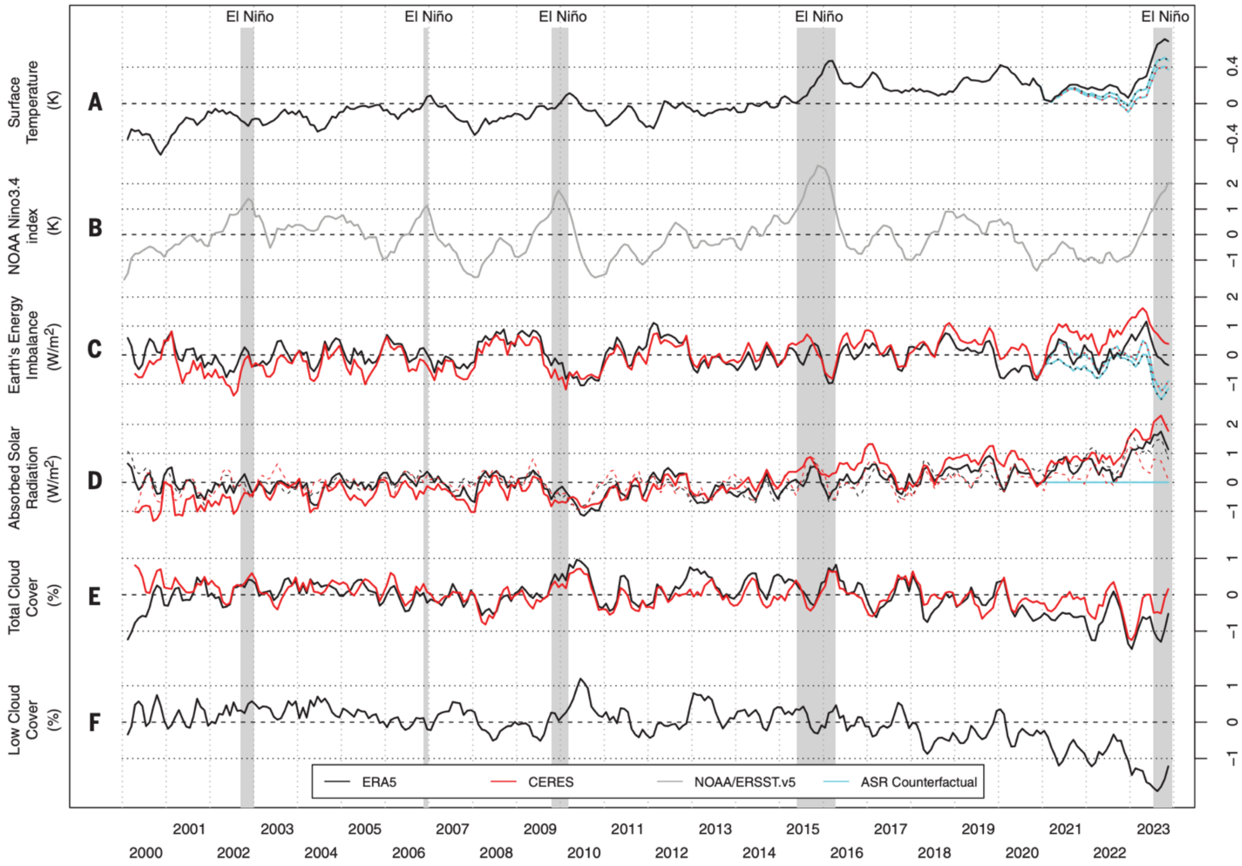

Figure 1.4: Figure 2 from Goessling et al. (2025): "Global mean anomalies of key parameters related to Earth's temperature, energy budget, and clouds. Three-month running-mean anomalies relative to 2001-2022 of (A) surface (skin) temperature, (B) National Oceanic and Atmospheric Administration (NOAA) Ocean Niño 3.4 index, (C) Earth's TOA total energy imbalance, (D) TOA net solar radiation, (E) total cloud cover fraction, and (F) low-cloud cover fraction. Red curves show satellite data from CERES, and black curves show reanalysis data from ERA5. Dashed curves in (D) show the TOA solar cloud radiative effect (or ASR) inferred from TCC anomalies. Cyan curves show the full counterfactuals based on a two-layer in which ASR anomalies are assumed to be zero from the beginning of December 2020 onward. El Niño periods with anomalies exceeding +1 K are highlighted with gray shading."

The southeastern Pacific Ocean, off the South America, is characterized by a prevalence of maritime low clouds. Maritime low clouds are essential for regulating climate and energy balance, primarily through their high albedo, which enhances solar radiation reflection into space (Boucher et al., 2013; Hartmann et al., 1992). These cloud formations are commonly found over the ocean near the western coasts of continents, where atmospheric subsidence driven by subtropical high-pressure systems interacts with cold sea surface temperatures (SSTs). This interaction helps sustain a shallow marine boundary layer (MBL), which is constrained by a temperature inversion (Norris and Klein, 2000; Wood and Bretherton, 2006). These meteorological conditions are collectively referred to as cloud-controlling factors (CCFs).

Andersen et al. (2022) show a decrease in maritime low clouds due to the increase in SSTs over the northeast Pacific, which leads to a weakening of the cooling effects of the clouds. These changes are the opposite of those observed in maritime low clouds over the southeastern Pacific Ocean using the third edition of CM SAF cLoud Albedo, and surface Radiation dataset (CLARA-A3; Karlsson et al., 2023), as shown in Figure 1.5. As a result, a better understanding of physical processes over this region is useful for improving the accuracy of climate model predictions associated with the global warming crisis that we are experiencing now.

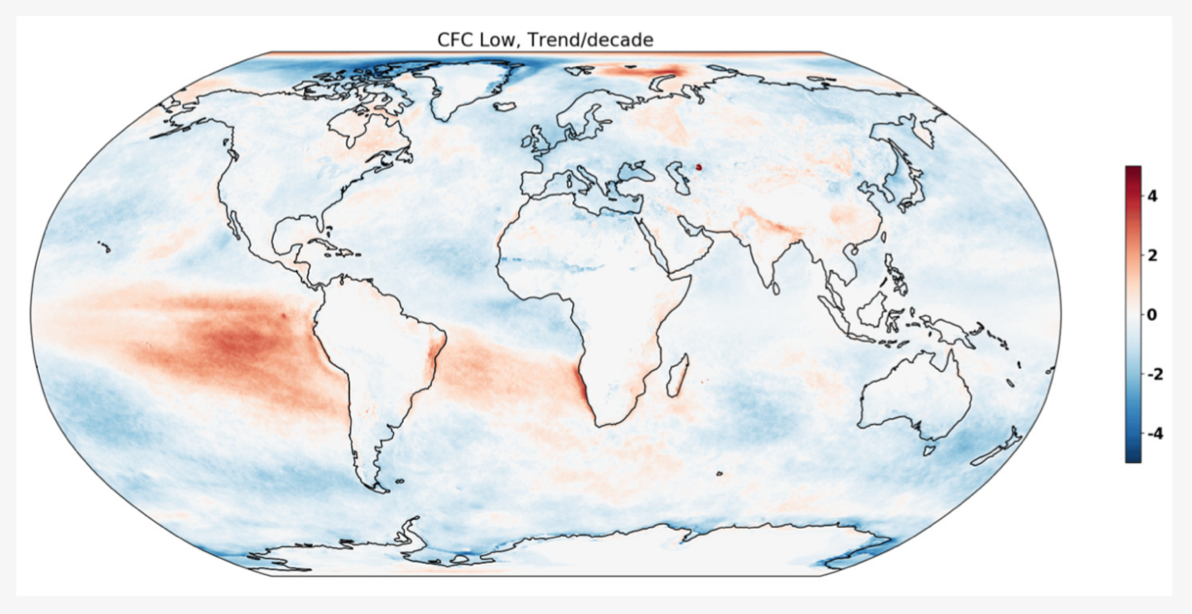

Figure 1.5: Figure 9 from Karlsson et al. (2023): "Geographical distribution of overall trends in the observable CLARA-A3 CFC contributions of low-level clouds (% per decade) from 1979 to 2020."

My dissertation investigates long-term changes in clouds over the ocean using Pv6.0 data over four decades since 1981. It examines their influences on radiative effects through the CERES EBAF dataset and explores the physical processes contributing to these changes, analyzed using CCFs from reanalysis data.

The overarching questions of my Ph. D. work are:

1) Have clouds changed significantly over the tropical and subtropical ocean since 1981?

2) How have observed changes in clouds influenced cloud radiative effects?

3) Can we identify physical processes contributing to regional changes in clouds?

These research questions are further motivated and expanded upon in the subsequent chapters.

Chapter 2

Have clouds changed significantly over the tropical and subtropical ocean since 1981?

2.1 Preface

The purpose of this chapter is to introduce the methodology to make monthly mean cloud properties from the Pv6.0 level 2b dataset, which generates two global observations per day per satellite, to investigate long-term changes in cloud amounts and properties over the ocean from 60°S to 60°N since 1981. To validate means and trends of cloud fractions from Pv6.0 and investigate similarities and differences with other long-term datasets, two satellite-based CDRs, CLARA-A3, and CERES EBAF, and two reanalysis datasets, the European Centre for Medium-Range Weather Forecasts (ECMWF) Reanalysis v5 (ERA5; Hersbach et al., 2020) and Modern-Era Retrospective analysis for Research and Application Version 2 (MERRA-2) from National Aeronautics and Space Administration (NASA), are used. This work was published in Seo et al. (2025b).

2.2 Data and Methodology

2.2.1 PATMOS-x v6.0

NOAA's Polar Operational Environmental Satellites (POES) program began with the NASA's launch of TIROS-1 in 1960, which is the world's first weather satellite, and demonstrated the potential of satellite-based weather observation and leaded to the development of operational polar-orbiting systems. After that, NOAA-1 was launched in 1970 as the first operational weather satellite which has visible and infrared imaging systems for cloud observation as well as atmospheric temperature and moisture profile retrievals. Starting in 1980, NOAA transitioned to more a sophisticated platform, the NOAA POES system satellite, which spanned 14 satellites, from

NOAA-06 to NOAA-19, and onboarded the Advanced Very High Resolution Radiometer (AVHRR) and High-Resolution Infrared Radiation Sounder (HIRS).

With the beginning of the POES system, long-term operational data collection of global satellite observations is conducted within the scope of the NOAA and NASA Pathfinder Program. The PATMOS project is a National Environmental Satellite, Data, and Information Service (NESDIS) component of the NOAA and NASA Pathfinder Program and had produced an extensive achieve of daily cloud cover, cloud properties, and surface variables for the period July 1981 to August 1994 (Stowe et al., 1997, 1999, and 2002; Wetzel and Stowe, 1999).

As a part of larger Data Stewardship Initiative within the NESDIS Office of Research and Applications (ORA), the PATMOS-x project was initiated to improve the AVHRR data and make it more useful for climate studies in collaboration with NOAA and CIMSS at the University of Wisconsin-Madison (Heidinger et al., 2005). The PATMOS-x project offers more products at a higher spatial resolution with well-calibrated radiometric observations compared to the original PATMOS dataset, in addition to improved cloud masking using the Clouds from AVHRR Extended (CLAVR-x) processing system. The PATMOS-x project focuses on producing a reliable satellite-based climate dataset of calibrated radiometric observations and atmospheric variables as well as surface products (Heidinger et al., 2014).

The major components in the PATMOS-x dataset are cloud properties, including cloud mask and phase, cloud top assignments and optical properties. This dataset has been developed through many efforts in calibration and validation including radiometric consistency (Heidinger et al., 2002; Heidinger et al., 2003; Molling et al., 2010), inter-satellite validation (Heidinger et al., 2010; Heidinger et al., 2016), sensitivity to ancillary data (Foster et al., 2016), and correction to orbital drift of satellites (Foster and Heidinger, 2013). As a result, this dataset has been widely used in many atmospheric research studies such as the investigation of global water and ice cloud distributions with climate models (Eliasson et al., 2011), microphysical cloud properties in marine boundary layer (Rausch et al., 2010), and the global changes in aerosol (Cermak et al., 2010; Zhao et al., 2013) as well as climate studies for regional and global applications (Foster et al., 2019; Ackerman et al., 2013; Nielsen et al., 2011; Stubenrauch et al., 2013; Sun et al., 2015; Wu et al., 2014; Zhong et al., 2016; Norris et al., 2016).

The latest version of PATMOS-x adopts a fusion methodology by using a combination of AVHRR and HIRS to overcome the limitations of the prior PATMOS-x version 5.3 (Foster et al., 2023). PATMOS-x version 5.3 provides information from five spectral channels from a single AVHRR that may vary dependent on the version of sensor. The Pv6.0 dataset with this new technique shows improvement in inter-satellite consistency, as shown in Figure 2.1, cloud detection, accuracy of cloud properties and more similarity with more modern sensors such as Visible Infrared Imaging Radiometer Suite (VIIRS). Consistency with VIIRS sensor is remarkable in satellite-based climate research in the future because VIIRS is the next generation of sensor for the NOAA POES project including Soumi National Polar-orbiting Partnership (Soumi NPP), NOAA-20, and NOAA-21. Intercomparison and investigation of consistency between AVHRR-based satellite (NOAA-18, NOAA-19, MetOp-A, and MetOp-B) and VIIRS-based satellite (NOAA-20) were conducted by Seo et al. (2025).

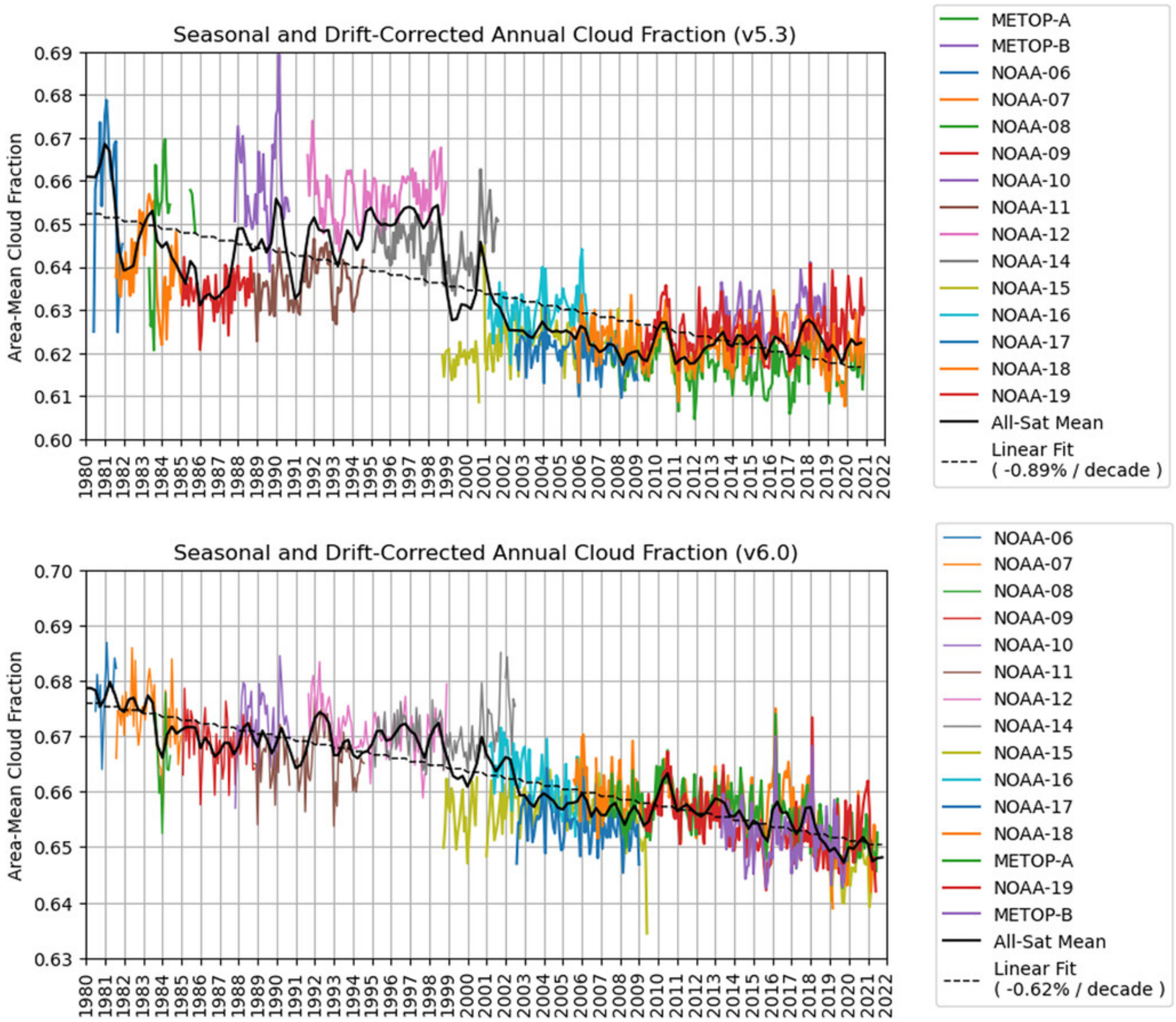

Figure 2.1: Figure 6 from Foster et al. (2023): "Seasonal drift-corrected global cloud fraction time series for (top) Pv5.3 and (bottom) Pv6.0. Individual satellites are color-coded. The thick black line is the all-satellite mean and the dashed black line represents the linear fit."

In this study, Pv6.0 level2b dataset is used to make monthly mean cloud properties to analyze the mean and trend in cloud properties. This dataset provides daily observations with a spatial resolution of 0.1° ×0.1° starting from 1981.

2.2.1.1 Enterprise Cloud Mask (ECM) algorithm

Total, water, and ice cloud fractions are derived using cloud masking and phasing products from the NOAA/NESDIS Enterprise Cloud Mask (ECM) algorithm (Heidinger et al., 2012; Heidinger et al., 2020). This algorithm is based on a Naïve Bayesian method, trained using cloud layer and cloud phase products from NASA's Cloud-Aerosol Lidar and Infrared Pathfinder Satellite Observation (CALIPSO)/Cloud-Aerosol Lidar with Orthogonal Polarization (CALIOP). The updated ECM algorithm, integrated into Pv6.0, represents an evolution from Pv5.3 by introducing two- and three-dimensional classifiers comprised of radiometric observations (0.65, 0.86, 3.75, 7.3, 11.0, and 13.3 μm), ancillary data (temperature profile) and radiative transfer calculations to produce clear, water, and ice cloud probabilities. A 4-level cloud mask is determined by cloud probability, categorized as confidently clear, probably clear, probably cloudy, and confidently cloudy.

One of the products from ECM is the cloud type classification, which consists of 10 categories: clear, probably clear, fog, water, mixed, supercooled water, opaque ice, cirrus, overlapping, overshooting. Cloud type is classified using the 4-level cloud mask, water, and ice probabilities, cloud mask uncertainty, radiometric observations such as reflectivity and brightness temperature, cloud top temperature, and other ancillary information. Therefore, cloud type is highly related to the characteristics of clouds and their radiative effects. The cloud phase/type identification is also important to a-prior values for other cloud property retrievals. In this study, the cloud type is used to determine cloud phase, which consists of 4 categories: clear, total, water, and ice. For example, clear and probably clear are categorized as clear and all other cloud types are cloudy. Fog, water, mixed, and supercooled water are grouped as the water cloud phase, while opaque ice, cirrus, overlapping, and overshooting are classified as ice cloud phase. Total clouds are combination of water and ice. Total (water and ice) cloud fractions are calculated from the ratio of all (water and ice) cloudy counts to all counts within $1° \times 1°$ grid box for a specific hour and month. After that, monthly mean total (water and ice) cloud fractions are computed with diurnal correction using the backfitting model and observational weighting.

2.2.1.2 GOES-R Algorithm Working Group (AWG) Cloud Height Algorithm (ACHA)

For the cloud top assignments including cloud top height and temperature, the GOES-R Algorithm Working Group (AWG) cloud height algorithm (ACHA) is used. This algorithm is based on a one-dimensional (1D) VAR optimal estimation method (Heidinger and Pavolonis, 2009). Correct cloud phase determination is critical to the accuracy of cloud top assignment, because it is required to determine which *a priori* information is used for the forward model. The ACHA applied in Pv6.0 uses the 11.0 and 13.3 μm channels to estimate cloud top temperature, cloud emissivity, and a cloud microphysical index. Subsequently, cloud top height and pressure are derived from the estimated cloud top temperature and numerical weather prediction profiles at the pixel level. NASA's MODIS and CALIPSO/CALIOP products were used to validate the ACHA products (Young and Vaughan, 2009). In this study, cloud top temperature and height are analyzed using map plots, and monthly mean plots as well as zonal mean plots.

2.2.1.3 Daytime Cloud Optical and Microphysical Properties (DCOMP) algorithm

The retrieval of cloud optical properties is carried out using the Daytime Cloud Optical and Microphysical Properties (DCOMP) algorithm (Walter and Heidinger, 2012). This method uses a standard bispectral approach to estimates optical depth and effective radius, relying on radiometric observations from one visible and one near-infrared channel. Because POES satellites have different channel capabilities for daytime observations, most of NOAA satellites use the AVHRR 3.75-µm DCOMP mode, which combines the 0.65 and 3.75 µm, while NOAA-16, NOAA-17, and MetOp satellites use the AVHRR 1.6 µm instead of the 3.75 µm. This distinction in DCOMP modes leads to significant differences, particularly in cloud effective radius estimates (Foster et al., 2023). For this study, cloud optical depth (COD) is examined solely to characterize cloud thickness.

2.2.1.4 Orbital drifts and diurnal correction

In this study, each satellite's monthly mean values are computed from twice-daily gridded observations (Pv6.0 level 2b). Figure 2.2 shows the equatorial local overpass times of ascending and descending nodes for all satellites used in Pv6.0. After launch, the orbit of most satellite drifts, which changes the local overpass time (Ignatov et al., 2004). This orbital drift must be considered when calculating daily and monthly mean values (Foster and Heidinger, 2013). Also note that there are no late-morning observations before 2002 (Weaver et al., 2024). As a result, considering orbital drifts and different local overpass times between satellites is necessary to make stable long-term records from polar orbiting satellite observations (Bojanowski and Musial, 2020).

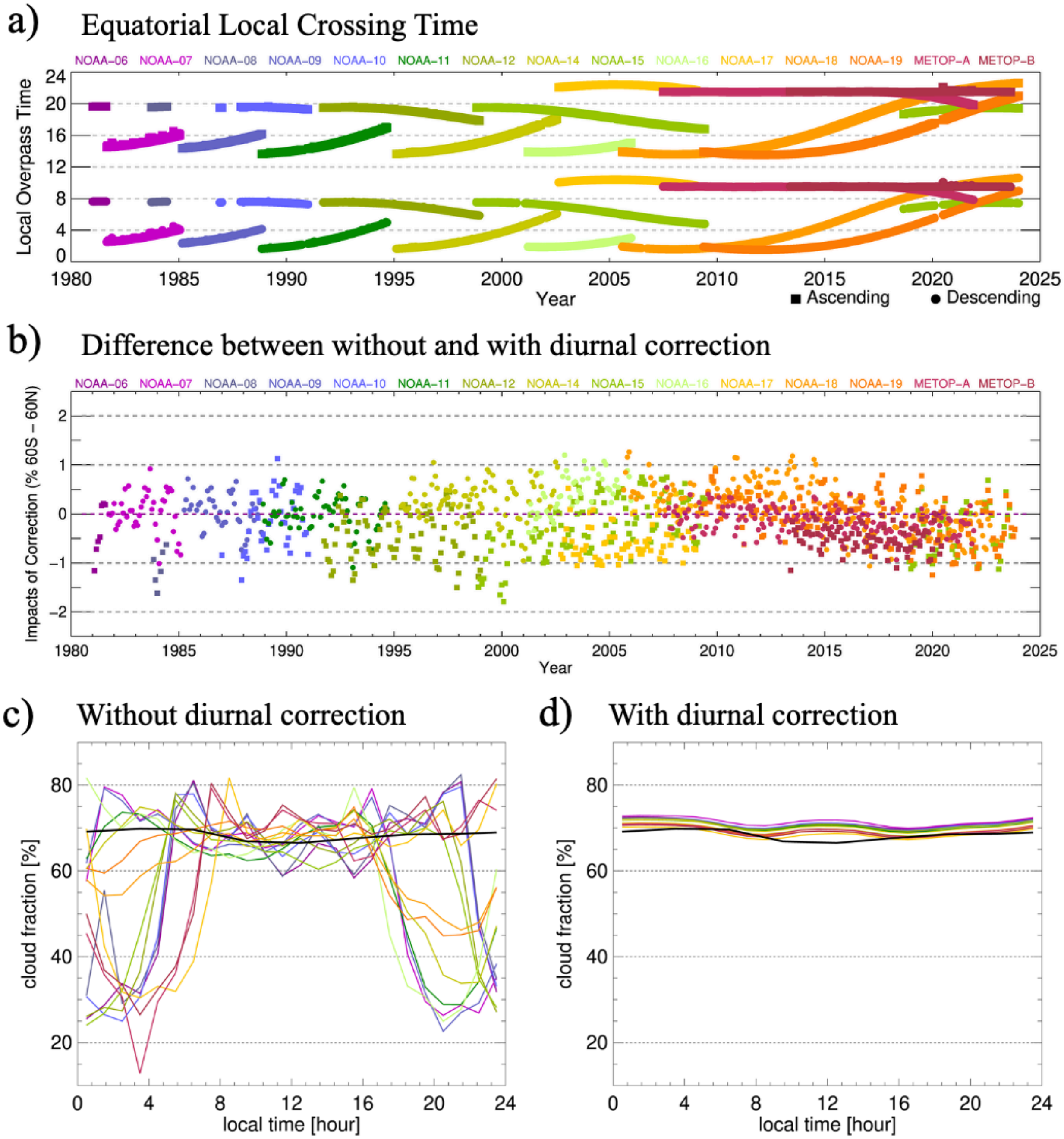

Figure 2.2: a) Equatorial local overpass time of the NOAA and MetOp POES series from the Pv6.0 level 2b dataset spanning from 1981 to 2023. b) difference between anomaly of mean total cloud fraction without/with diurnal correction. c) hourly global mean cloud fraction without diurnal correction (black line is a GEO-Ring composite). d) hourly global mean cloud fraction with diurnal correction.

To correct for orbital drifts and different overpass times, we first diagnose the diurnal cycle for each 1° ×1° grid box and month of the year. The basic idea about diurnal correction is that almost all hours of the day are observed at some point in the record at shown in Figure 1a. A generalized additive model (GAM) is used to isolate the diurnal cycle, even in the presence of interannual variability and long-term trends. Using the diurnal parameters from the GAM and actual observations, monthly daily mean values are calculated as follows:

$$\overline{y_{daily}} = \sum_{i}^{24} y_{model}(i) \times \left\{ 1 + \frac{1}{\sum_j \left| Coef_{i,j} \right|} \sum_{j} \left(\frac{y_{obs}(j) - y_{model}(j)}{y_{model}(j)} \right) Coef_{i,j} \times \left| Coef_{i,j} \right| \right\}$$

where j and y_{obs} are the local time index (0-23 hours) and averaged cloud property values observed from satellite on a given hour. y_{model} is the modeled diurnal cycle from the GAM. $Coef_{i,j}$ is the autocorrelation coefficient of the cloud product between model hour (*i*) and observation hour (*j*) at a specific month and location. The autocorrelation coefficient is derived empirically from all observations since 1981. This method can be viewed as a kernel smoother that combines the climatological diurnal cycle and observations to impute a full day of observations before averaging and the idea about observational weighing using model output and actual observation is suggested in Foster et al. (2013). This method is separately applied to cloud fractions and cloud top properties depending on the cloud phases (total, water, and ice).

Figure 2.2b shows differences in total cloud fraction over the ocean from 60°S to 60°N without and with diurnal correction using the GAM and observational weighting from 1981 to 2023.

Morning-orbit (afternoon-orbit) satellites tend to have lower (higher) cloud fractions without diurnal corrections, and the GAM and observations weighting reduce these differences. Notably, for NOAA-19, the differences align with changes in equatorial local overpass time (Figure 1a). Figure 2.2c and 2.2d show the global hourly mean cloud fraction from Pv6.0 without diurnal correction and with diurnal correction. We created a GEO-Ring composite to compare the diurnal cycle of global mean cloud fraction (black line in Figure 2.2c and 2.2d). Without diurnal correction, the variations between inter-satellites are large due to the different coverage of local overpass time depending on orbits and orbital drifting. With diurnal correction, all polar orbiting satellites from Pv6.0 show a similar diurnal cycle to the GEO-Ring composite except between the hours from 10 to 14. These figures show that the GAM and observational weighting effectively reduce inter-satellite variability caused by different local overpass times and orbital drifts.

2.2.2 CERES EBAF

The primary goals of the CERES EBAF TOA products are to produce integrated global CDRs for detecting decadal changes in the radiation budget from the surface to TOA observed by CERES instruments onboard Terra, Aqua, Suomi NPP and NOAA-20 satellites in addition to the cloud and aerosol properties since 2000 (Loeb et al., 2018). This dataset has been used in many climate studies to investigate changes in cloud radiative effects and feedback (Ceppi et al., 2021; Yuan et al., 2023; Ghausi et al., 2023; Goessling et al., 2025) and climate sensitivity (Sherwood et al., 2020; Loeb et al., 2021) as well as validate results with climate models (Dunne et al., 2020; Döscher et al., 2021; Boucher et al., 2020; Smith et al., 2020). In this study, CERES EBAF Edition 4.2 (Ed4.2) level 3b dataset is used, which is the monthly mean values with 1° ×1° spatial resolution.

2.2.3 CLARA-A3

The EUMETSAT Satellite Application Facility on Climate Monitoring (CM SAF) provides long-term cloud, albedo, and surface radiation datasets since 1979 through the CLARA-A3 (Karlsson et al., 2023). This dataset is also based on the AVHRR-based satellites. The CLARA-A3 dataset provides additional information compared to CLARA-2, including higher spatial resolution (0.25° ×0.25°), and shortwave and longwave radiation at surface and TOA, with improvements in retrieval algorithms. With these advancements, this dataset has been used in many climate studies as satellite-based CDRs (Tselioudis et al., 2024; Myers et al., 2024; Riihelä et al., 2024; Devasthale et al., 2023). In this dissertation, the monthly mean of the fractional cloud cover product from CLARA-A3 is used for comparison with the Pv6.0 dataset in chapter 2 and net radiation products are used in chapter 3.

2.2.4 ERA5 reanalysis dataset

ERA5 is the fifth generation of atmosphere reanalysis dataset produced by ECMWF (Hersbach et al., 2020). By optimally combing observations and models, this dataset provides a continuous and consistent record of atmospheric variables, ensuring integrity and coherence in representing key Earth system cycles. With a substantial increase in both the horizontal and vertical resolution, along with a decade of advancements in model development and data assimilation, ERA5 offers an expanded set of output parameters, hourly high-resolution output throughout, and 3-hourly uncertainty information. As a result, ERA5 have been used in a wide array of applications in atmospheric sciences including improving medium-range global weather forecasting (Lam et al., 2023; Bi et al., 2023) and studying global climate change (Jones et al., 2023; Seneviratne et al., 2021). In this study, we use monthly mean cloud fractions in chapter 2 and atmospheric variables in chapter 4 at a spatial resolution of 0.25° ×0.25°.

2.2.5 MERRA-2 reanalysis dataset

The MERRA-2 is the latest atmospheric reanalysis of the modern satellite era produced by NASA's Global Modeling and Assimilation Office (GMAO) (Gelaro et al., 2017). MERRA-2 assimilates observation types not available to its predecessor, MERRA, and includes updates to the Goddard Earth Observing System (GEOS) model and analysis scheme so as to provide a viable ongoing climate analysis beyond MERRA's terminus. While addressing known limitations of MERRA, MERRA-2 is also intended to be a development milestone for a future integrated Earth system analysis (IESA) currently under development at GMAO. Among the advances in MERRA-2 relevant to IESA are the assimilation of aerosol observations, several improvements to the representation of the stratosphere including ozone, and improved representations of cryosphere processes. Other improvements in the quality of MERRA-2 compared with MERRA include the reduction of some spurious trends and jumps related to changes in the observing system and reduced biases and imbalances in aspects of the water cycle. Consequently, MERRA-2 has been used in many atmospheric studies including investigating global precipitations (Maclennan et al., 2022; Yang et al, 2023; Andrade et al., 2024), analyzing ozone variations (Stauffer et al., 2019; Ziemke et al., 2019; Orbe et al., 2020), and studying aerosols interacting with clouds (Zhu et al., 2022; Bender et al., 2019). In this dissertation, we use monthly mean cloud fractions in chapter 2 at a spatial resolution of 0.5° ×0.625°.

2.3 Cloud Fraction

Cloud fraction is essential for calculating the net TOA flux of radiation simulated by a model. It can be expressed as the sum of two components (Taylor et al., 2007):

$$R = (1 - c)R_{clr} + cR_{oc}$$

where c is the fraction of the region covered by clouds, R_{clr} is the spatially averaged flux obtained by removing all clouds from the region and performing a radiative transfer calculation, and R_{oc} is the flux averaged over only the overcast portion of the region. Moreover, CREs can be determined using following equation:

$$CRE = R_{clr} - R = c(R_{clr} + R_{oc})$$

Differences in cloud fraction can contribute to variations in the net TOA flux of radiation and influence the uncertainty of radiative effects in climate model simulations. Therefore, obtaining accurate cloud fraction estimates and understanding their changes are crucial for climate studies.

2.3.1 Map of mean cloud fractions

Figure 2.3 provides a map of mean and trend for total, water, and ice cloud fractions over the last four decades from Pv6.0. The trend is calculated using a linear fit between time and deseasonalized anomaly values. In Figure 2.3a, cloud fractions are usually high (>80%) over the ocean including Inter Tropical Convergence Zone (ITCZ), marine stratocumulus clouds regimes, and midlatitudes. The large-scale subsidence areas near the 20° latitude show relatively low cloud fractions (<40%). The trends in total cloud fractions are shown in Figure 2.3b. Figure 2.3c shows statistical significance tests for trends. Areas surrounded by a red line are statistically significant, while areas that are not statistically significant are left blank. For the statistical significance test of trends, the method described in Weatherhead et al. (1998) is used, applying a 95% confidence level. This method is useful for detecting long-term linear trends of atmospheric variables, considering various factors such as the time span of data, the magnitude of variability, and the presence of autocorrelation in the data.

Decreasing trends in total cloud fractions are dominant from 60°S to 60°N, which is highly related to a zonal contraction and a strengthening of the ITCZ regions and expansion of the subtropical dry zone (Tselioudis et al., 2024). The Central Pacific Ocean especially shows the remarkable decreasing trend of approximately 3% to 4% per decade. The western Pacific Ocean and the west coast of South America show slightly increasing trends, even though most of these are not statistically significant. The magnitude of trend is smaller than the confidence level because of high cloud fractions over these regions, higher than 80%, and high seasonality and variability due to changes in global circulation patterns such as the El Niño-Southern Oscillation (ENSO).

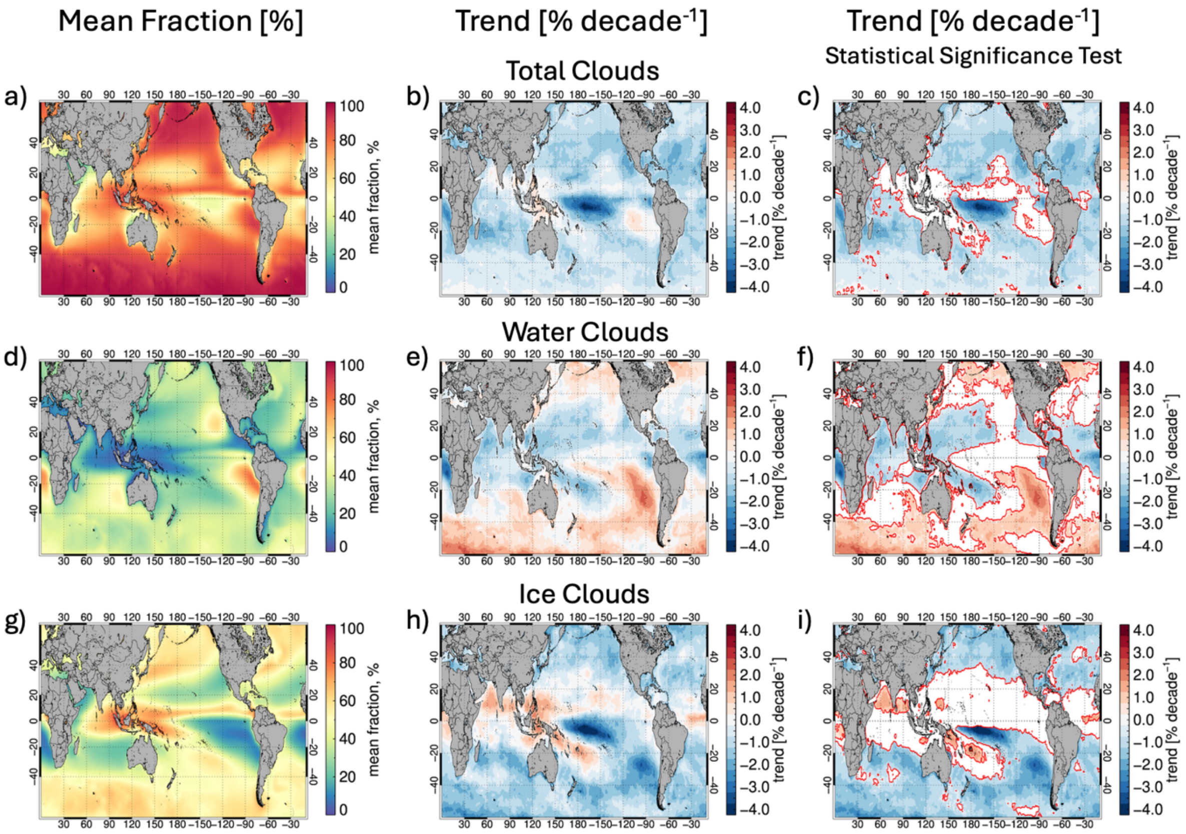

Figure 2.3: Map of mean cloud fractions (left column), trend of cloud fractions (middle column; % per decade), and statistical significance test (right column: areas thar are not statistically significant are blanked and are surrounded by a red line is statistically significant) from Pv6.0.

The maps of the mean and trend for water clouds are shown in Figure 2.2d and 2.2e in addition to the statistically significant tests in Figure 2.2f. The regions where maritime stratocumulus clouds are dominant, including the west coast of North America, South America, and Africa, show high fractions of water clouds (>60%). With these areas, increasing trends are dominant over the west coast of South America and the southern mid-latitude regions, with a maximum of 3.0% per decade. This is related to increases of shallow and maritime low clouds such as stratocumulus and trade cumulus, over subtropical ocean due to the increases of atmospheric stability associated with global warming (Bony and Dufresne, 2005; Brient et al, 2016). Water clouds are less frequent

(<20%) over western Pacific Ocean and the ITCZ due to the dominance of high and thick clouds caused by strong convection. Decreasing trends over the ITCZ and northern mid-latitudes are about 1.0% to 2.0% per decade. This might be caused by ITCZ intensification (Wodzicki and Rapp, 2016) and its migration and expansion to the Northern Hemisphere (Schneider et al., 2014).

Mean and trend of ice clouds as well as statistical significance test are shown in Figure 2.2g-i. Cloud area fractions of ice cloud are high over western Pacific Ocean, the ITCZ (>70%), and increasing trends are dominant even though some areas are not statistically significant due to the high seasonality and variability. Ice cloud fractions are also high over both the northern and southern midlatitude ocean (>60%), although a decreasing trends in ice clouds are observed over these areas. This is related to transitions from ice to water cloud particles as temperature warms which can result in both larger cloud amounts and larger cloud optical depths through the ’cloud phase feedback’ (Tan and Storelvmo, 2016; Frey and Kay, 2017). The significant decreases in cloud fraction over the central Pacific Ocean appear to be attributable to ice clouds, which make up most of the clouds in that region.

The changes in albedo, as shown in Weaver et al., (2024), are comparable to the observed changes in cloud fractions, highlighting significant regional patterns. For example, albedo increases have been observed along the west coast of South America and over southeastern Asia. In contrast, decreases in albedo are evident in regions such as the central Pacific Ocean and midlatitudes, which could be associated with reduced cloud fractions. Understanding these dynamics helps in assessing the impacts of cloud changes on global climate patterns and energy fluxes because clouds play a key role in regulating the Earth’s energy balance (Ramanathan et al., 1989; Harrison et al., 1990).

To investigate the similarity and difference of trends in cloud fractions with other long-term dataset, Figure 2.4 shows the trend of cloud fractions over the ocean from 1981 to 2023 and from 2000 to 2023. Three satellite-based CDRs, Pv6.0, CLARA-A3, and CERES EBAF, and two reanalysis datasets, ERA5 and MERRA-2, are compared. First, Pv6.0 and CLARA-A3 looks similar in the trend of total cloud fraction from 1981 to 2023, as introduced in previous research (Karlsson et al., 2023; Devasthale and Karlsson, 2023). These show substantial decreasing trends in the central Pacific Ocean, as well as in the subtropical and midlatitude ocean, while modest increasing trends are observed over western Pacific Ocean and the west coast of South America.

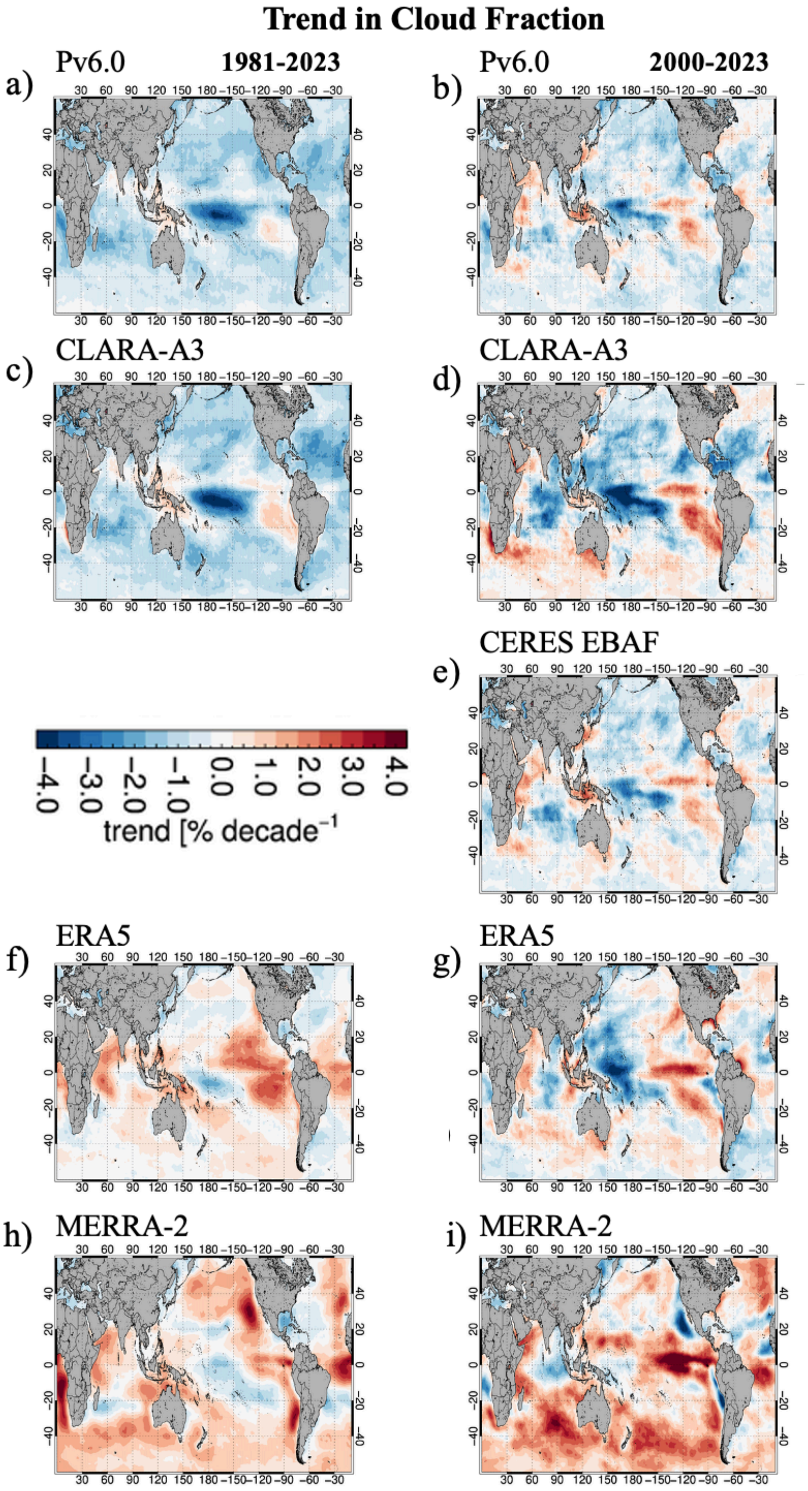

Figure 2.4: Map of trend of cloud fractions (% per decade) from 1981 to 2023 (left column) and from 2000 to 2023 (right column). a) and b) are from Pv6.0. c) and d) are from CLARA-A3. e) is from CERES EBAF. f) and g) are from ERA5. h) and i) are from MERRA-2.

Reanalysis datasets show different trends in total clouds compared to satellite-based CDRs from 1981 to 2023, and the results also differ among the reanalysis dataset themselves. For example, MERRA-2 and ERA-5 show dominance of increasing trends, including over the west coast of North America and Atlantic Ocean near the Equator. Especially, MERRA-2 shows significant increasing trends in the midlatitude ocean even though ERA-5 shows decreasing trend or weak increasing trend. The high variations between reanalysis datasets and models due to different parametrization and cloud feedback mechanism are investigated in previous research (Loveridge and Davies, 2019; Vignesh et al., 2020; Myers et al., 2021). However, decreasing trends in the central Pacific Ocean, western Pacific Ocean and the west coast of South America are observed for both reanalysis datasets even though the size of area and magnitude differ from observations.

Even though CLARA-A3 and Pv6.0 apply different algorithms for clouds, they use the same platforms and sensors to obtain cloud properties. The CERES EBAF dataset, based on the MODIS sensor, provides an independent dataset from a more modern sensor with no orbital drifts, while it is only available since 2000 (Figure 2.4e). The CERES EBAF shows comparable trends in total cloud fractions as Pv6.0 and CLARA-A3 from 2000 to 2023. The decreasing trends over the central Pacific Ocean as well as northern subtropical and midlatitude oceans and increasing trends on the west coast of South America are also dominant during this period for all three satellite-based CDRs. However, differences between satellite-based CDRs over the Southern Ocean are observed. Cloud fractions increase in CLARA-A3 and decrease in Pv6.0, with CERES falling between them. Differences between observations over the midlatitude Southern Ocean are also shown in Tselioudis et al. (2024) and this is also noticeable between climate models (Schuddeboom and McDonald, 2021). This would benefit from further investigation.

The trends in total cloud fractions from ERA5 from 2000 to 2023 show similar patterns to those from satellite-based CDRs, including decreasing trends over the west central Pacific Ocean and increasing trends on the west coast of South America and the east central Pacific Ocean. However, ERA5 shows opposite trends over the west coast of North America compared to the observations. In MERRA-2, increases of cloud fraction are dominant between 2000 to 2023, and it is especially noticeable over the midlatitude Southern Ocean. Overall, satellite-based CDRs exhibit similar patterns in trends but differ from reanalysis dataset. However, ERA5 show similar trends to satellite-based observations from 2000 to 2023. The high similarities between satellite-based CDRs have also been shown in other previous studies in terms of timeseries and zonal mean plot (Foster et al., 2023; Karlsson et al., 2023). The largest variations between datasets are observed in the midlatitude Southern Ocean. These differences may reflect challenges in accurately capturing cloud properties in this region, where dynamic weather patterns and low solar angles complicate observations and data assimilation, as well as different parameterizations of clouds and cloud feedback mechanisms in weather prediction models and climate modeling.

2.3.2 Timeseries of mean cloud fractions

Figure 2.5 shows timeseries of mean total, water, and ice cloud fractions from 60°S to 60°N over the ocean from 1981 to 2023. The fractions of total clouds range from 72.0% to 79.3% (75.3 ± 1.5%) and show strong seasonality, being highest in December and lowest in March. It has a decreasing trend of 0.91% per decade over the last four decades, even though the mean cloud fractions appear flat after the early 2000s. The cloud fractions of the water phase range from 28.4% to 34.2% (31.2 ± 1.2%). It is highest in July and August, and lowest in February and March. The trend in water cloud fraction is small compared to total and ice cloud fractions, with an increase of 0.03% per decade. The ice cloud fractions vary from 40.5% to 49.4% (44.1 ± 1.7%). Ice cloud fractions are high in December and January, and low in August. It shows a significant decreasing trend of 0.91% per decade. Therefore, the decreasing trend in cloud fraction is mainly driven by decreases in ice clouds. To investigate seasonal and latitudinal changes in cloud fractions, we will analyze monthly and zonal mean plots.

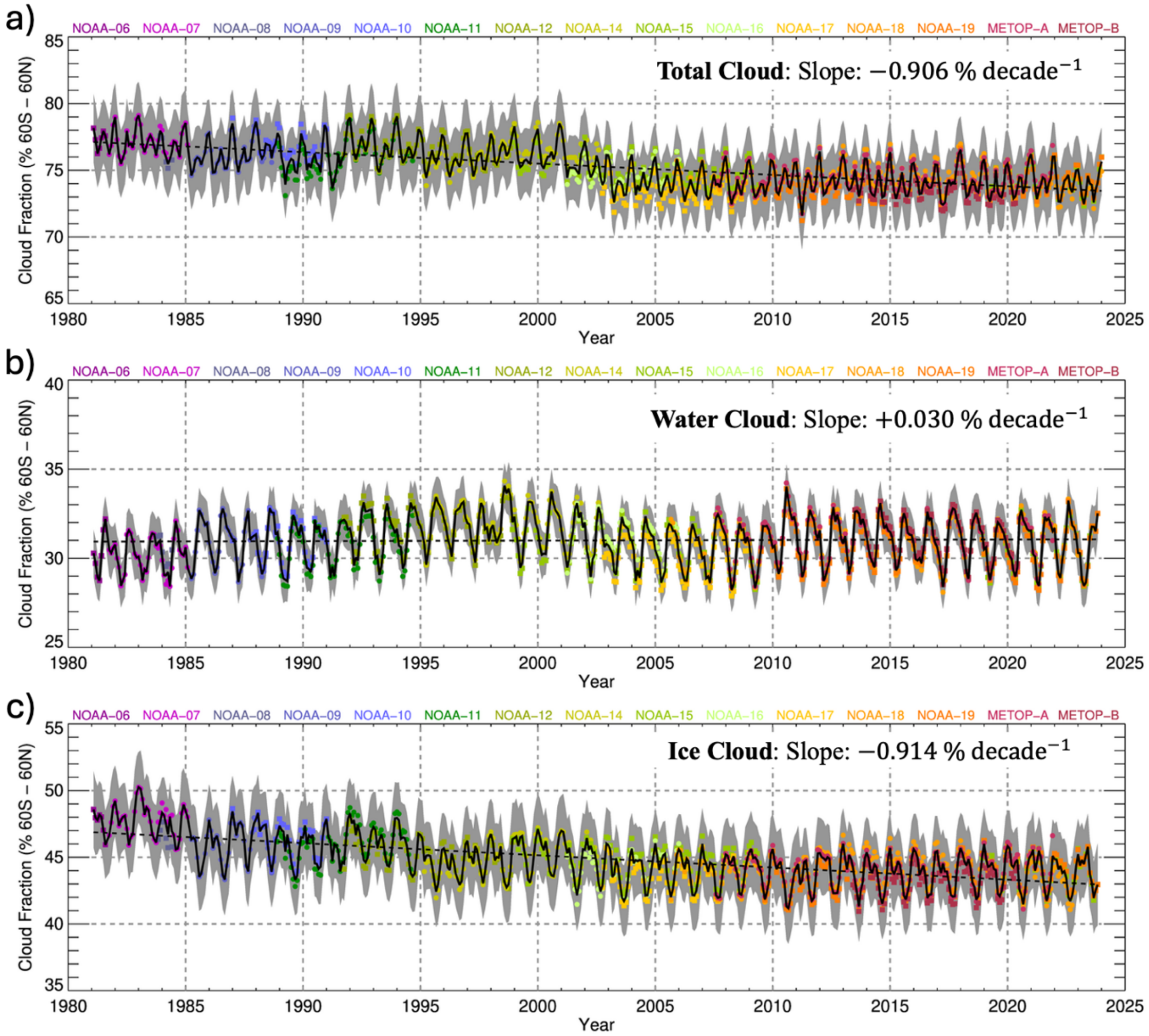

Figure 2.5: Timeseries of mean cloud fractions over the ocean from 60°S to 60°N from Pv6.0. a is total clouds. b is water clouds. c is ice clouds. Colors represent POES satellites.

Figure 2.6 presents the timeseries of mean cloud fractions over the ocean from 60°S to 60°N since 1981. As shown in Figure 2.4, ERA5 and MERRA-2 exhibit lower mean cloud fractions compared to satellite-based CDRs. The differences between satellite-based CDRs and reanalysis datasets are about 5% to 15%. The trends in Pv6.0 and CLARA-A3 are both negative, at −0.85% per decade and −0.91% per decade from 1981 to 2023, respectively. However, ERA5 and MERRA-2 show increases in cloud fraction, at 0.31% per decade and 0.70% per decade. Since 2000, the satellites-based CDRs have continued to show decreasing trends in cloud fraction although the magnitudes are reduced. CERES and ERA5 also exhibit decreases in cloud fraction at −0.21% per decade and −0.12% per decade, respectively. MERRA-2 still shows an increase in cloud fraction of +0.85% per decade. Therefore, the decreasing trends in cloud fraction over the ocean are noticeable although the magnitudes differ slightly between satellite-based datasets.

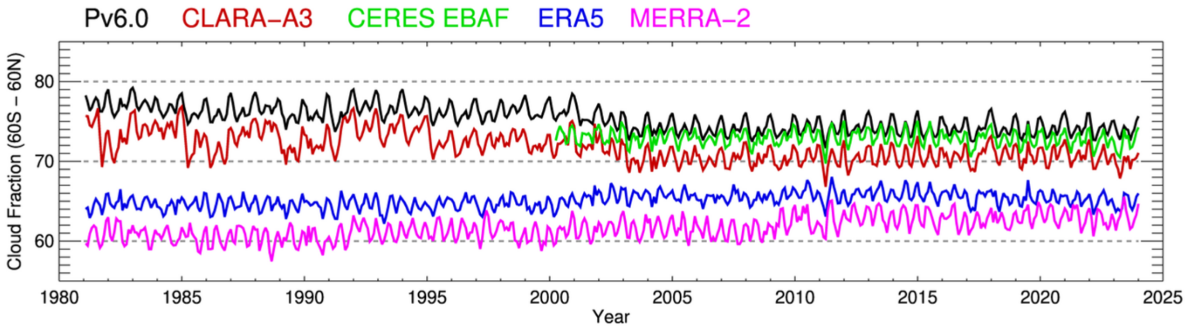

	1981 - 2023				2000 - 2023				
	Pv6.0	CLARA-A3	ERA5	MERRA-2	Pv6.0	CLARA-A3	CERES	ERA5	MERRA-2
Trend [% decade^{-1}]	−0.85	−0.91	+0.31	+0.70	−0.44	−0.31	−0.21	−0.12	+0.85

Figure 2.6: Timeseries of mean total cloud fractions over the ocean from 60°S to 60°N from various datasets (Black curves are Pv6.0. Red curves are CLARA-A3. Green curves are CERES EBAF. Blue curves are ERA5. Magenta curves are MERRA-2.) and their trends in total cloud fractions.

2.3.2.1. Statistical Experiment

Figure 2.7 shows two experiments to investigate consistency of trend in cloud fractions. Figure 2.7a provides the variations of trends when a single satellite is excluded from the timeseries, in order to assess the impact of that satellite to the long-term trend. The results are well-grouped, except for NOAA-07 in the case of water and ice clouds, although this difference is not significant.

The trends in total clouds in the experiment are similar to the trend in the overall timeseries, showing $-0.86 \pm 0.02\%$ per decade ($0.08 \pm 0.03\%$ per decade for water clouds and $-0.92 \pm 0.04\%$ per decade for ice clouds).

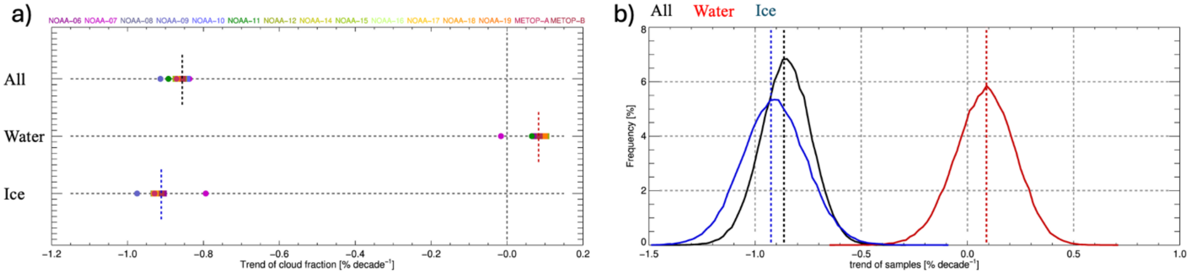

Figure 2.7: Trends after excluding single satellite (a) and histogram of trends of randomly sampled monthly mean cloud fractions [(b): Black curves are total cloud fractions. Red curves are water cloud fractions. Blue curves are ice cloud fractions.].

The second experiment calculates the trend using randomly sampled monthly mean cloud fractions to investigate the impacts of different time spans to the long-term trend, especially sensitivity of large-scale modes of variability such as ENSO. The 10% of all monthly mean cloud fractions are randomly selected, and the trend is calculated, repeating this process 3,000 times. Figure 2.7b shows the histogram of the trends from these 3,000 iterations. The histogram appears to follow a normal distribution, and the mean of distribution is similar to the overall timeseries trend, showing $-0.86 \pm 0.12\%$ per decade for total cloud ($0.08 \pm 0.14\%$ per decade for water clouds and $-0.91 \pm 0.15\%$ per decade for ice clouds).

Radiometric consistency between satellites also can impact this analysis of long-term trends. In particular, the flatness of the timeseries of total cloud in Figure 2.5a seems to start with the beginning of the AVHRR/3 era. Moreover, spectral response functions are slightly different between AVHRR instruments (Foster et al., 2023). To investigate radiometric consistency, an anomaly of brightness temperature at 11.0 μm, which is the most important infrared channel for cloud mask and cloud top assignments, is compared with anomaly of surface temperature from the ERA5 in Figure 2.8. The study area is from 10°S to 0°S and 144°W to 120°W, where the clear fraction is higher than the other ocean area so that it is likely to have more clear observations. The brightness temperature and surface temperature anomalies align well, except for two spikes in surface temperature observed in 1983 and 1998, where it rises by up to 2 K. This coincident with two very strong El ni$\tilde{n}$o events. As a result, there is no significant difference in brightness temperature at 11.0 μm between AVHRR versions over the last four decades.

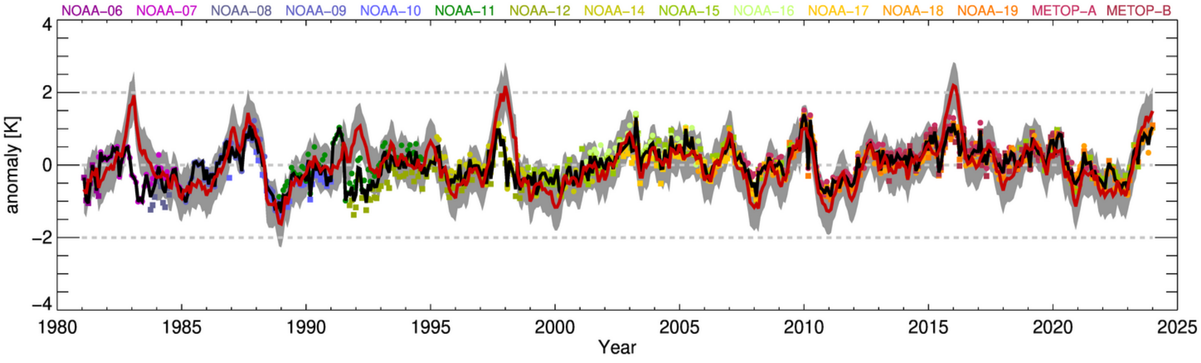

Figure 2.8: Anomalies of surface temperature from ERA5 reanalysis data and brightness temperature at 11.0 µm over clear sky from Pv6.0 level 2b dataset (Black curves are anomaly of monthly mean brightness temperatures from satellite average. Red curves are anomaly of monthly mean surface temperature from ERA5.). The area for calculating mean values ranges from 10°S to 0°S and 144°W to 120°W.

Figure 2.9 is last experiment for flatness of the timeseries, showing global maps of total, water, and ice cloud fraction trends derived from three groups of satellites. The left column represents cloud fraction trends from all satellites. Maps in the middle column are trends from AVHRR/1 and 2 which are onboard satellites from NOAA-06 to NOAA-14 (from 1981 to 2002). Trends in the right column are only from AVHRR/3 satellites, including NOAA-15 to NOAA-19 and MetOp satellites (1998 onward). For total cloud, significant decreases over the central Pacific Ocean and increases over the west coast of South America are seen in both AVHRR/1 and 2 (Figure 2.9b) and AVHRR/3 (Figure 2.9c). Global decreasing trends are more dominant in the AVHRR/3 era while AVHRR/1 and 2 shows an increase of cloud fractions over western Pacific Ocean and parts of middle latitude regions. The magnitudes of trend from AVHRR/1 and 2 are larger than AVHRR/3.

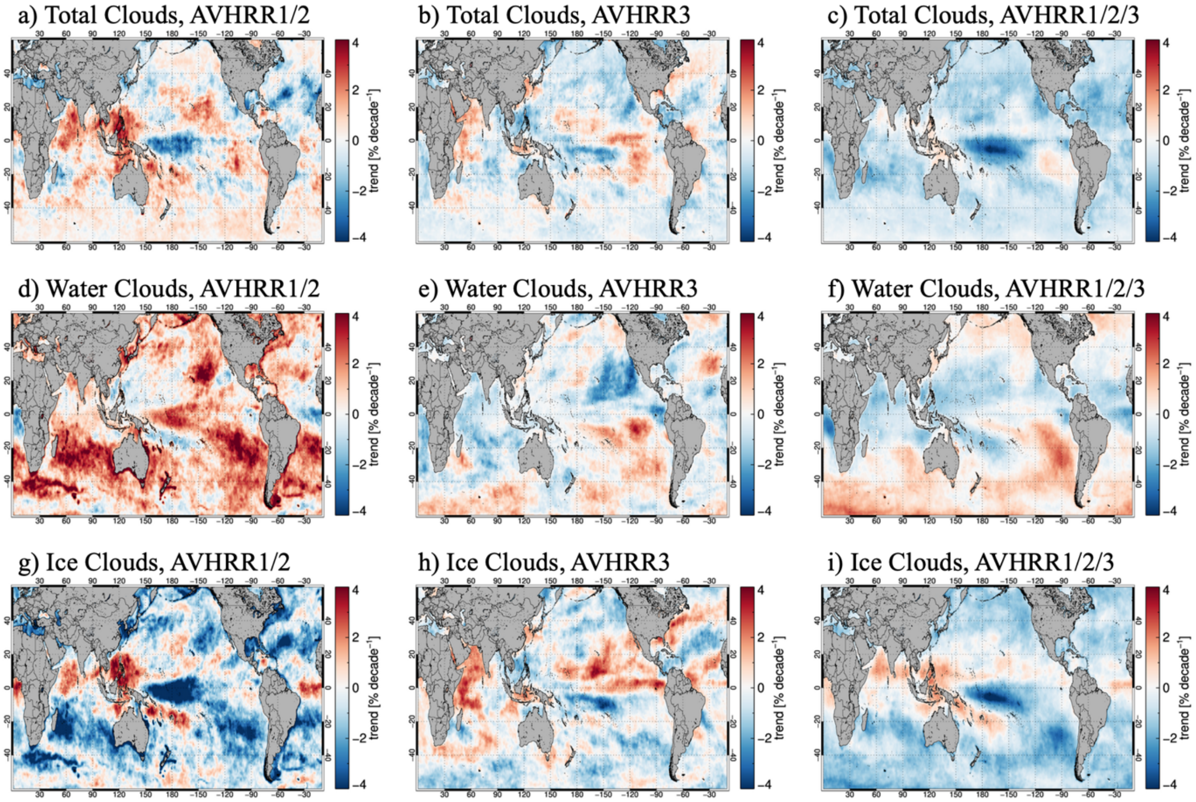

Figure 2.9: Map of trends of cloud fractions for different cloud phases (Top is total clouds. Middle is water cloud fractions. Bottom is ice cloud fractions.). Left column is from combination of AVHRR/1 and AVHRR/2 from NOAA-06 to NOAA-14. Middle column is from AVHRR/3 from NOAA-15 to NOAA-19 in addition to MetOp satellites. Right column is from all satellites.

For water clouds and ice clouds, most of ocean areas shows similar the patterns between AVHRR/1 and 2 and AVHRR/3 except for west coast of North America and Southern Indian Ocean although the magnitudes from AVHRR/1 and 2 are larger than AVHRR/3. Increases in water clouds are dominant for both AVHRR/1 and 2 (Figure 2.9e) and AVHRR/3 (Figure 2.9f) except for Arabian sea and west coast of North America at AVHRR/3. Magnitude of AVHRR/1 and 2 is higher than AVHRR/3 and it can contribute to the increase of total cloud fractions over middle latitude. Last, ice cloud trends are more similar except for over the western Pacific Ocean and the ITCZ regions.

AVHRR1/ and 2 show an increase of ice clouds over western Pacific Ocean while AVHRR/3 show an increasing trend in the Eastern Pacific Ocean. It can be caused by ENSO status. As a result, over some areas, spatial patterns of trends are similar between AVHRR/1 and 2 and AVHRR/3 while there is a significant difference in spatial pattern and magnitude in cloud fraction trends between from 1981 to 2002 (AVHRR/ 1 and 2) and from 1998 to 2023 (AVHRR/3). This highlights the importance of further investigating causes of these issues.

2.3.3 Monthly mean cloud fractions

Figure 2.10 shows box plots of the monthly mean of total, water, and ice cloud fractions over the ocean from 60°S to 60°N and monthly mean trends for the last four decades. Total cloud fractions range from 72% in March to 80% in December (Figure 2.10a). The 5-years mean of total cloud fractions show a consistent decreasing trend for all months. Specifically, the mean value from 2021 to 2023 shows the lowest across most months. The water clouds show a strong seasonality from 29% to 34%, with lower values in the early months of the year and higher values around June to August (Figure 2.10b). The variations of water clouds are the smallest and the 5-years mean tendency is also not noticeable compared to total and ice clouds. The ice cloud fraction ranges from 41% around mid-year (June to August) to 50% at the beginning and end of the year (Figure 2.10c), which is the opposite shape of water clouds seasonality. The 5-year average shows a strong tendency of decrease.

The trends in monthly mean total, water, and ice clouds are shown in Figure 2.10d. The range of trends in total clouds is from −0.81% per decade in June to −0.92% in October. The trends of water clouds are always positive from 0.01% per decade in March and 0.23% per decade in

September. Last, the trends of ice clouds are highest in September as -1.07% per decade and lowest in March as -0.80% per decade. The seasonal variations in trends are not noticeable compared to the seasonal variations in mean cloud fractions.

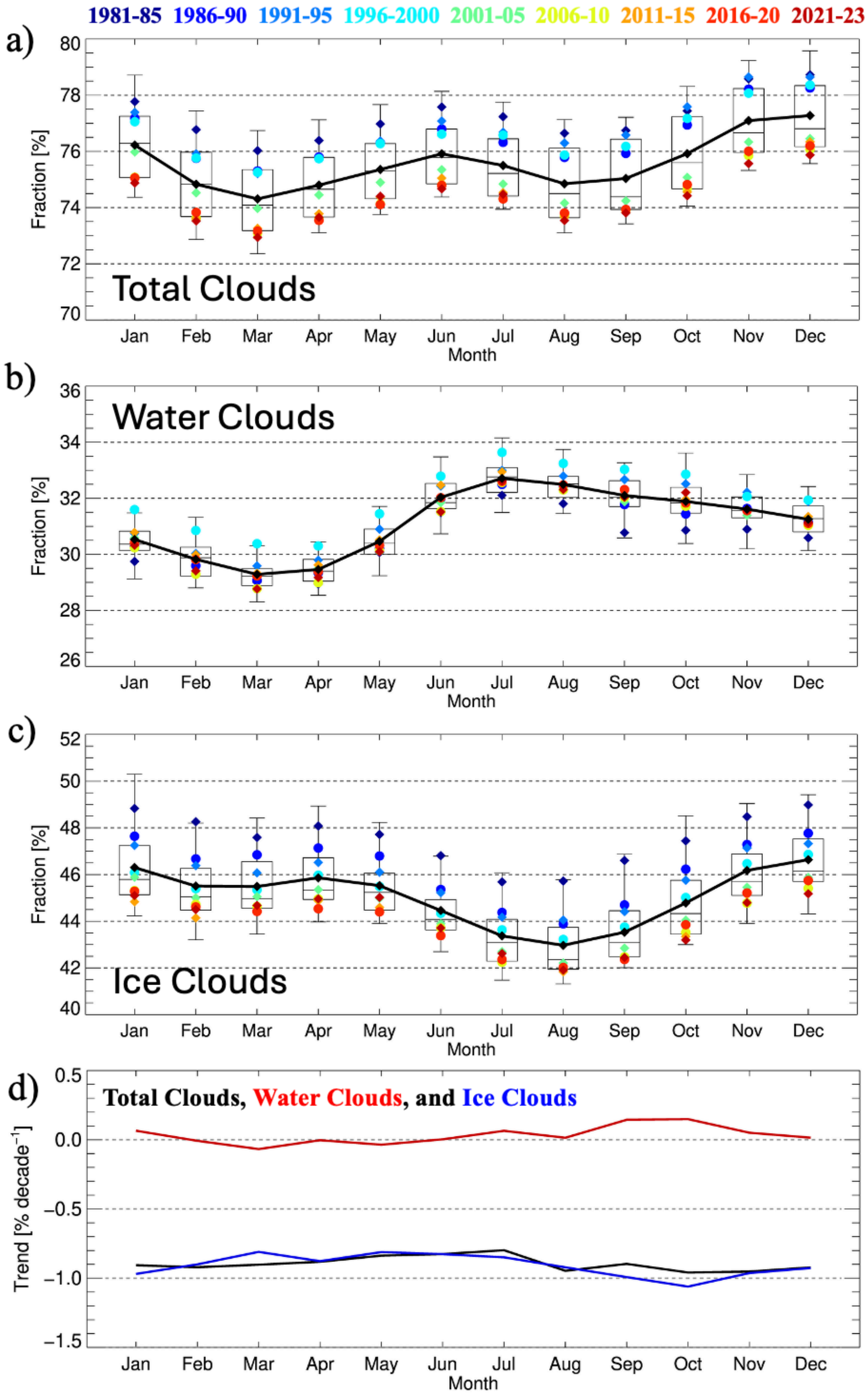

Figure 2.10: Box plots of mean cloud fractions (a: total clouds, b: water clouds, and c: ice clouds). The colors represent the time span used to calculate mean value. Black curves are the mean for the entire period. d) is the monthly trend of mean cloud fractions (Black curves are total clouds. Red curves are water clouds. Blue curves are ice clouds.).

Figure 2.11 presents the trends in monthly mean cloud fractions across different latitude ranges. From 0°N to 20°N, the seasonal variations in trend magnitudes are relatively weak. Ice cloud trends range from −0.3% to 0.4% per decade. Total cloud trends are negative throughout the year, primarily due to significant decreases in water clouds. From 20°N to 40°N, this region exhibits stronger seasonality compared to the equator. Total cloud fraction shows a predominantly decreasing trend, ranging from −1.0% to −1.5% per decade. Water clouds increase slightly from January to March but reach a maximum decline in August at −0.9% per decade. Ice clouds show their largest decrease in February (−1.6% per decade) and the smallest in July (−0.5% per decade). From 40°N to 60°N, ice clouds also show significant declines, ranging from −0.8% to −1.5% per decade. Water clouds increase throughout the year, except in July and August. The total cloud trends remain negative, varying between −0.8% to −1.0% per decade.

From 0°S to 20°S, all cloud phases show decreasing trends across all months. From 20°N to 40°N, water clouds show significant increases, particularly from July to September, likely influenced by maritime low cloud regimes. Meanwhile, ice clouds decline during the same period. Overall, total cloud fraction decreases throughout the year. From 40°S to 60°S, the trends in all cloud phases are constant over the months. Increases in water cloud are observed, as a rate from 0.6% per decade to 1.0% per decade, while ice clouds decrease from −1.2% to −1.6% per decade. Total clouds decline slightly, ranging from −0.5% to −0.6% per decade.

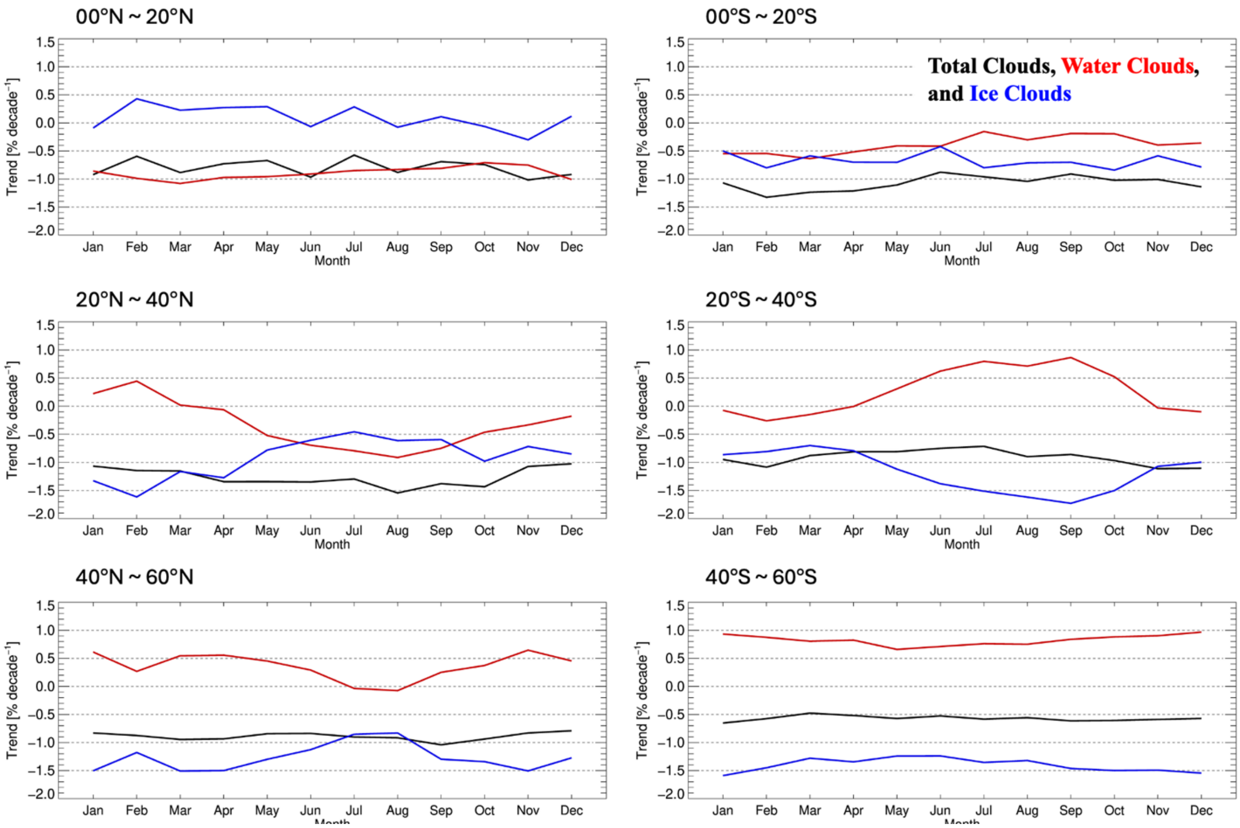

Figure 2.11: Monthly trend of mean cloud fractions for different latitude ranges (Black curves are total clouds. Red curves are water clouds. Blue curves are ice clouds.).

2.3.4. Zonal mean cloud fractions

Figure 2.12a and 2.12b provide zonal mean fractions of total, water, and ice clouds and zonal mean cloud fraction trends over the ocean. Total cloud fractions are highest in the mid-latitudes, ranging from 90% to 95%, and lowest at 20°N and 5°S, around 55% (Figure 2.12a). Decreasing trends in total cloud fractions are observed across all latitudes, with a maximum of −1.35% per decade around 4.5°S, corresponding to significant decreasing trends over the central Pacific Ocean, as shown in Figure 2.3. Water clouds are lowest as 15% in the ITCZ and highest as 45% in the southern mid-latitudes. From 15°S to 30°N, water clouds decrease, with a maximum of −1.11%

per decade around 13.5°N. Above 30° latitude, the magnitude of water cloud fractions increases with latitude, reaching a maximum of 1.37% per decade at 60°S. Ice cloud fractions are highest at the tropics and mid-latitudes. Increasing trends are observed only at the tropics, while decreasing trends are dominant at all other latitudes. Because of different cloud radiative effects depending on cloud types and regions as well as latitudes, the impacts of these changes on the Earth's radiation budget should be investigated.

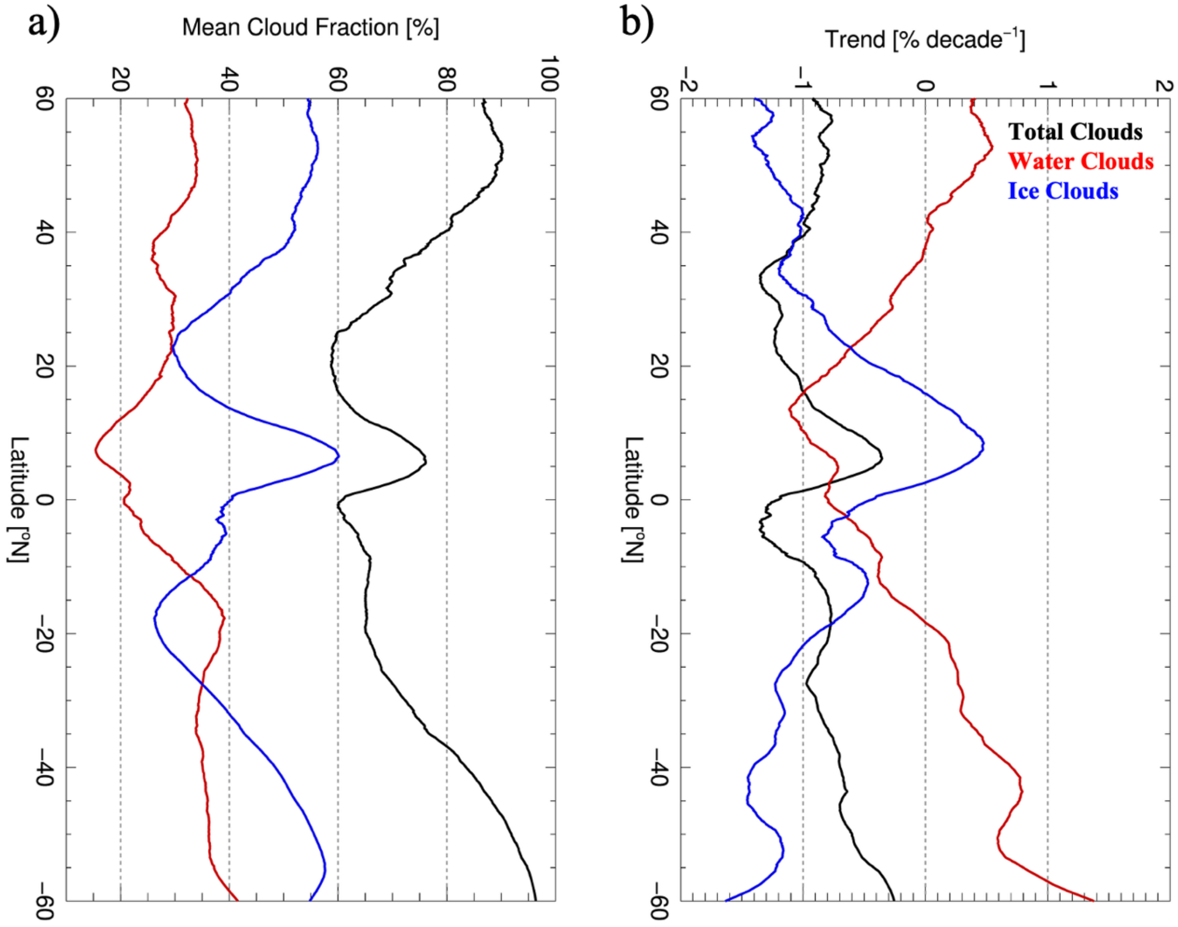

Figure 2.12: Zonal mean plot of cloud fractions (a) and zonal mean cloud fraction trend plot (b) from 1981 to 2023. The colors represent the cloud phase (Black curves are total clouds. Red curves are water clouds. Blue curves are ice clouds.).

2.4 Cloud Top Properties

In the net TOA flux of radiation calculation terms, cloud top properties, especially cloud top temperature, influence the amount of longwave radiation. Warm cloud top temperature (low clouds) can cool the atmosphere by increasing the downward emission of longwave radiation, while cold cloud top temperature (high clouds) warms it by decreasing the upward emission of longwave radiation (Slingo and Slingo, 1988). Moreover, cloud top properties have been used in various atmospheric applications such as estimating precipitation (Zeng, 1999; Janowiak and Arkin, 1991), evaluating a lightning parametrization (Karagiannidis et al., 2019; Wong et al., 2013), and investigating direct and indirect effects of aerosol associated with cloud top properties (Koren et al., 2010; Sekiguchi et al., 2003; Massie et al., 2007; Yuan et al., 2008).

2.4.1 Map of cloud top properties

Regional mean and trend of cloud top assignments over four decades from Pv6.0 are shown in Figure 2.13. The regional patterns between cloud top assignments are comparable because cloud top heights are calculated using cloud top temperature retrieved from ACHA algorithm and numerical weather prediction model. In tropical and subtropical regions, changes in cloud phases are highly correlated with changes in cloud top assignments. The mean cloud top height is the highest over western Pacific Ocean and ITCZ regions, reaching around 10 to 12 km, where ice clouds are dominant due to strong convection (Figure 2.13a). These regions exhibit noticeable increasing trends in cloud top height, with a maximum of 0.42 km per decade, associated with the rise of convective cloud under global warming conditions (Bony et al., 2016). In contrast, the regions dominated by maritime low clouds that cloud top heights are below 3 km, such as the west coast of South America, show decreasing trends in cloud top heights. These decreases appear to be related to significant increases in water clouds and decreases in ice clouds over these regions. Also, decreases in cloud top height are observed over the central Pacific Ocean due to the substantial decreases in ice clouds, as shown in Figure 2.2, with a maximum of −0.53 km per decade. However, in the midlatitudes, cloud top heights show increasing trends despite increases in water clouds and decreases in ice clouds.

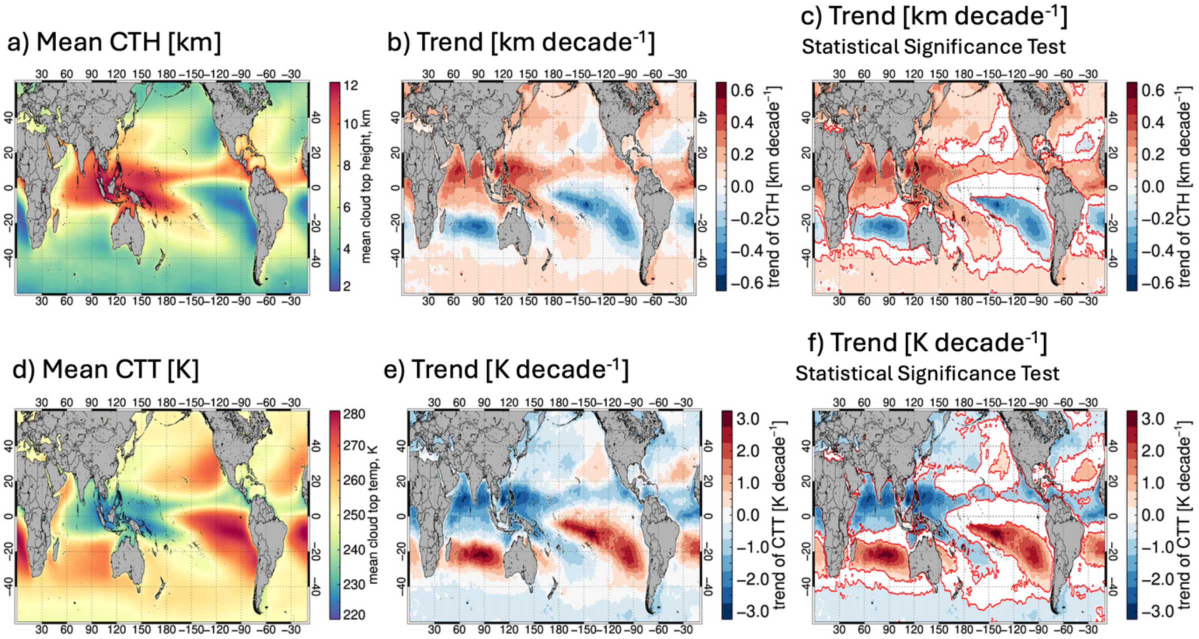

Figure 2.13: Map of mean cloud top properties (a: cloud top height [km] and d: cloud top temperature [K]) and trend (b: cloud top height and e: cloud top temperature) from 1981 to 2023. Statistical significance test shows area that are not statistically significant are blanked and area surrounded by a red line is statistically significant (c: cloud top height and f: cloud top temperature).

The mean cloud top temperature over western Pacific Ocean and ITCZ is approximately 230 K and has cooled, decreasing by 3 K per decade. This indicates that the warming effects of high clouds could be strengthening over these regions (Weaver et al., 2024). The mean cloud top temperatures in regions where water clouds are dominant range from 260 to 280 K. These regions show increasing trends in cloud top temperature for the same reason that cloud top height decreases. Similar to cloud top height, cloud top temperature shows decreasing trends in the midlatitudes while the mean cloud top temperature is around 250 K.

Figure 2.14 shows the mean and trend of cloud top temperature from three satellite-based CDRs (Pv6.0, CLARA-A3, and CERES EBAF). The mean cloud top temperatures are lowest over western Pacific Ocean and the ITCZ, but the mean values are different between datasets due to the different retrieval methods, spectral information used in algorithm and cloud-conservative approaches between datasets. The mean cloud top temperature over these regions ranges from 220 K to 230 K in Pv6.0, 200 K to 210 K in CLARA-A3, and 230 K to 240 K in CERES EBAF. The mean cloud top temperatures are highest over the regions dominated by maritime low clouds, including the west coast of South America. The mean values also differ between satellite-based CDRs, with CERES EBAF being higher than the others, although the differences are smaller compared to the ITCZ regions. Lastly, noticeable differences in cloud top temperatures are also observed over the midlatitudes, with CERES showing warmer cloud top temperatures than the other datasets.

Trends in cloud top temperature over the last four decades show similar patterns in Pv6.0 and CLARA-A3, including decreasing trends over western Pacific Ocean, where convective clouds are dominant. The magnitudes of decreases over this region range from 2 K per decade to 3 K per decade. Over the central and eastern central Pacific Ocean, both Pv6.0 and CLARA-A3 show increases in cloud top temperature, with CLARA-A3 exhibiting larger magnitude in trends. Other regions, where maritime low clouds are dominant, also show increasing trends in cloud top temperature. From 2000 to 2023, the patterns of trends remain consistent with patterns over last four decade except for midlatitude regions. Over these two decades, cloud top temperatures in these areas have increased.

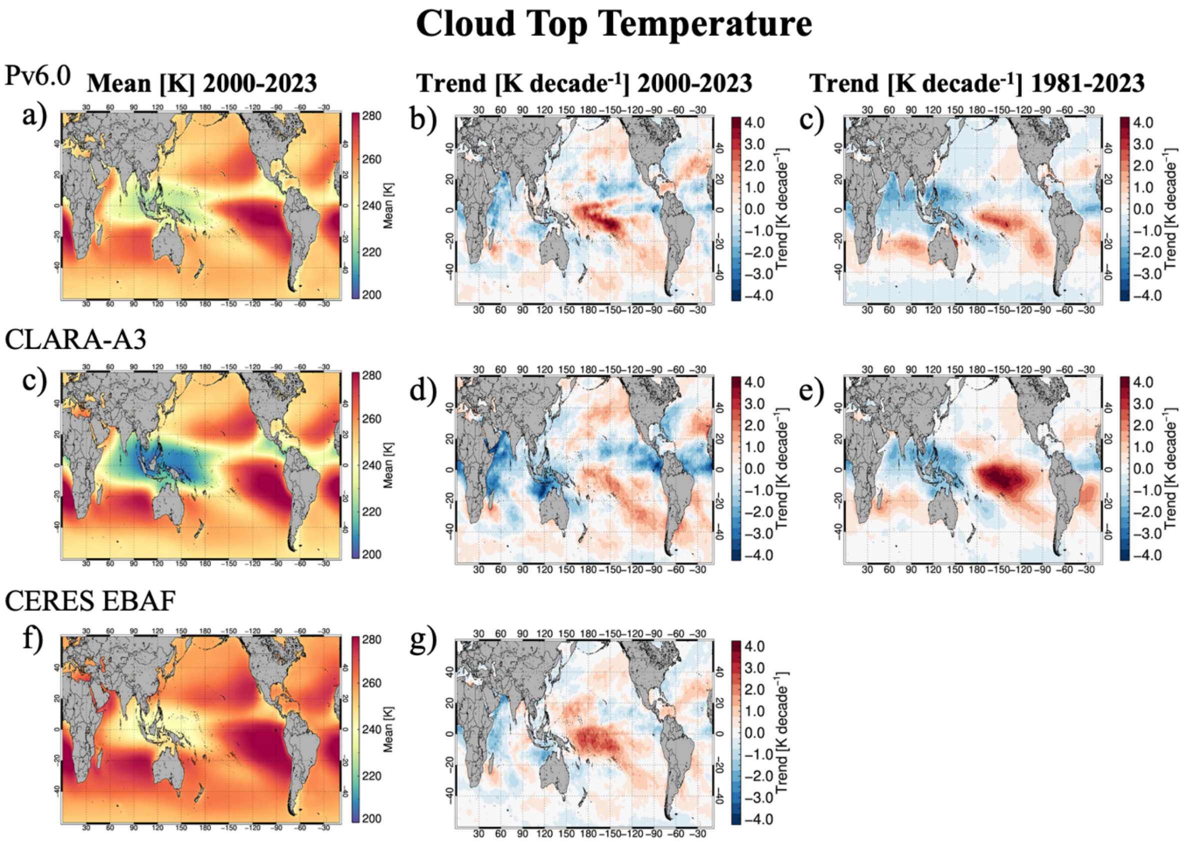

Figure 2.14: Map of mean cloud top temperature from 2000 to 2023 (left column; K) and trend of cloud top temperature (middle column; K per decade) from 2000 to 2023. Then trends of cloud top temperature from Pv6.0 and CLARA-A3 over last four decades are showing at right column.

2.4.2. Timeseries of mean cloud top properties

Figure 2.15 provides timeseries of mean cloud top height, temperature, and pressure over the ocean from 60°S to 60°N. All cloud top assignments show strong seasonality, with average cloud top heights being high in April and low in July, and cloud top temperature and pressure being low in April and high in July. This is also related to the seasonality of cloud phase fractions mentioned above. Cloud top height ranges from 5.5 km to 6.7 km (6.03 ± 0.16 km) and shows an increasing trend of 0.056 km per decade (Figure 10a). Cloud top temperature varies between 251 K to 257 K (253.90 ± 0.96 K), with a decreasing trend of 0.082 K per decade (Figure 10b). Monthly mean cloud top pressure ranges from 520 hPa to 580 hPa (554.06 ± 8.84 hPa) and has a decreasing trend of 0.915 hPa per decade (Figure 10c).

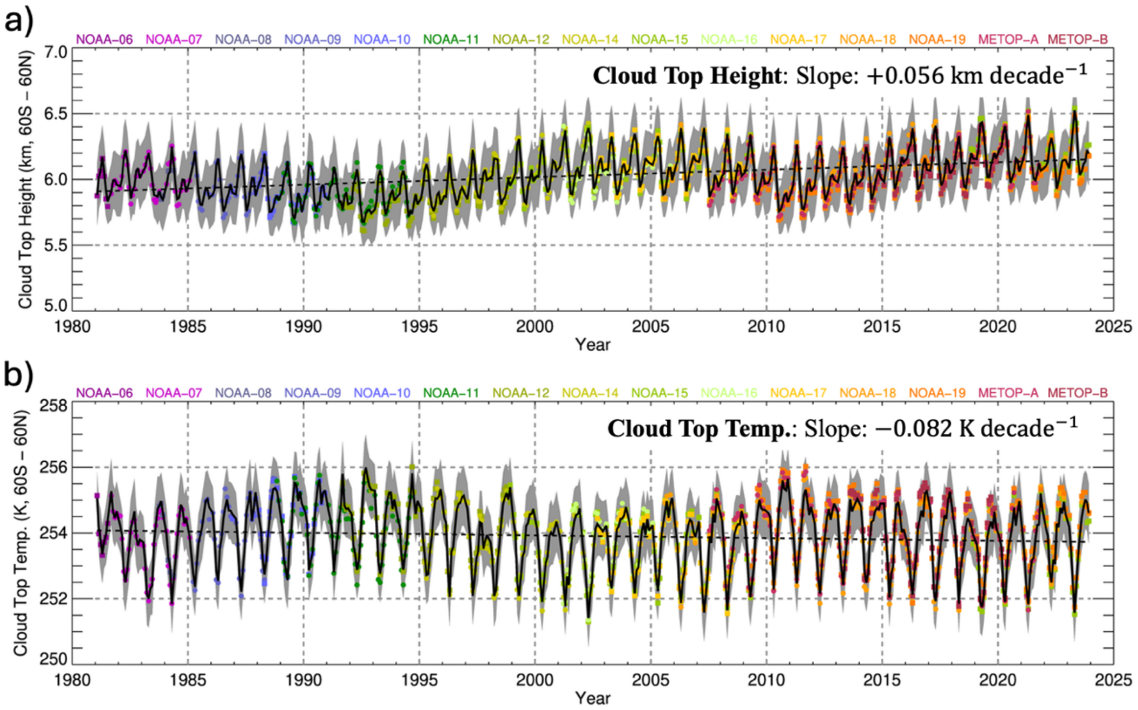

Figure 2.15: Timeseries of mean cloud top height (a) and temperature (b) over the ocean from 60°S to 60°N from Pv6.0. Colors represent POES satellites.

2.4.3 Monthly mean cloud top properties

Monthly mean cloud top assignments over the ocean from 60°S to 60°N are shown in Figure 11a-c. Mean cloud top temperatures are lowest in April and highest in September (254.1 ± 1.0 K), showing a strong seasonality (Figure 2.16b). The shape of seasonality follows the monthly variations of cloud phase fractions (Figure 2.10). The 5-year mean trends show a decrease in cloud top temperature, although it is not as clear as the trend of cloud fractions. On the other hand, cloud top height (pressure) shows identical trends with an increase (decrease) for all month, with a mean value of 6.0 ± 0.2 km (556.2. ± 9.3 hPa) and the mean from 2021 to 2023 shows higher (lower) values than previous years (Figure 2.16a and 2.16c).

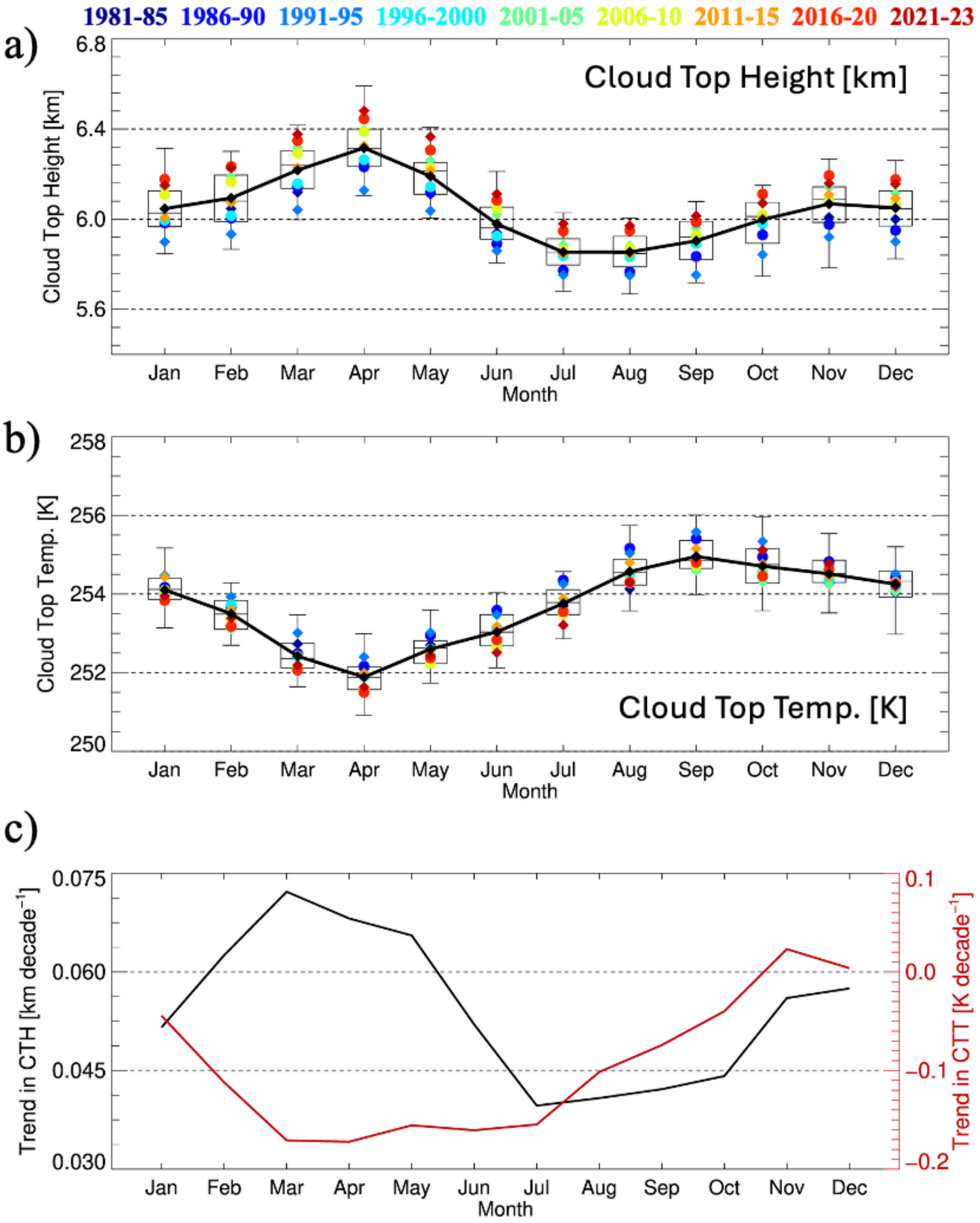

Figure 2.16: Box plot of monthly mean cloud top properties from Pv6.0 (a: cloud top height [km] and b: cloud top temperature [K]). The colors represent the time span used to calculate the mean values. Black curves are the mean for the entire period. The monthly mean trends (c) in cloud top height (black) and cloud top temperature (red) are from 1981 to 2023.

2.4.4 Zonal mean cloud top properties

Zonal mean and zonal mean trend plots of cloud top assignments are shown in Figure 2.17. Mean cloud top height is highest at 5°N, around 9.8 km, and lowest at the 60°, at approximately 4 km (Figure 2.17a). The cloud top heights have increased over the past four decades at all latitudes, except between 15°S and 30°S, where maritime low clouds are dominant including off the west coast of South America. In the midlatitudes, cloud top heights have increased despite the increase in water clouds and decreases in ice clouds. While cloud top height is highest near the equator and decrease consistently with latitude, the pattern of mean cloud top temperature is different. Cloud top temperatures range from 237 K at the equator to 262 K at 20°S. Above 20°, the mean cloud top temperatures increase with latitude. A decreasing trend of cloud top temperature is dominant, and it is particularly noticeable at 10°N. The patterns of cloud top temperature are similar to those of cloud top heights, ranging from -1 K per decade at 10°N to +0.5 K per decade at 20°S (Figure 2.17b).

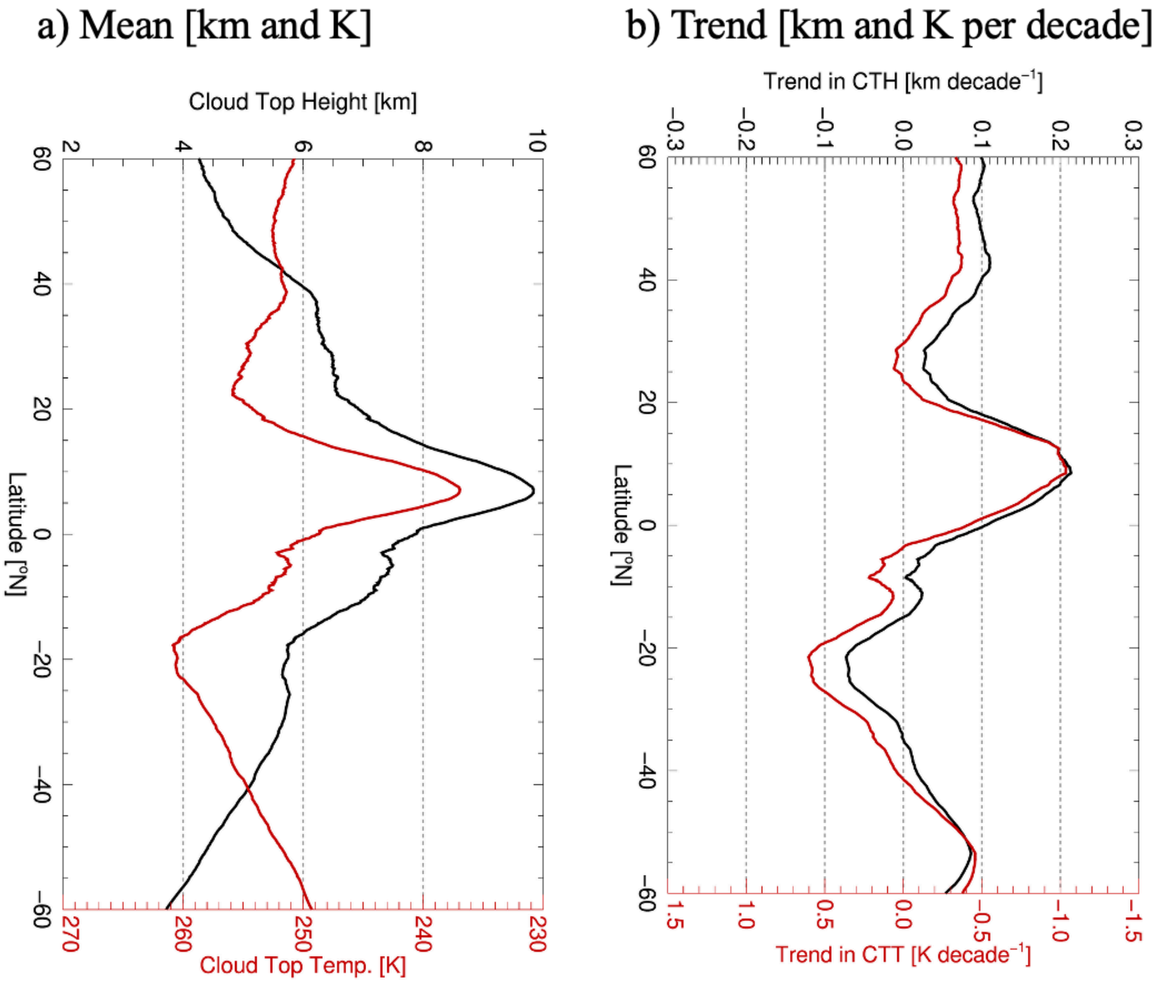

Figure 2.17: Zonal mean plot (a) and zonal mean trend plot (b) of cloud top height (black) and temperature (red) from 1981 to 2023 from Pv6.0.

2.4.5 Relationship with tropopause heights

To investigate the relationship between changes in cloud top height and tropopause height, the zonal mean and trend of fractions as a function of cloud top height over the ocean from 1981 to 2023 are shown in Figure 13a and 13b. At the equator, cloud top heights reach up to 12 km and gradually decrease toward the mid-latitudes (Figure 2.18a). From 0° to 20°S, the fractions of low cloud top heights are higher than at other latitudes due to the presence of marine stratocumulus clouds. Cloud top heights are confined to a very low range of 4 to 6 km from 40° to 60°. Figure 2.18b provides the trends of fractions of cloud top heights. All latitudes show an increase in fractions at higher cloud top heights. Also, there is an increase in fractions over the marine low cloud regimes from 0° to 40°S, which is associated with increases in water cloud fraction discussed above.

To compare the changes in cloud top heights, mean and trend of tropopause height along the latitude are shown in Figure 2.18c and 2.18b. The tropopause height is obtained from MERRA-2. Xian and Homeyer (2019) showed good agreement between radiosondes and MERRA-2 in terms of thermodynamic vertical profile and tropopause height. The mean tropopause height ranges from 16 to 17 km between 20°S to 20°N and gradually decreases with latitude, reaching 9 km at 60°S and 60°N. The trends of tropopause height show an increase over the last four decades across all latitudes, with the most remarkable increase occurring in the tropics. Especially, over the tropics, where convective clouds are dominant, increase in tropopause heights can be associated with increases in cloud top heights.

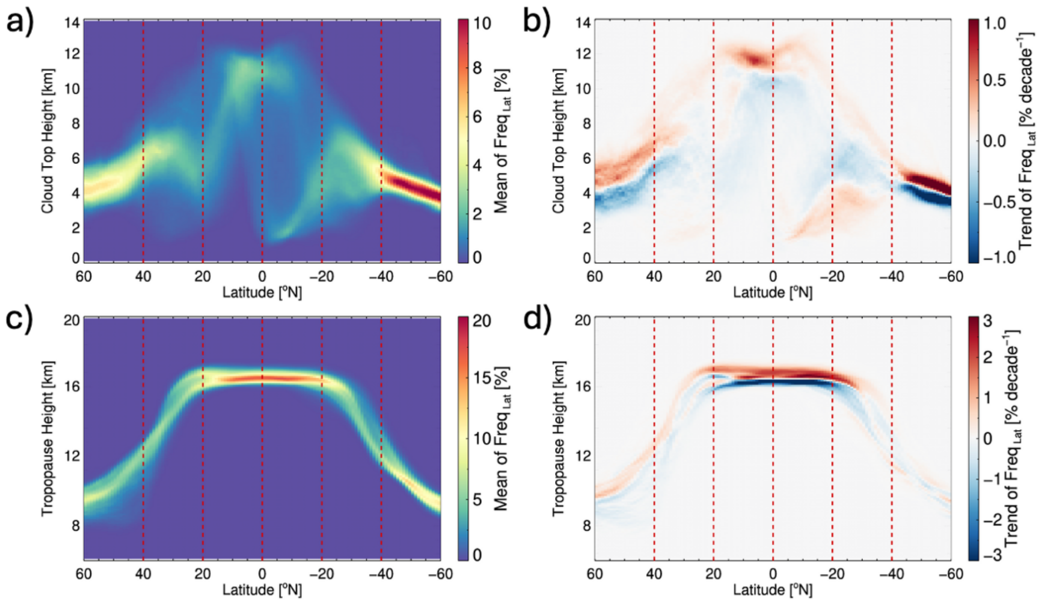

Figure 2.18: Zonal plots of frequency of cloud top height from Pv6.0 and tropopause height from MERRA-2 data over the ocean from 1981 to 2023. Left column is mean frequency and right column is trend of frequency.

2.5 Cloud Optical Depth

COD, also known as cloud optical thickness, is a measure of how much a cloud attenuates sunlight passing through it. It is a dimensionless quantity that quantifies the cloud's ability to absorb and scatter radiation, playing a crucial role in estimating the net TOA shortwave flux. Many atmospheric studies have highlighted the importance of COD in various atmospheric applications, including its influence on radiative forcing (Ogunjobi et al., 2004; Jensen et al., 1994; Yang et al., 2010; Curry and Ebert, 1992; Prabhakara et al., 1993), its role in climate feedback (Ceppi et al., 2017; Gordon and Klein, 2014; Roeckner et al., 1987), and its relationship with cloud drop size and precipitation (Yuan et al., 2008; Stenz et al., 2016). Despite its significance, COD remains one of the most poorly observed climate variables over the ocean. Satellite observations of COD are therefore essential for atmospheric research, particularly for studies that rely on COD and other interrelated climate variables.

2.5.1 Map of cloud optical depth

Figure 2.19 shows a map of the mean COD and its trend from Pv6.0 and CERES EBAF. The mean COD is highest over the ITCZ region due to the strong convection and midlatitude where thick stratiform clouds dominate. However, CERES EBAF shows lower mean COD values compared to Pv6.0. This discrepancy suggests that absolute COD values may differ between Pv6.0 and CERES EBAF due to variations in spectral availability, retrieval method, and local overpass time. The trend in COD from Pv6.0 from 1981 to 2023 shows a predominant increase across most of the globe, except for certain regions such as the central Pacific Ocean and the east coast of North America. The trend in COD from Pv6.0 from 2000 to 2023 exhibits a similar pattern, with increasing trends dominating globally. In contrast, the trend in COD from CERES EBAF from 2000 to 2023 shows decreases in certain regions, particularly over the Northern midlatitudes. Despite these differences, both datasets indicate significant increases in COD over the southeastern Pacific Ocean, as we discussed in chapter 1.

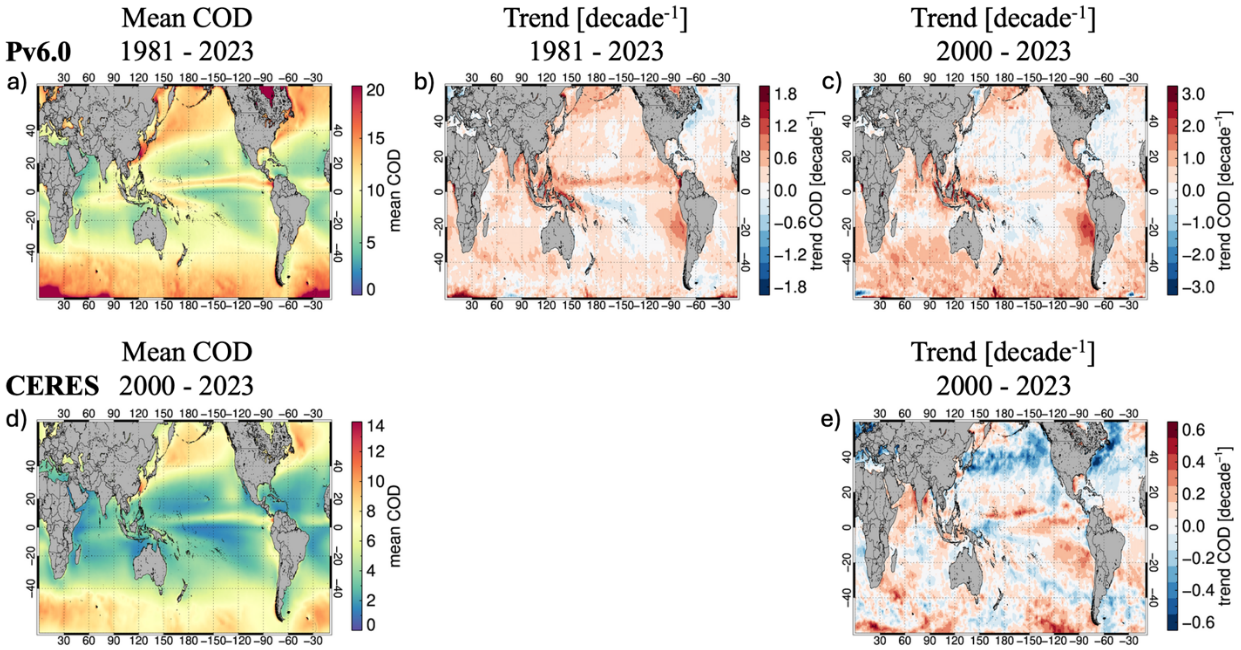

Figure 2.19: a) Map of mean cloud optical depth from 1981 to 2023 from Pv6.0. b) trend of cloud optical depth from 1981 to 2023 from Pv6.0. c) trend of cloud optical depth from 2000 to 2023 from Pv6.0. d) mean cloud optical depth from 2000 to 2023 from CERES EBAF. e) trend of cloud optical depth from 2000 to 2023 from CERES EBAF.

Chapter 3

How have observed changes in clouds influenced cloud radiative effects?

3.1 Introduction

Clouds play a critical role in Earth’s radiation budget by modulating incoming solar radiation (shortwave) and outgoing longwave radiation from the surface and cloud. This modulation, known as the CRE, represents the difference in radiative fluxes between all-sky and clear-sky conditions at the top of the atmosphere. CRE serves as a key diagnostic for understanding how clouds influence climate by exerting both cooling effects through the reflection of solar radiation and warming effects by trapping outgoing longwave radiation. The magnitude and sign of CRE vary spatially and temporally depending on cloud type, altitude, optical properties, and regional atmospheric conditions. Accurate quantification of CRE is essential for detecting climate feedback, evaluating model performance, and improving projections of future climate change. The large variability of net CRE across climate simulations is shown in Appendix A. In this chapter, we analyze the characteristics of CRE using satellite observations over the southeastern Pacific Ocean, with a focus on identifying key cloud properties associated with changes in CRE. This work has been submitted as part of Seo et al. (2025c).

3.2 Outgoing Radiation

3.2.1 Outgoing shortwave radiation

Outgoing shortwave radiation (OSR) represents the portion of solar radiation that is reflected back into space by the Earth’s surface, atmosphere, and clouds. Clouds are highly reflective and contribute significantly to OSR over the ocean because the ocean’s albedo is generally low, ranging from 2% to 10%. Figure 3.1 shows the mean OSR for clear sky, all sky, and CRE. The mean OSR for clear sky conditions remains constant across all latitudes, except in certain regions where ice cover is present during winter. The mean OSR for all sky conditions is high in area with a high cloud fraction. The CRE values are all negative due to the higher albedo of clouds compared to the ocean surface, indicating the cooling effect of clouds except in certain area where cloud fractions are low.

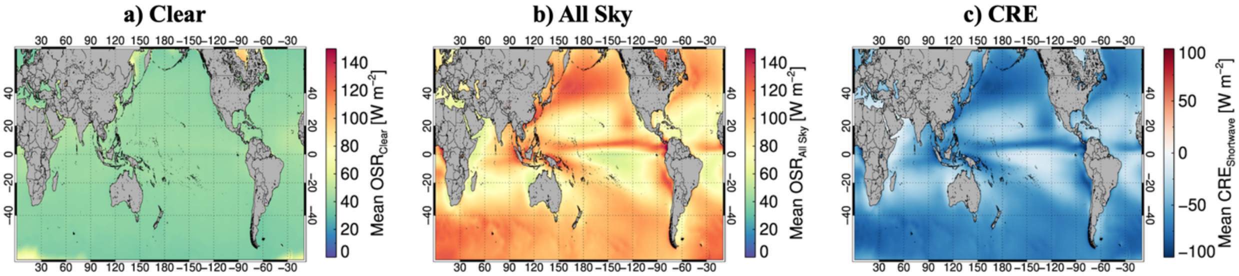

Figure 3.1: Map of mean outgoing shortwave radiation (W·m^{-2}) for (a) clear sky, (b) all sky, and (c) CRE from 2000 to 2023 based on CERES EBAF dataset.

3.2.2 Outgoing Longwave Radiation

Outgoing longwave radiation (OLR) refers to the thermal infrared radiation emitted by the Earth and its atmosphere that escapes into space. Warmer regions emit more OLR, while colder regions emit less. High altitude clouds, being colder, emit little OLR and trap heat below them, contributing to the greenhouse effect. Figure 3.2 shows the mean OLR for clear sky, all sky, and CRE conditions. The mean OLR for clear sky conditions is highest at the equator and decrease toward the poles due to variations in sea surface temperature. The mean OLR for all sky conditions is higher in regions where low clouds are prevalent. CRE values are all positive due to the greenhouse effect of clouds, with significant impacts observed in the ITCZ, western Pacific Ocean, and midlatitudes. However, areas dominated by low clouds exhibit a relatively weak warming effect.

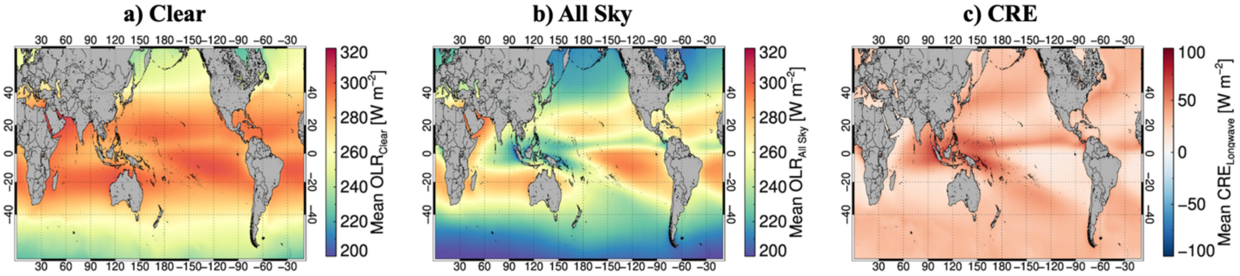

Figure 3.2: Map of mean outgoing longwave radiation (W·m^{-2}) for (a) clear sky, (b) all sky, and (c) CRE from 2000 to 2023 based on CERES EBAF dataset.

3.2.3 Net Radiation

In this study, net radiation is defined as the sum of outgoing shortwave and longwave radiation. Figure 3.3 shows the mean outgoing net radiation from 2000 to 2023 for clear sky, all sky, and CRE conditions. The mean outgoing net radiation for clear sky is highest at the equatore due to the strong emission of longwave radiation. For all sky conditions, the mean outgoing net radiation is highest over maritime low cloud regions, where both shortwave and longwave radiation are strongly reflected or emitted. As a result, the net CRE has the strongest cooling effects over these regions and midlatitudes.

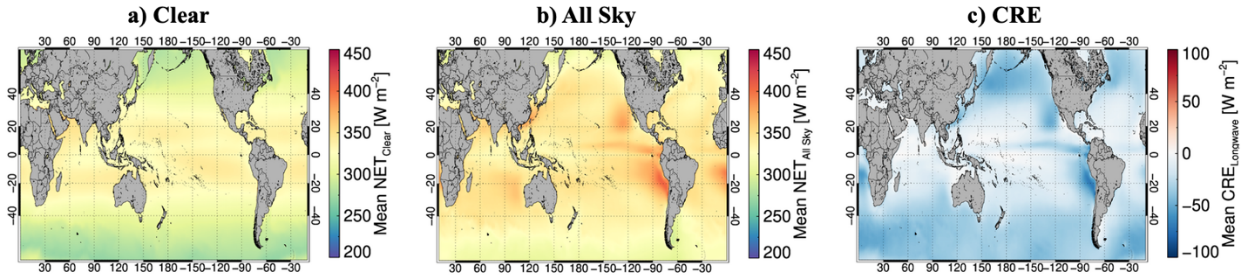

Figure 3.3: Map of mean outgoing net radiation (W·m^{-2}) for (a) clear sky, (b) all sky, and (c) CRE from 2000 to 2023 based on CERES EBAF dataset.

Figure 3.4 shows the trends in outgoing net radiation for clear sky, all sky, and CRE from 2000 to 2023, based on CERES EBAF dataset. The trends are calculated after subtracting the monthly mean values to account for seasonal variations in solar radiation and sea surface temperature. The trends for clear sky are relatively weak, as the main factors influencing changes are sea surface temperature, solar intensity and ice cover at midlatitudes. In contrast, trends for all sky show a predominant decrease due to the decline in cloud fraction, as seen in Figure 2.3, which reflects a reduction in the albedo effect of clouds. Consequently, net CRE exhibits an increasing trend, contributing to surface warming by allowing more solar radiation to reach the surface. However, the southeastern Pacific Ocean shows significant decreasing trends, indicating a strengthening of cloud induced cooling effects, as discussed in Chapter 1. The increasing cooling effects of clouds are particularly important in the context of global warming. Therefore, we will focus specifically on these regions (from 30°S to 10°S, and from 120°W to 70°W).

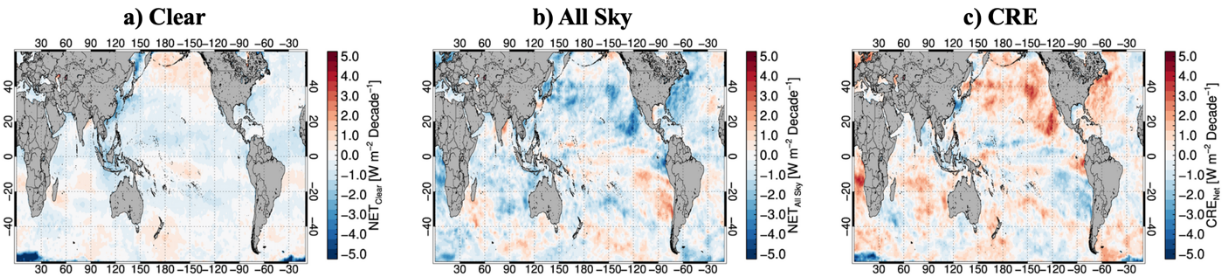

Figure 3.4: Map of trend in outgoing net radiation (W·m^{-2}) for (a) clear sky, (b) all sky, and (c) CRE from 2000 to 2023 based on CERES EBAF dataset.

Figure 3.5 shows a map of trends in CRE for shortwave, longwave, and net radiation. The shortwave CRE shows an overall increasing trend due to reduced reflected solar radiation caused by a decrease in cloud fraction. This trend is particularly notable over the central Pacific Ocean and midlatitudes. In contrast, a decreasing trend is observed in certain regions, including western Pacific Ocean and southeastern Pacific Ocean, where cloud fractions have increased. The longwave CRE shows a decreasing trend for the same reason as the shortwave CRE. Over the southeastern Pacific Ocean, changes in longwave CRE are minimal due to presence of low altitude clouds with warm cloud top temperature, which are similar to the sea surface temperature. Therefore, the strengthening of cooling effects in the study area is primarily driven by decreases in shortwave CRE.

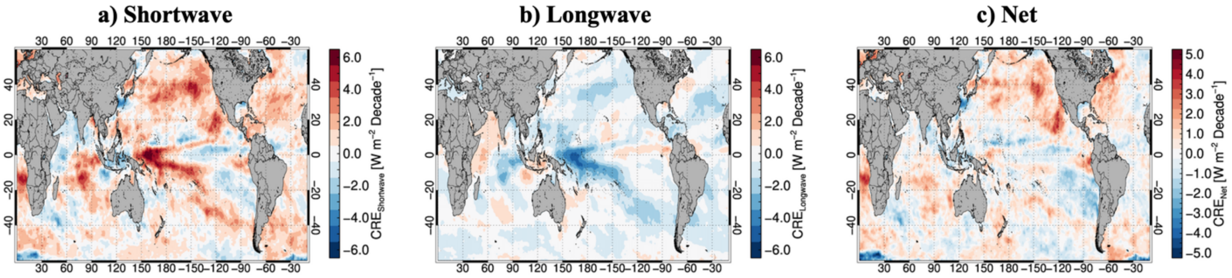

Figure 3.5: Map of trend in CRE (W·m^{-2}) for (a) shortwave, (b) longwave, and (c) net radiation from 2000 to 2023 based on CERES EBAF dataset.

3.3 Relationship between CRE and cloud fractions

Figure 3.6 shows the trends of net CRE and cloud fractions for total, water, and ice clouds from 2000 to 2023 over the study area. A decreasing trend in net CRE, or a strengthening of cooling effects, is observed in regions dominated by water clouds. In these areas, total cloud fractions are also increasing, mainly due to a rise in water cloud fractions and a decline in ice cloud fractions. This suggests that the enhanced cooling effects are primarily driven by changes in cloud fractions, particularly the increase in water clouds.

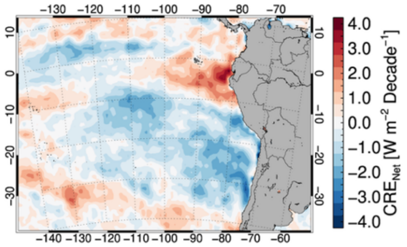

a) Net CRE

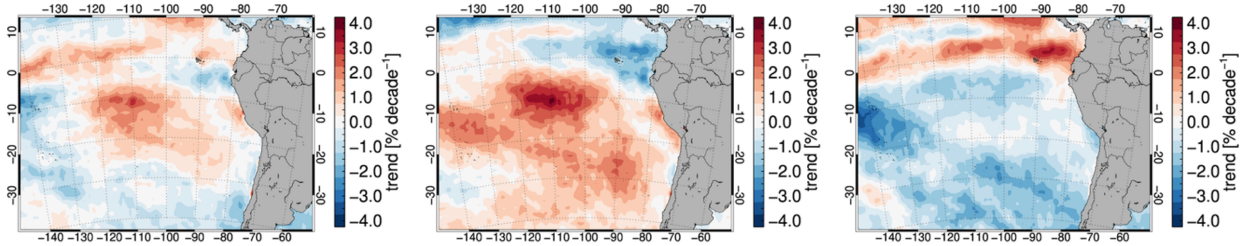

b) Total Clouds

c) Water Clouds

d) Ice Clouds

Figure 3.6: Map of trend in (a) net CRE (Wm^{-2}) from CERES EBAF dataset and cloud fraction for (a) total clouds, (b) water clouds, and (c) ice clouds from Pv6.0 dataset.

Figure 3.7 provides timeseries plots of normalized anomalies for cloud fractions across different cloud phases and net CREs, along with scatter plots depicting the relationships between these anomalies. To account for strong seasonal variations in cloud fractions and CREs, anomalies are calculated by subtracting the respective monthly mean values. Since cloud fractions and CREs have different units, a normalization process is applied to the timeseries plots by subtracting the mean anomaly value and dividing by the standard deviation. The mean and standard deviation are derived separately for cloud fraction and CRE anomalies to ensure consistency. This normalization allows for direct comparability between cloud fraction and CRE anomalies, facilitating a more meaningful analysis of their variations and correlations.

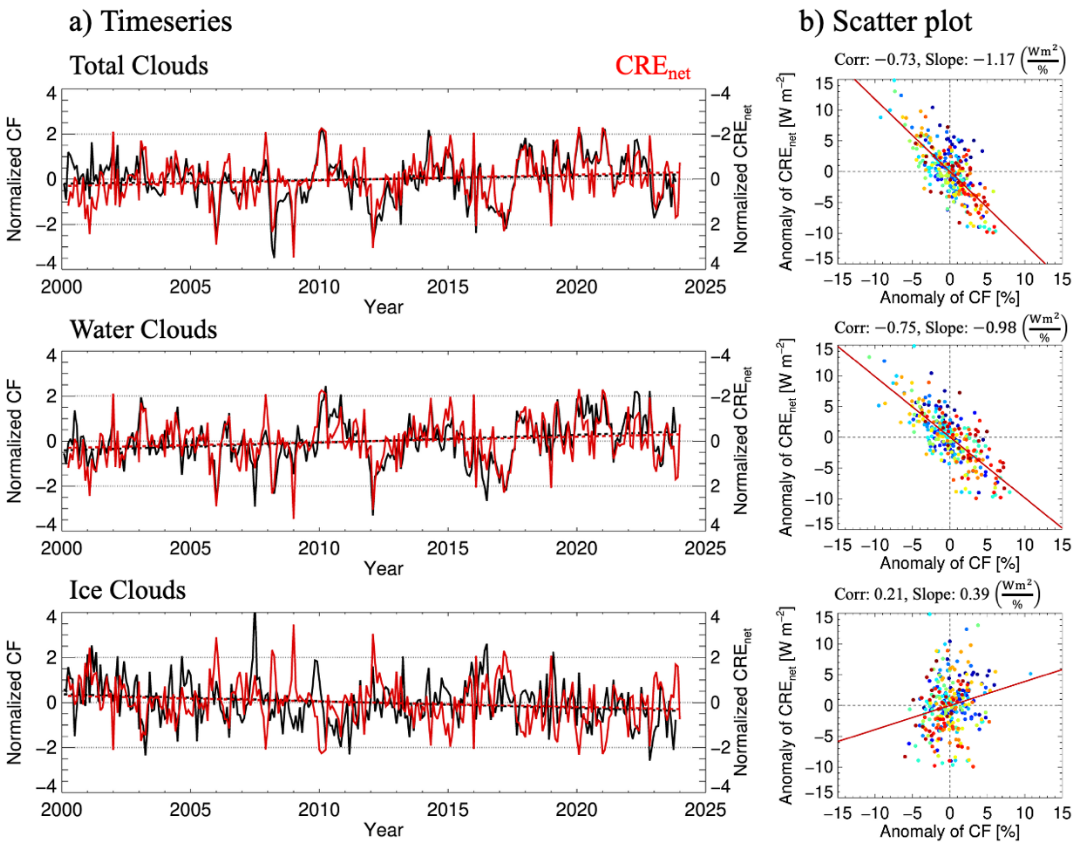

Figure 3.7: (a) timeseries plot of normalized cloud fraction (black) from Pv6.0 dataset and net CRE from CERES EBAF dataset and (b) scatter plots between anomaly of cloud fraction and net CRE for different cloud phases (top: total clouds, middle: water clouds, and ice clouds).

Normalized anomalies of total cloud fractions show a strong inverse relationship with the normalized anomalies of CREs, indicating a negative correlation between cloud fractions and CREs. The correlation coefficient between total cloud fractions anomalies and CRE anomalies is −0.74, with a slope of −1.18 Wm^2 per %. Similarly, water cloud fractions show an even stronger negative correlation with CREs, with a correlation coefficient of −0.76 and a slope of −0.99 Wm^2 per %. Both total (+0.97% per decade) and water (+1.63% per decade) cloud fractions have increased over the study area since 2000. In contrast, ice cloud fractions show a weak positive correlation with CREs (correlation coefficient: 0.23, slope: 0.42 Wm^2 per %), contributing the warming effect of ice clouds. These results indicate that the strengthening of the cooling effects of CREs over the study area is primarily driven by the increases in cloud fractions, particularly water clouds.

Figure 3.8 shows the timeseries of mean cloud fraction over the study area for different cloud phases since 2000. Total cloud fraction ranges from 60 to 85%, with an increasing trend of 0.97% per decade. It exhibits show strong seasonality, with higher cloud fractions observed from August to October and lower cloud fractions from January to March. Similarly, water clouds also show pronounced seasonality, also ranging from 60 to 85% with a mean increase of 1.63% per decade. In contrast, ice clouds show relatively weak seasonality, ranging from 10 to 25%, and show a decreasing trend at a rate of 0.70% per decade.

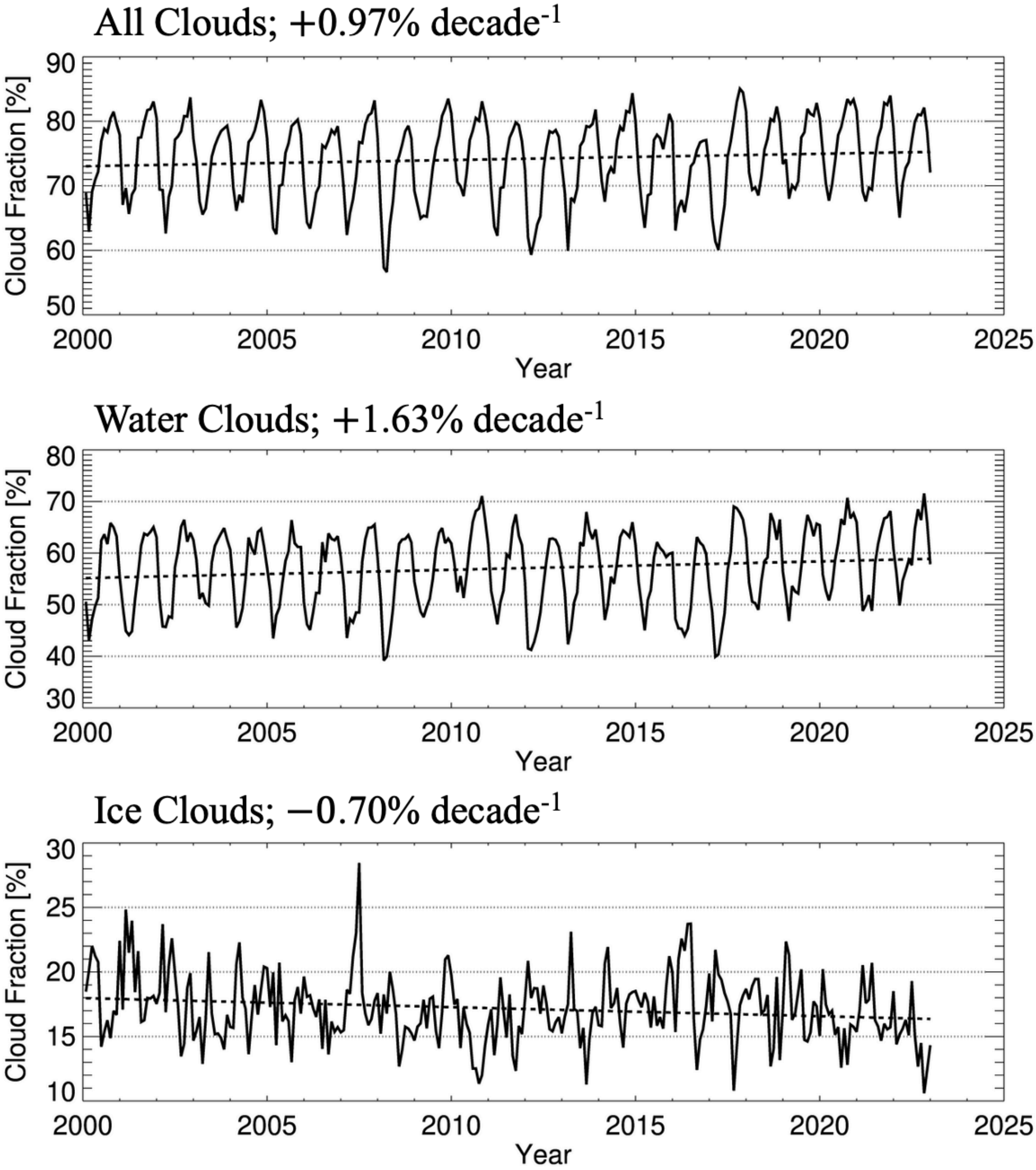

Fig. 3.8 Timeseries of mean cloud fraction over the study area for different cloud phases (total clouds: top, water clouds: middle, and ice clouds: bottom).

Figure 3.9 shows the timeseries of mean shortwave, longwave, and net CREs over the study area since 2000. The mean shortwave CRE ranges from −30 to −80 Wm^2, following seasonality of total and water cloud fractions. High cloud fractions, particularly the large proportion of water clouds, contribute to strong cooling effects of CREs over the study area. The cooling effect has strengthened at a rate of −1.45 Wm^2 per decade. The mean longwave CRE ranges from 11 to 20 Wm^2 and shows weak seasonality. The warming effects of clouds has weakened at a rate of −0.46 Wm^2 per decade. The net CRE, which is the sum of shortwave and longwave, ranges from −20 to −60 Wm^2, with a significant decreasing trend of −1.91 Wm^2 per decade.

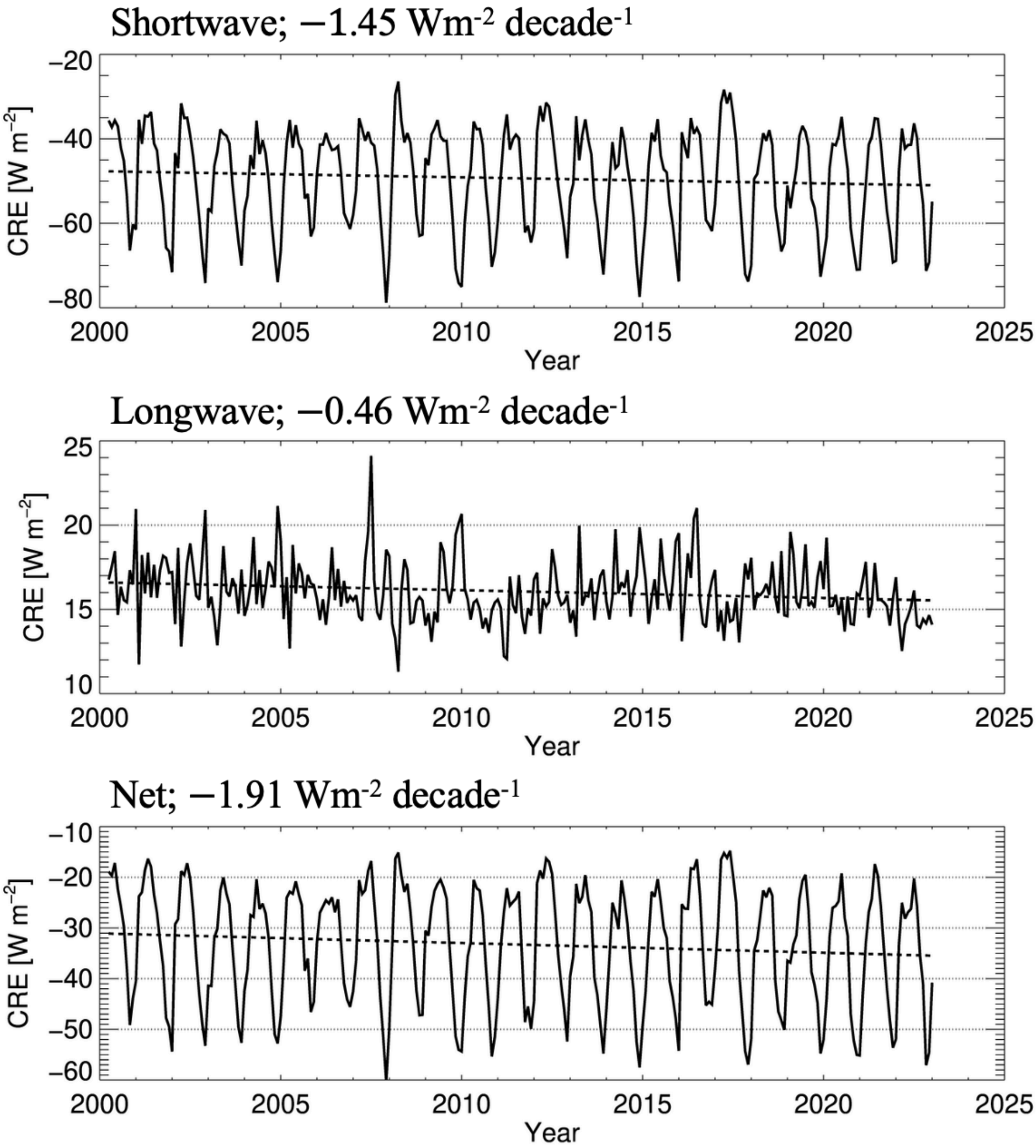

Fig. 3.9 Timeseries of CREs from CERES EBAF over the study area (shortwave: top, longwave: middle, and net: bottom).

Chapter 4

Can we identify physical processes contributing to regional changes in clouds?

4.1 Introduction

The CCFs framework is widely used in many studies to better understand the mechanisms behind cloud formation and to investigate the atmospheric factors that drive variations in clouds characteristics (Grise and Tselioudis, 2024; Naud et al., 2023; Jian et al., 2021; Klein et al., 2018; Kawai et al., 2017). This framework helps identify key processes, such as temperature, moisture, and other atmospheric variables that influence cloud development and behavior. For example, surface temperature, a well-known CCF, plays a crucial role in cloud formation by influencing evaporation and moisture supply, convective uplift, and atmospheric stability (Ramanathan and Collins, 1991). Another important CCF with a strong positive correlation to maritime low cloud fractions is the estimated inversion strength (EIS; Wood and Bretherton, 2006), which is used to characterize the strength of the inversion at the top of the boundary layer (Naud et al., 2023). In this chapter, we investigate the role of CCFs in influencing cloud fractions over the southeastern Pacific Ocean using satellite observations and reanalysis datasets and identify the main drivers of changes in clouds. This work has been submitted as part of Seo et al. (2025c).

4.2 Cloud Controlling Factors

In this research, we use 14 CCFs, including surface temperature, humidity, heat flux, atmospheric stability, and vertical/horizontal wind velocities, that have been widely used in previous CCFs framework studies. These variables are used to comprehensively evaluate the atmospheric conditions influencing cloud formation in both water and ice phases. For the analysis of the 14 meteorological CCFs, we use the ERA5 reanalysis dataset, produced by the ECMWF, at a monthly resolution. Table 4.1 provides a list of the CCFs along with their physical explanations, highlighting the key atmospheric processes that influence cloud formation.

Table 4.1. Cloud controlling factors used in this study, physical explanations connecting them to cloud formation, and key studies supporting them.

Cloud Controlling Factors	Physical Explanations	Key Studies
Surface temperature (T_{sfc})	Warmer surfaces enhance convection and increase atmospheric instability, while cooler surfaces support formation of low-level stratus clouds.	Klein et al., 2018; Zelinka and Hartmann, 2011; Bony et al., 1997
Temperature advection (T_{adv})	Warm air advections increase instability and enhance lift. Cold advections suppress deep convection and generate low clouds in moist convection.	Grise et al., 2021; Klein, 1997
Estimated inversion strength (EIS)	Strength of EIS in the boundary layer inhibits convection and favors extensive stratocumulus clouds over ocean regions.	Wood and Bretherton, 2006; Andersen et al., 2022
Wind speed at 10m (WS_{10m})	Surface wind speeds influence surface moisture fluxes and impact the depth of MBL.	Scott et al., 2020; Boutle et al., 2010
Surface sensible heat flux (SSHF)	Characterized the energy exchange between the ocean and the atmosphere. Low sensible heat fluxes maintain stable stratocumulus layers, favoring the occurrence of low-level clouds.	Naud et al., 2023; Boutle et al., 2010
Total column water vapor (TCWV)	High TCWV increases the likelihood tha the air will reach its saturation point, and it is associated with the development of thicker and more extensive clouds.	Henken et al., 2015
Upper tropospheric stability (UTS)	UTS controls the vertical motion of air at high altitude so that it is robustly correlated with upper-level clouds such as tropical anvil cloud formation.	Kemsley et al., 2024; Saint-Lu et al., 2022; Bony et al., 2016

Upper-tropospheric wind shear between surface and 300 hPa ($UTWS_{300hPa}$)	Affect the structure of convective storms and mesoscale convective systems, enhancing cloud-top turbulence and causing clouds to spread and stretch horizontally through the advection of air at different levels and speeds.	Kemsley et al., 2024; Anber et al., 2014; Jensen et al., 2011; Lin and Mapes, 2004
Relative humidity at 300, 500, and 700 hPa (RH_{300hPa}, RH_{500hPa}, and RH_{700hPa})	Upper-tropospheric relative humidity is associated with large-scale distribution of tropical deep clouds and lower free-tropospheric relative humidity regulates the mean height of convective outflow.	Kemsley et al., 2024; Sherwood et al., 2004; Sherwood et al., 1999; Bony et al., 1997
Vertical velocity at 300, 500, and 700 hPa (w_{300hPa}, w_{500hPa}, and w_{700hPa})	Indicates regions of air rise and descent. Enhanced upward motion encourages the development of high and thick clouds.	Ge et al., 2021; Grise et al., 2021; Klein et al., 2018

4.3 Multilinear regression fit

To model the multilinear relationship between the CCFs and cloud fractions, we apply the ridge regression technique (Ceppi and Nowack, 2021). This method is particularly effective in addressing common issues in multilinear regression models, such as multicollinearity and overfitting. Ridge regression is especially suitable for this analysis, given the high degree of correlation among the CCFs, as it helps stabilize coefficient estimates and enhances the model's ability to generalize to observations. Due to the varying ranges and different units of the CCFs, all variables are normalized using their mean and standard deviation values to ensure consistency and comparability. The models are computed for each grid box with a resolution of $1° \times 1°$.

4.3.1 Experiment for model performance

Figure 4.1 represents the R-squared values of individual CCFs for water clouds, which quantify how well the model replicates observed cloud fractions by measuring the proportion of total variation in observations explained by the regression model. The R-squared value is calculated using the following equation:

$$\text{R-squared} = 1 - \frac{\sum_i (y_i - \hat{y}_i)^2}{\sum_i (y_i - \bar{y})^2}$$

where y_i represents cloud fractions from satellite-based observations, $\bar{y}$ is the mean cloud fraction, and $\hat{y}_i$ denotes the cloud fraction estimated by the model. An R-squared value of 1 indicates a perfect fit, meaning the model fully explains the observed variations. For water clouds, EIS shows the highest R-squared values, followed by humidity such as relative humidity and total precipitable water vapor. Surface temperature and wind speed also show relatively high R-squared values. Dynamical and surface flux factors are less consistently explanatory on their own, but still contribute within the full model. Overall, the R-squared values from all CCFs are high over most ocean regions, except for some part of the Southern Ocean.

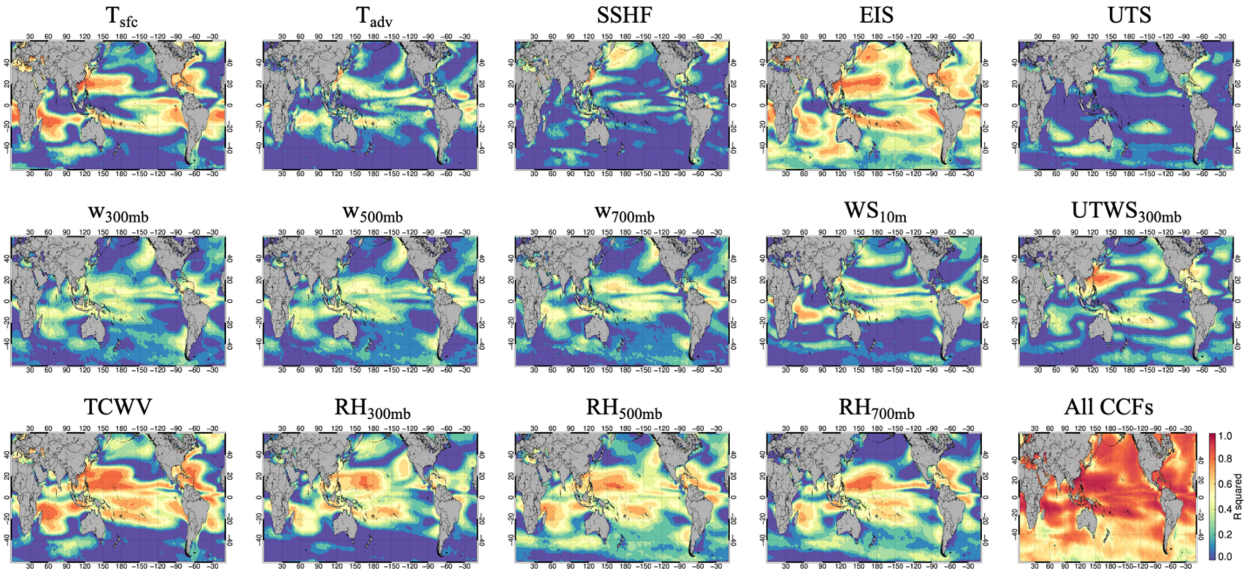

Figure 4.1: Map of R-squared values of individual CCFs from 1981 to 2023 for water cloud phases.

Figure 4.2 shows R-squared values of individual CCFs for ice clouds using multilinear regression model from 1981 to 2023. The R-squared values for ice clouds from all CCFs are also high over most ocean area except for the Southern Ocean. The results indicate that upper-tropospheric humidity, total column water vapor, and vertical motion show the strongest relationships with ice cloud variability, especially over tropical deep convective regions such as the western Pacific and Indian Ocean. The spatial patterns of R-squared values for vertical velocity and relative humidity are similar so that an additional experiment is conducted in Appendix C. In contrast, SSHF and surface wind speed show weak correlations across most regions, suggesting limited direct influence on high cloud processes.

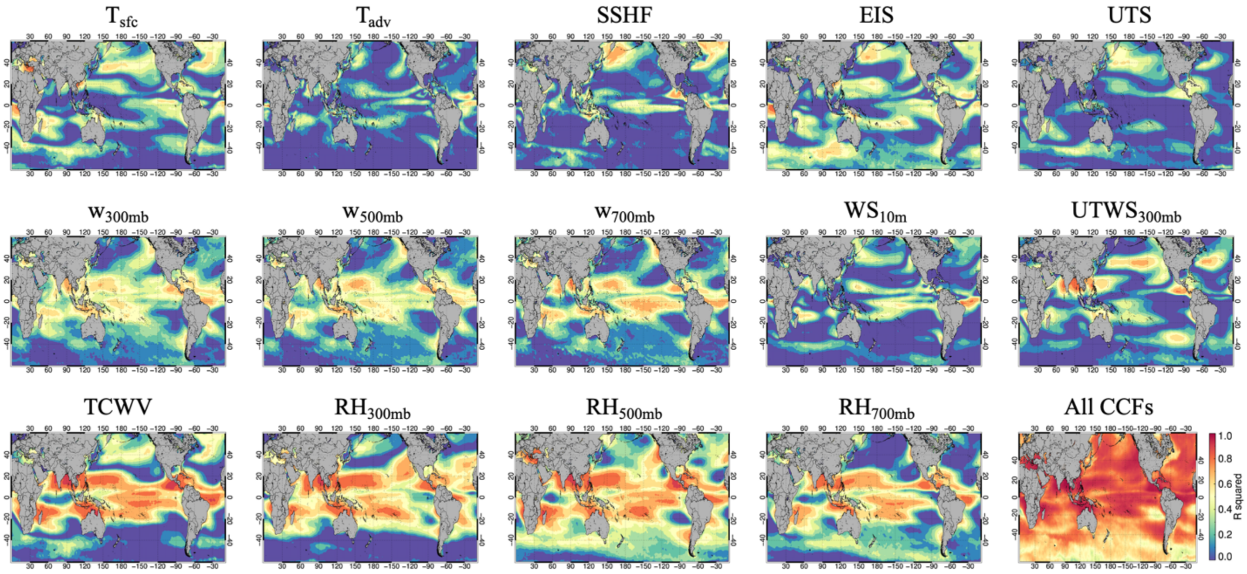

Figure 4.2: Map of R-squared values for individual CCFs from 1981 to 2023 for ice cloud phases.

To assess the feasibility of simulating cloud fractions using a multilinear regression model, we trained the model with cloud fraction data from Pv6.0 and corresponding CCFs from 1981 to 2010 to determine the regression coefficients. These coefficients were then applied to CCFs from 2011 to 2023 to estimate cloud fractions. Figure 4.3 shows R-squared and RMSE values from 2011 to 2023, obtained using the multilinear regression model trained from 1981 to 2010. For total clouds, the model performs well across most regions, especially within the study area, except for a small section along the west coast of South America. For water clouds, the model demonstrates strong predictive capability, as indicated by consistently high R-squared values across all regions. In the cast of ice clouds, R-squared values remain high overall, except for a small central area within the study region where ice cloud fractions are very low. These results suggest that the multilinear regression model using CCFs is particularly effective in capturing variations in specific cloud types. Globally, R-squared values are high across most of regions, except for the midlatitude Southern Ocean for all cloud phases, with a particularly notable decrease for total clouds. This is due to consistently high cloud fractions exceeding 90%. As a result, the low variation in the denominator of the R-squared equation leads to relatively lower model predictions compared to the other regions.

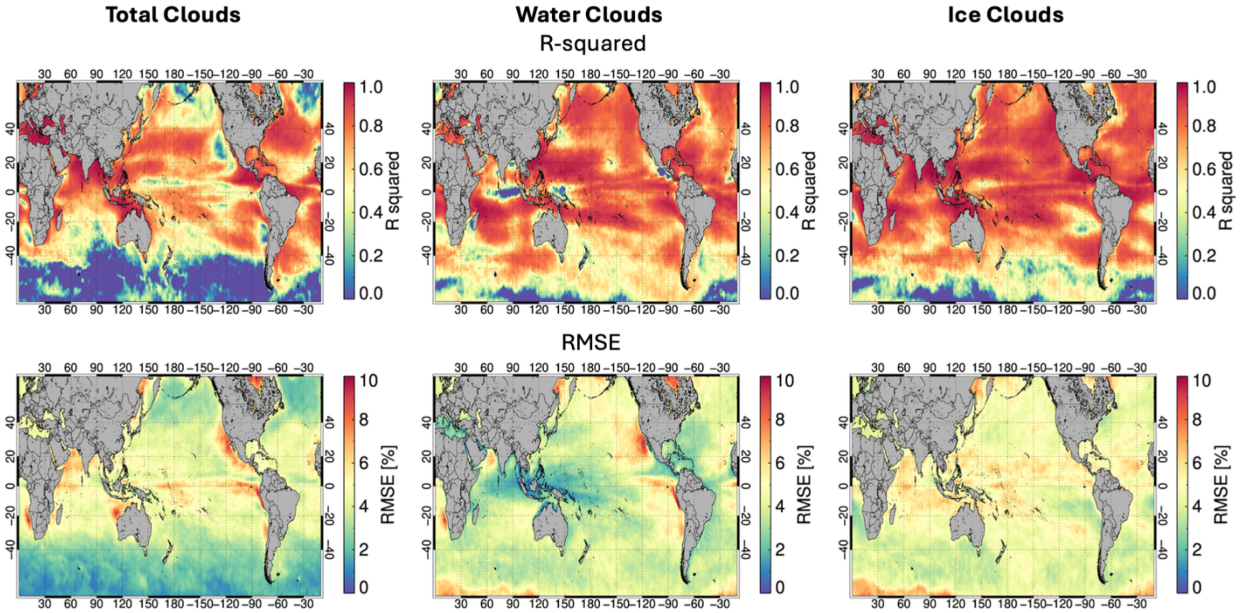

Figure 4.3: Map of R-squared values (top) and RMES (bottom) of cloud fraction between Pv6.0 dataset and multilinear regression model from 2011 to 2023 for different cloud phases (left: total clouds, middle: water clouds, and right: ice clouds).

Figure 4.3 also shows RMSE values for total, water, and ice clouds. The RMSE of total clouds is high along the west coast of North America, where water clouds dominate, and in the ITCZ region, where convective high clouds are prevalent, reaching 10%. In these regions, R-squared values are also lower than in other areas. Additionally, the RMSE is lower over the Southern Ocean, despite the R-squared values are low. Across the study area, the RMSE of total clouds is approximately 5%, which is significantly lower than the RMSE between Pv6.0 and climate models, as shown in

Appendix A. The mean RMSE of water clouds over the study area is also around 5%, while the mean RMSE of ice clouds is below 4%. This suggests strong performance in estimating cloud fractions using CCFs and a multilinear regression model compared to observations.

Figure 4.4 shows the mean cloud fractions from Pv6.0 and the multilinear regression model. The mean cloud fractions for total, water, and ice clouds estimated by multilinear regression model using CCFs closely resemble the observed values.

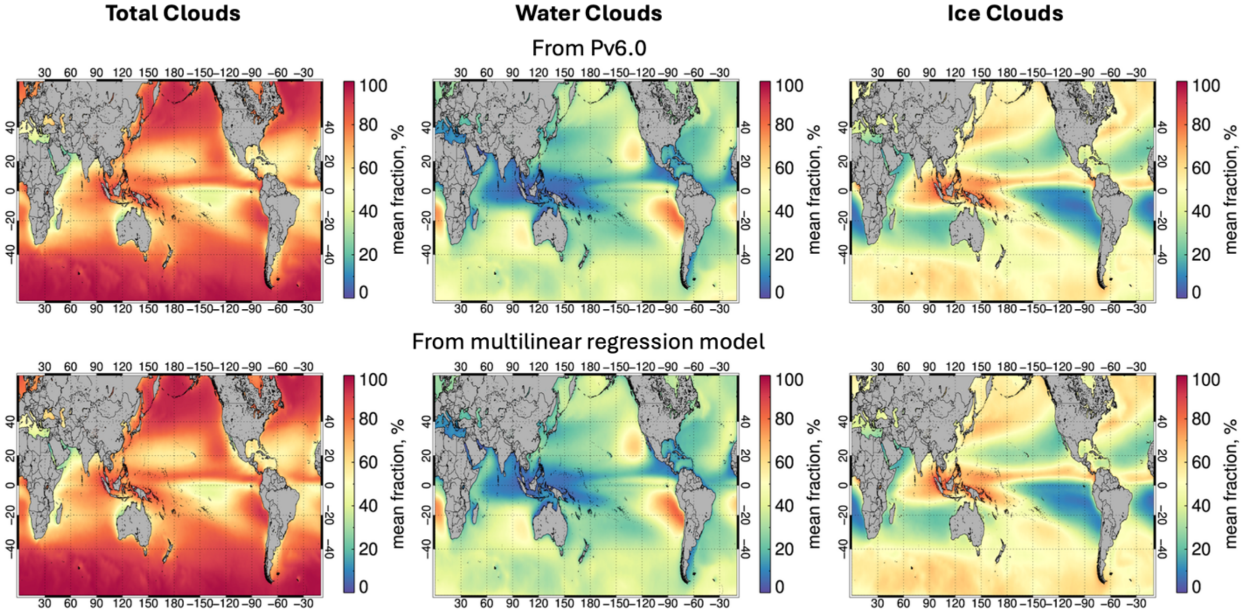
Total Clouds

Water Clouds

Ice Clouds

From Pv6.0

From multilinear regression model

Figure 4.4: Map of mean cloud fractions from Pv6.0 dataset (top) and multilinear regression model (bottom) from 2011 to 2023 for different cloud phases (left: total clouds, middle: water clouds, and right: ice clouds).

Figure 4.5a and 4.5b show the trends in cloud fractions from 2011 to 2023 based on Pv6.0 and model estimates. During this period, total cloud fractions increased, with a maximum observed rate of 5.7% per decade. The model also indicates an increasing trend in total cloud fractions over the study area, though the affected region is smaller, and the rate is lower at 3.5% per decade. Water cloud fractions from the model show better agreement with observations than total clouds, although the observed magnitudes remain higher. Observations indicate a maximum increase in water cloud fractions of 7.3 % per decade, while the model estimates a slightly lower rate of 4.8% per decade. Conversely, ice cloud fractions exhibit a decreasing trend, with maximum rates of −6.2 % per decade in observations and −4.3% per decade in model estimates. Overall, the model successfully captures the spatial patterns of cloud fraction trends, particularly for water and ice clouds, though it underestimates their magnitude compared to observations. While the model performs well when trained on the first three decades of data, it is ultimately trained using the full observational dataset for this study.

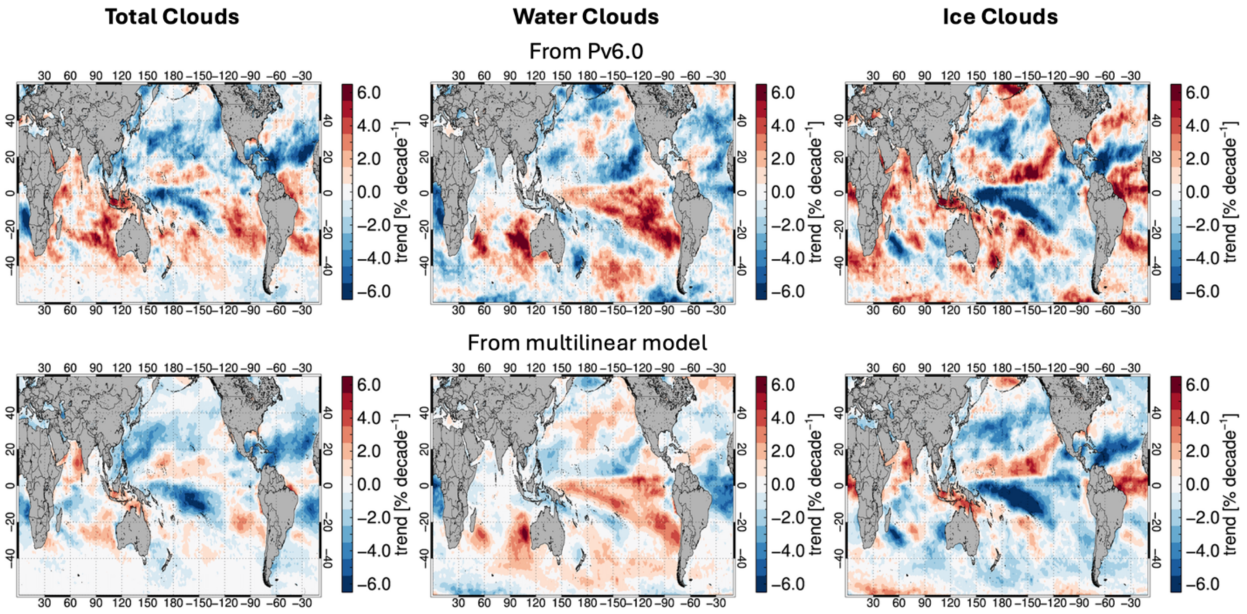

Figure 4.5: Map of trend in cloud fractions from Pv6.0 dataset (top) and multilinear regression model (bottom) from 2011 to 2023 for different cloud phases (left: total clouds, middle: water clouds, and right: ice clouds).

4.3.2 Model estimates

Figure 4.6 shows the mean cloud fractions from Pv6.0 and the multilinear regression model from 1981 to 2023. As shown in Figure 4.4, the mean cloud fractions for total, water, and ice clouds estimated by multilinear regression model using CCFs closely resemble those from Pv6.0 and show greater similarity to observations compared to climate models.

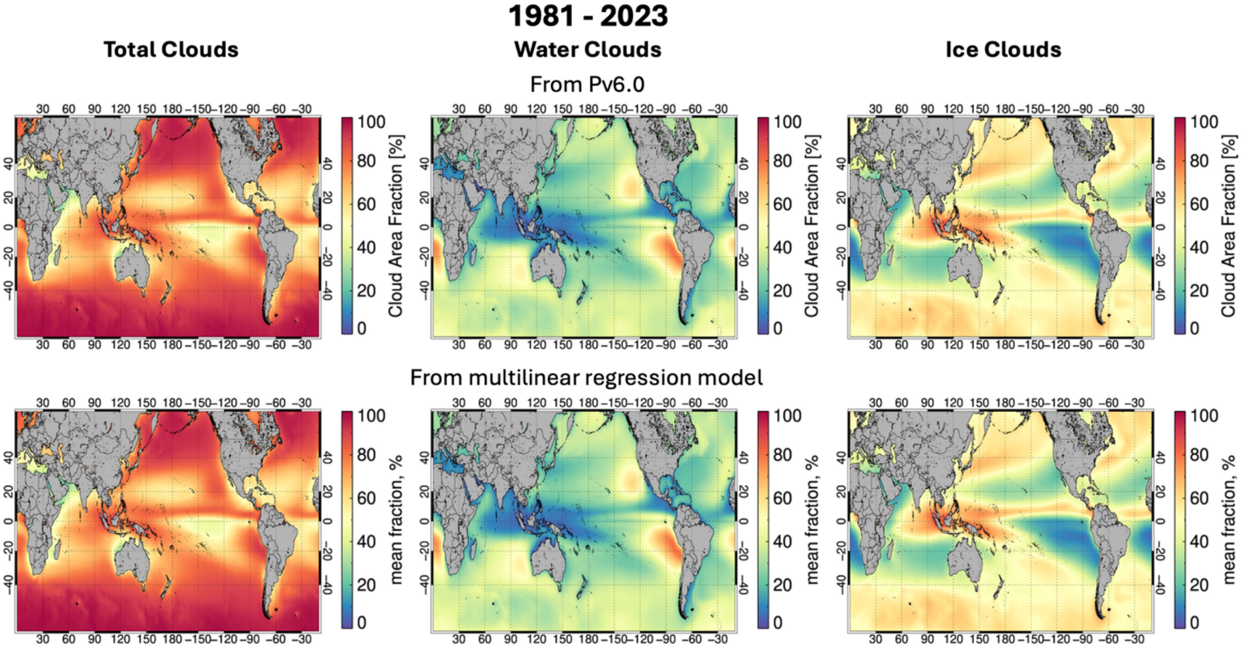

Figure 4.6: Map of mean cloud fractions from Pv6.0 dataset (top) and multilinear regression model (bottom) from 1981 to 2023 for different cloud phases (left: total clouds, middle: water clouds, and right: ice clouds).

Figure 4.7 shows the R-squared values and RMSE between Pv6.0 and the multilinear regression model from 1981 to 2023. Similar to the R-squared values in Figure 4.3, the model performs well across most regions, except for the Southern Ocean, although it performs better than in the period from 2011 to 2023. Water and ice clouds also show high R-squared values globally including in the Southern Ocean. The RMSE between Pv6.0 and the multilinear regression model also shows similarity in the period from 2011 to 2023. Most RMSE values for cloud fractions are below 5%, except in contain areas such as the ITCZ region and west coast of North America for total clouds and water clouds, and near the equator for ice clouds.

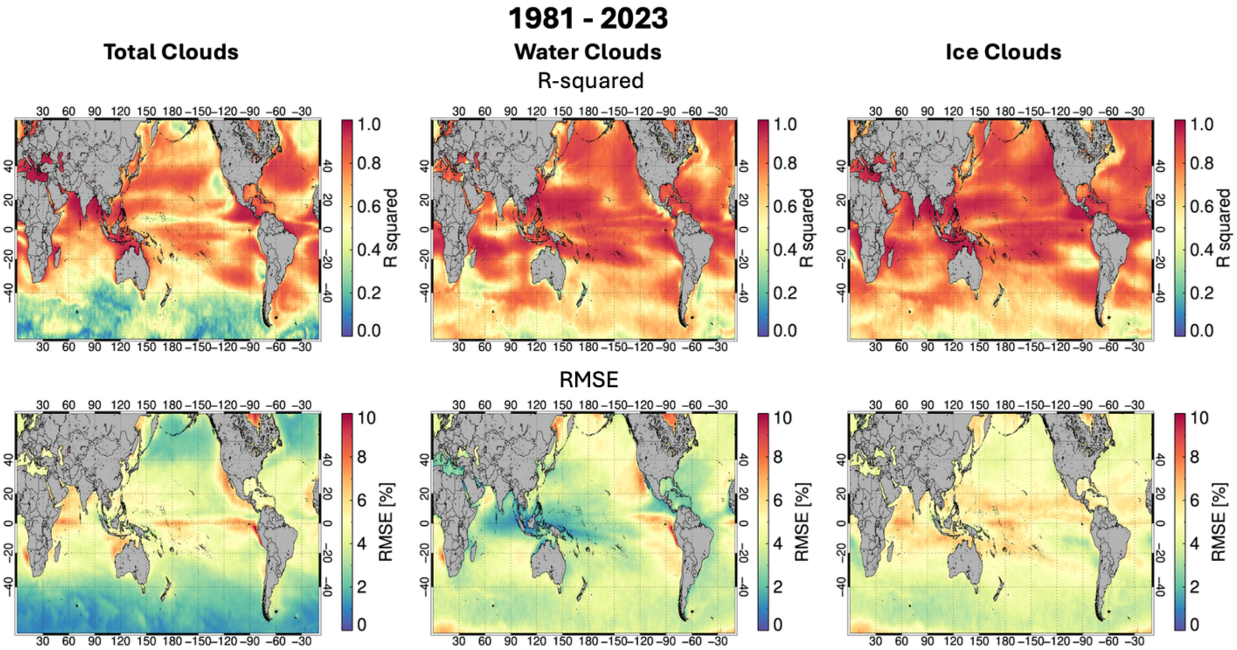

Figure 4.7: Map of R-squared values (top) and RMES (bottom) of cloud fraction between Pv6.0 dataset and multilinear regression model from 1981 to 2023 for different cloud phases (left: total clouds, middle: water clouds, and right: ice clouds).

Figure 4.8 shows maps of trends in total, water, and ice cloud fractions from Pv6.0 and model estimates from 1981 to 2023. For total clouds, model estimates show a trend pattern similar to observations, although the magnitudes are lower. They indicate a significant decreasing trend over the central Pacific Ocean and global declines, except for the southeastern Pacific Ocean and

Southeast Aisa. Trends in total clouds from model estimates over the midlatitudes remain close to 0%. For water clouds, both Pv6.0 and model estimates show increasing trends over the southeastern Pacific Ocean and midlatitude, while decreasing trends are observed over the ITCZ, western Pacific Ocean, and subtropical subsidence regions. Lastly, increases in ice cloud fractions from both Pv6.0 and model estimates are observed over the ITCZ and western Pacific Ocean, while decreases are seen in other regions, with the most notable decline over the central Pacific.

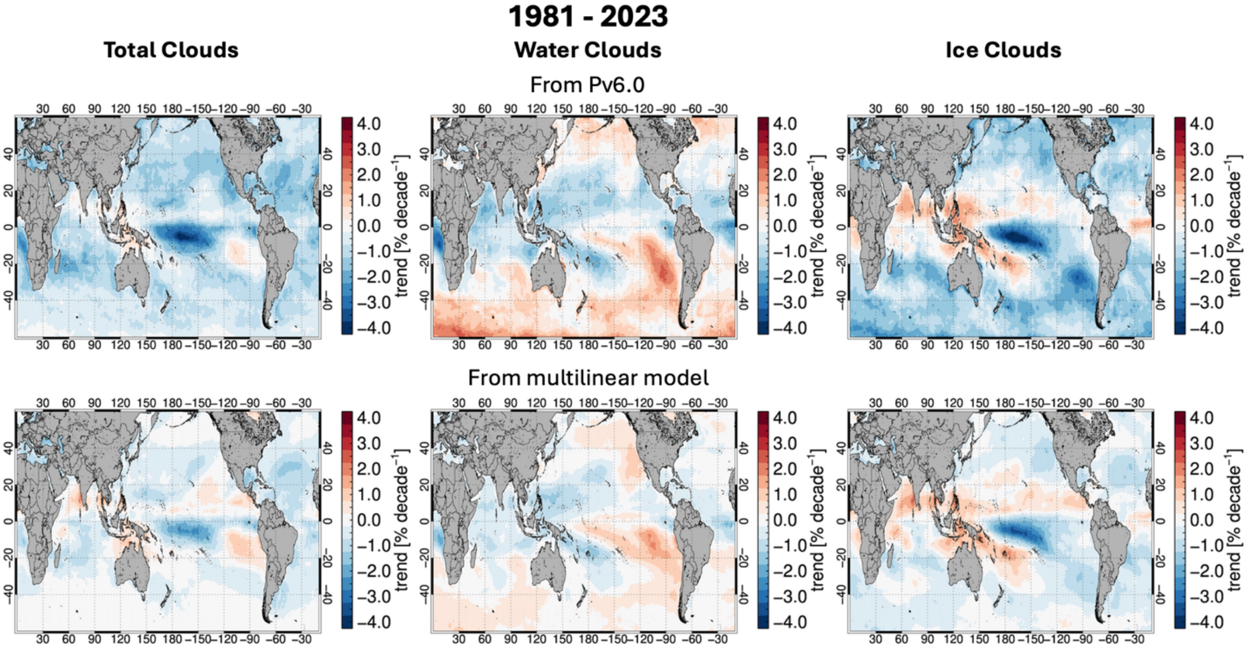

Figure 4.8: Map of trend in cloud fractions from Pv6.0 dataset (top) and multilinear regression model (bottom) from 1981 to 2023 for different cloud phases (left: total clouds, middle: water clouds, and right: ice clouds).

To connect with the changes in CREs, Figure 4.9-4.11 show the mean, R-squared, RMSE, and trends of cloud fractions estimated by the multilinear regression model and CCFs over the study area from 2000 to 2023. Figure 4.9 presents the mean cloud fractions from Pv6.0 and model estimates. As shown in Figure 4.6, the mean cloud fractions for total, water, and ice clouds estimated by the multilinear regression model using CCFs closely resemble those from Pv6.0. The regions that experience a strengthening of cooling effects, as shown in Figure 3.6, are dominated by water clouds.

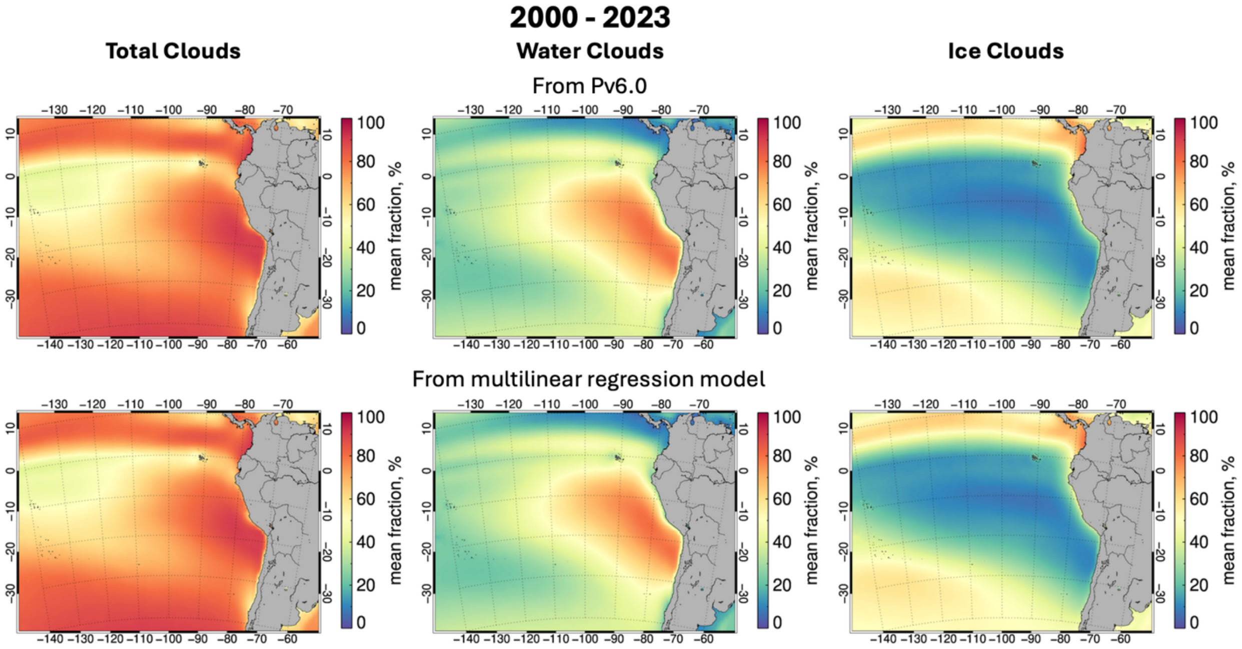

Figure 4.9: Map of mean cloud fractions from Pv6.0 dataset (top) and multilinear regression model (bottom) over study area from 2000 to 2023 for different cloud phases (left: total clouds, middle: water clouds, and right: ice clouds).

Figure 4.10 shows the R-squared and RMSE values between Pv6.0 and model estimates from 2000 to 2023. For total clouds, the R-squared values remain high across most regions, except for a small area along the west coast of South America, where the values are comparatively lower. The RMSE is generally below than 10%, although higher RMSE values are observed over the ITCZ. In regions dominated by water clouds, the RMSE is relatively low, ranging from 4% to 5%. For water clouds, the R-squared values exceed 0.6 across all regions and approach 1 in most areas, indicating a strong correlation. However, high RMSE values are observed over the ITCZ, similar to total clouds, while RMSE values along the west coast of South America remain below 6%. For ice clouds, most regions show high R-squared values, close to 1, except for some areas where water clouds dominate. Model estimates for ice clouds show good agreement with observations, with RMSE values generally lower than 6%.

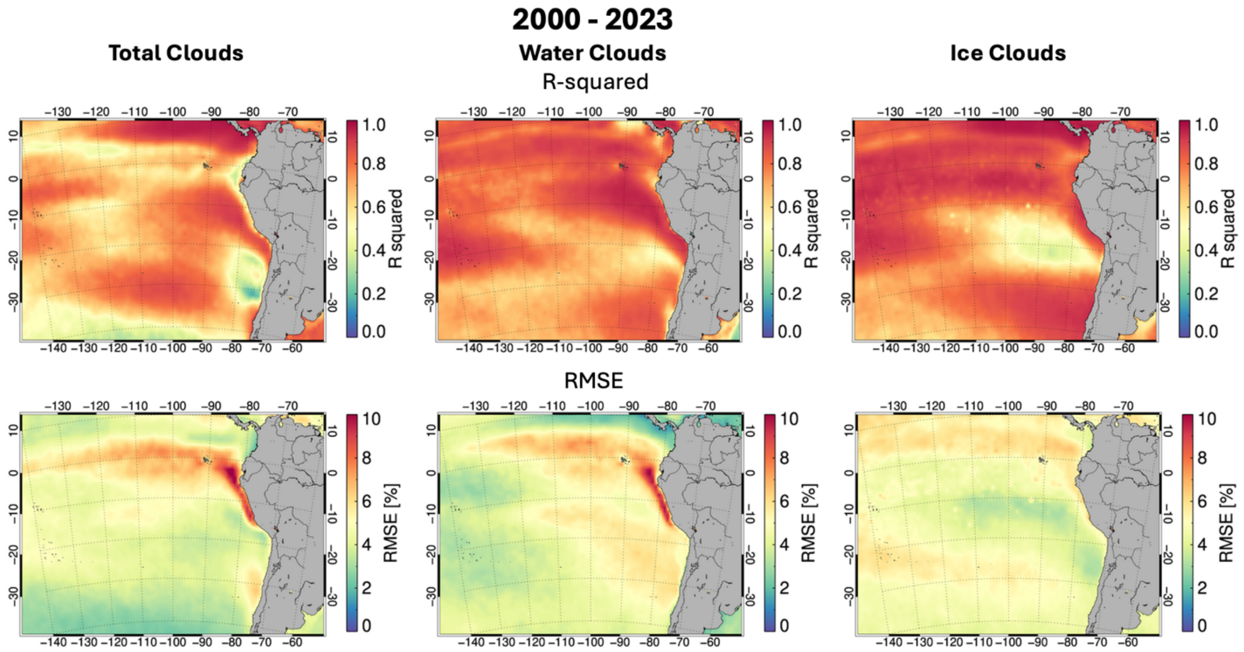

Figure 4.10: Map of R-squared values (top) and RMES (bottom) of cloud fraction between Pv6.0 dataset and multilinear regression model over study area from 1981 to 2023 for different cloud phases (left: total clouds, middle: water clouds, and right: ice clouds).

Figure 4.11 shows trends in cloud fractions over the study area from Pv6.0 and model estimates. Both trends show similar patterns of increases, particularly where water clouds dominate along the west coast of South America. For water clouds, Pv6.0 and model estimates show significant increases over this region, except for the ITCZ, with spatial patterns align with the strengthening of cooling effects in CREs. For ice clouds, most area show a decrease in cloud fractions, while an increase is observed over the ITCZ. Overall, the multilinear regression models using CCFs capture the spatial patterns and magnitudes of trends in cloud fractions well compared to observations.

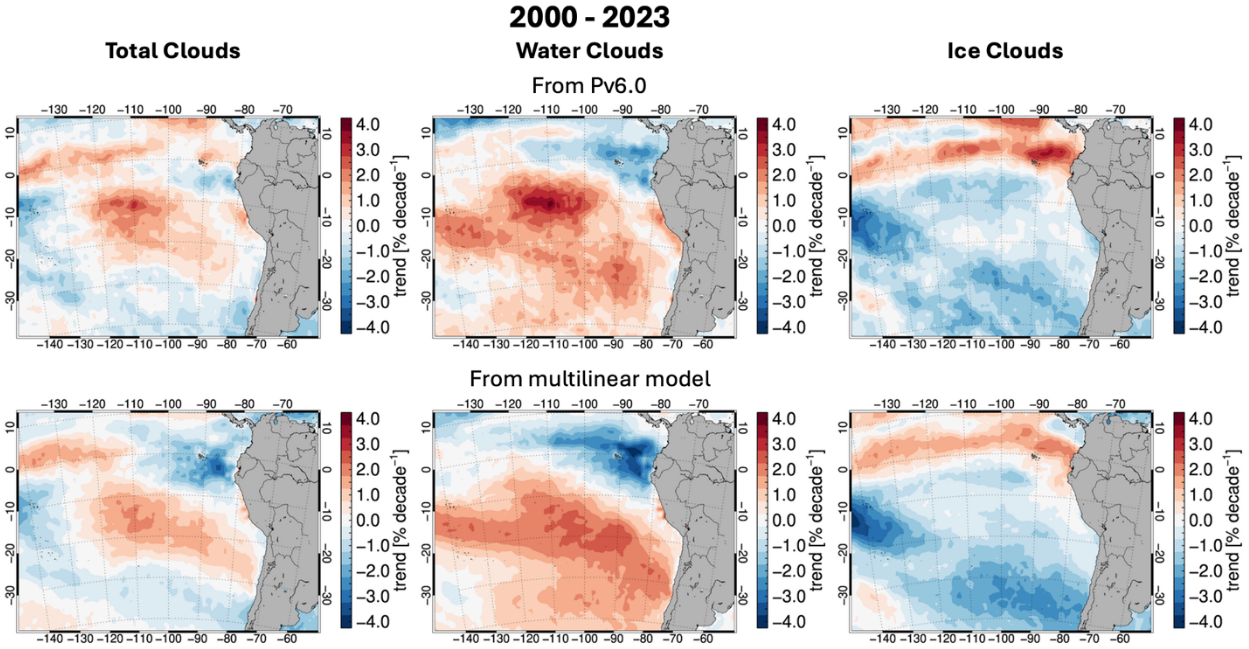

Figure 4.11: Map of trend in cloud fractions from Pv6.0 dataset (top) and multilinear regression model (bottom) over study area from 1981 to 2023 for different cloud phases (left: total clouds, middle: water clouds, and right: ice clouds).

4.3.3 Impacts of individual cloud controlling factors

Using the coefficients from the multilinear regression models and variations in CCFs, the contributions of individual CCFs to trends in cloud fractions over the study area can be quantified, as shown in Figure 4.12. Given the dominance of maritime stratocumulus clouds in this region, key drivers of low clouds such as EIS, surface temperature, wind speed at 10m, surface temperature advection, and relative humidity at 700 hPa play significant roles in shaping changes in total cloud fractions. For ice clouds, surface temperature and relative humidity at 700 hPa contribute to increasing ice cloud fractions, whereas EIS, TCWV, and relative humidity at 300 hPa are linked to decreases in ice cloud fractions. Among these factors, EIS has the strongest influence on in water cloud fraction increases, reaching a maximum of 1.6% per decade. This finding contrasts with Andersen et al. (2022), that reported a decline in low cloud cover over the Northeastern Pacific. Other CCFs have relatively weaker effects on changes in water cloud fractions.

a) Total Clouds

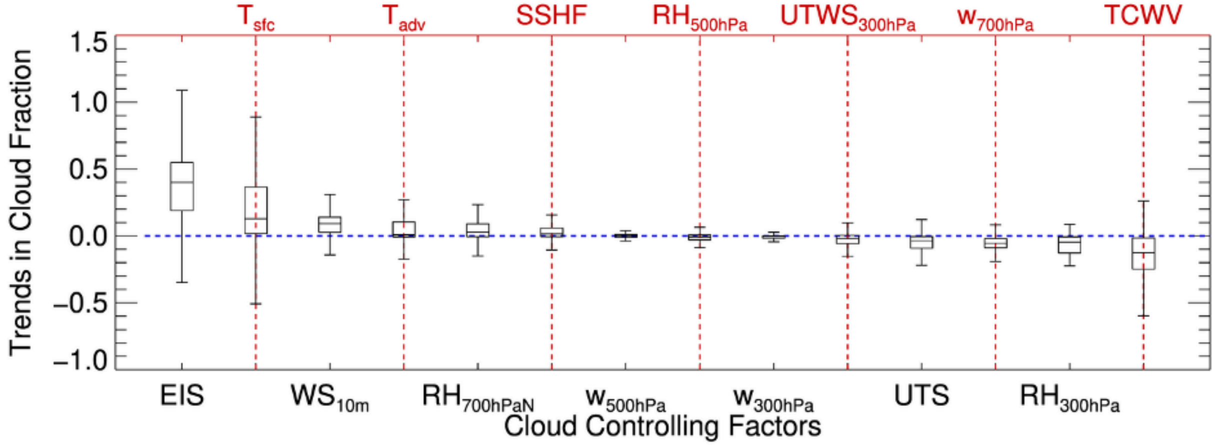

b) Water Clouds

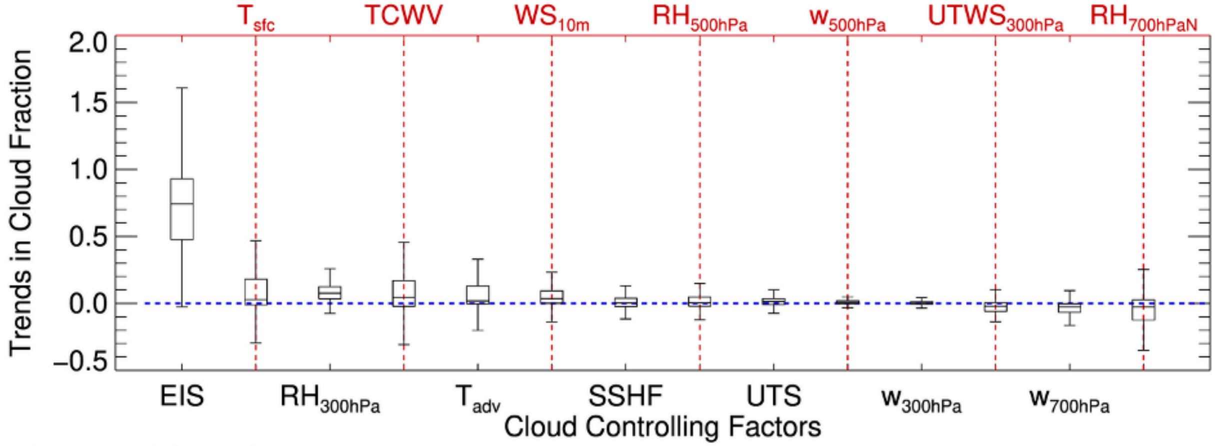

c) Ice Clouds

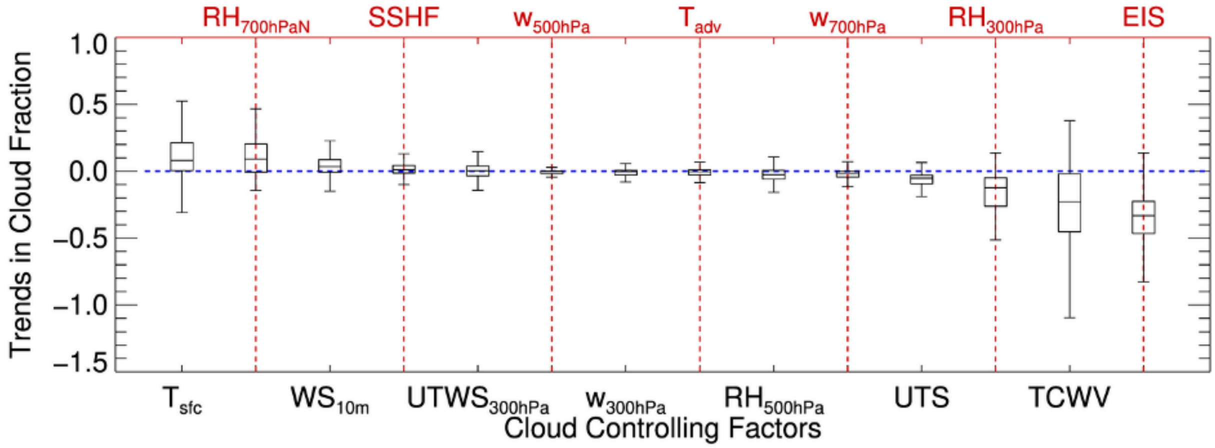

Figure 4.12. Box plot showing the contributions of individual CCFs to trends in clouds over the study area from 1981 to 2023 for different cloud types: (a) total clouds, (b) water clouds, and (c) ice clouds.

4.4 Estimated Inversion Strength

The EIS, as described by Wood and Bretherton (2006), is a measure of the stability of the lower atmosphere. It takes into account the vertical temperature gradient, which is another key component in determining atmospheric stability, in addition to the lower troposphere stability (LTS; Slingo 1987; Klein 1997). EIS can be calculated using the following equation:

$$EIS = LTS - \Gamma_m^{850}(z_{700} - z_{LCL})$$

where the LTS is the difference in potential temperature between 700 hPa and the surface, Γ_m^{850} is the moist adiabatic lapse rate at 850 hPa, and z_{700} and z_{LCL} are the height of the 700 hPa level and the lifting condensation level relative to the surface, respectively. A higher EIS value corresponds to a stronger inversion, resulting in reduced entrainment of dry air from the free troposphere, which prevents cloud breakup and contributes to a larger fraction of low cloud fractions.

4.3.1 relationship with cloud fractions

Figure 4.13 shows timeseries and scatter plots of anomalies in mean water cloud fractions from Pv6.0, model estimates, and mean EIS from ERA5 over the study area. Due to differences in units, the anomalies are normalized by subtracting the mean value and dividing by the standard deviation. The trend in water cloud fractions from Pv6.0 is 1.22 % per decade, while the trend from the model is 0.96% per decade. EIS has increase at a rate of 0.28 K per decade. Variations in water cloud fractions and EIS are strongly correlated from 1981 to 2023. The correlation coefficient between the anomaly in water cloud fractions from Pv6.0 and EIS is 0.73, with a slope of 3.66 % per K. The correlation coefficient between the anomaly in water cloud fractions from the model and EIS is higher, at 0.88, with a same slope of 3.66 % per K when compared to those from the observations. These slopes are lower than 6 ± 1% per K derived by Wood and Bretherton (2006), that calculated the slope using the National Centers for Environmental Prediction-National Center for Atmospheric Research (NCEP−NCAR) reanalysis dataset (Kistler et al., 2001). Other studies also report a slightly lower slope in the relationship between low cloud fractions and EIS, with values generally less than 6 % per K (Cutler et al., 2022; Wang et al., 2023; Kawai et al., 2017).

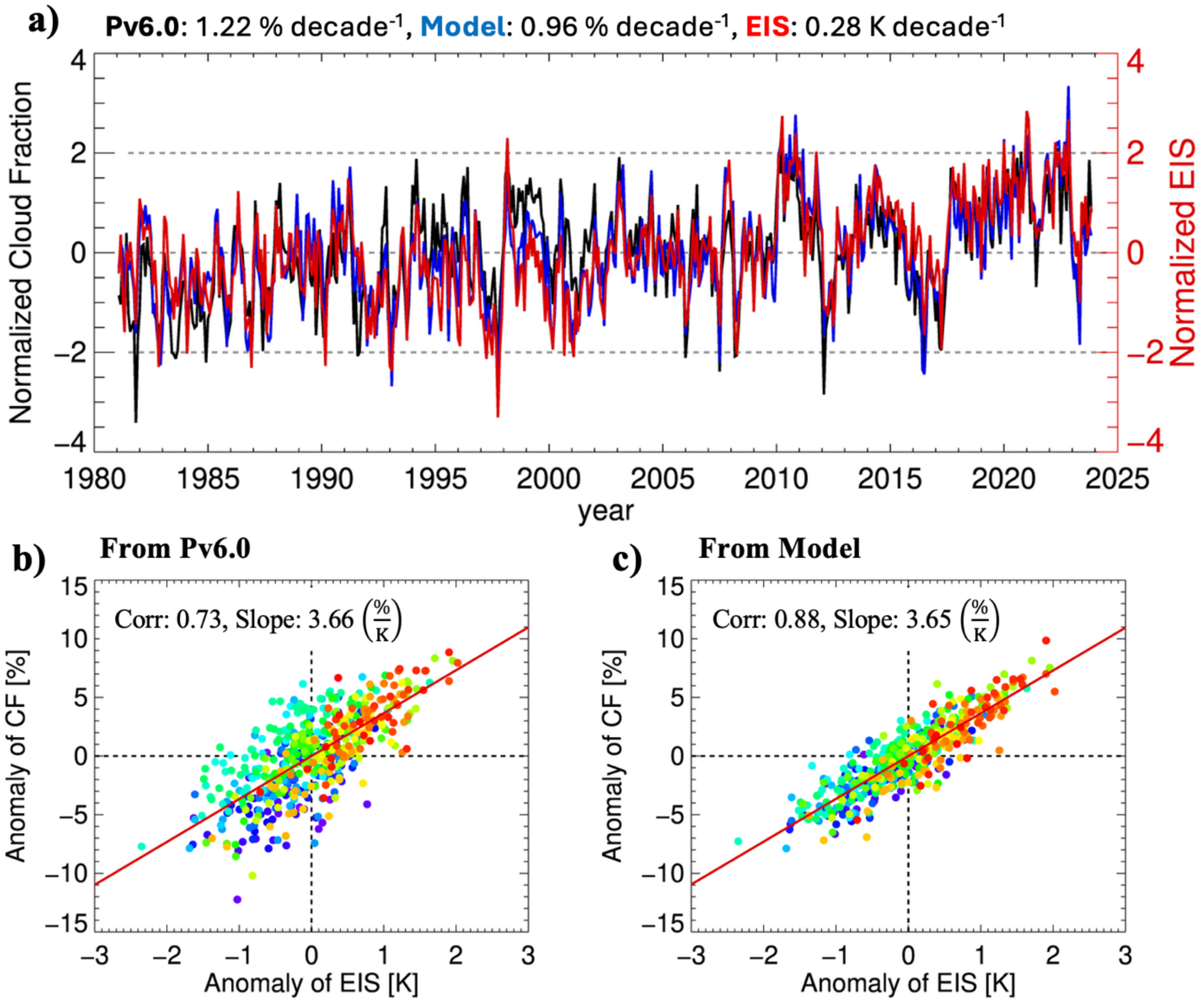

Figure 4.13. a. Timeseries of normalized anomaly of water cloud fraction and EIS over the study area from 1981 to 2023. b. Scatter plot of anomaly of water cloud fraction from Pv6.0 and EIS. c. Scatter plot of anomaly of water cloud fraction from model and EIS. Colors in scatter plot represent the date (blue: 1981 to red: 2023).

4.3.2 Timeseries plots

Figure 4.14a presents the timeseries of the mean EIS and its components used to calculate EIS over the study area. The mean EIS ranges from 2.6 to 9.1 K and shows a positive trend of 0.30 K per decade. The mean LTS ranges from 16.4 to 22.2 K and shows a similar positive trend of 0.31 K per decade, aligning with trend observed in EIS. The second term in the EIS equation ranges from 12.6 to 14.3 K, with a negligible trend of 0.01 K per decade. This indicates that changes in EIS are primarily driven by increases in LTS. The timeseries of the mean LTS and potential temperature at the surface and 700 hPa is shown in Figure 4.14b. The potential temperature at the surface ranges from 289 to 296 K. and shows a decreasing trend of 0.10 K per decade. In contrast, the potential temperature at 700 hPa ranges from 309 to 315 K and shows an increasing trend of 0.21 K per decade. Therefore, the strengthening of lower tropospheric stability over study area is primarily driven by the combined effects of a decrease in surface temperature and an increase in temperature at 700 hPa.

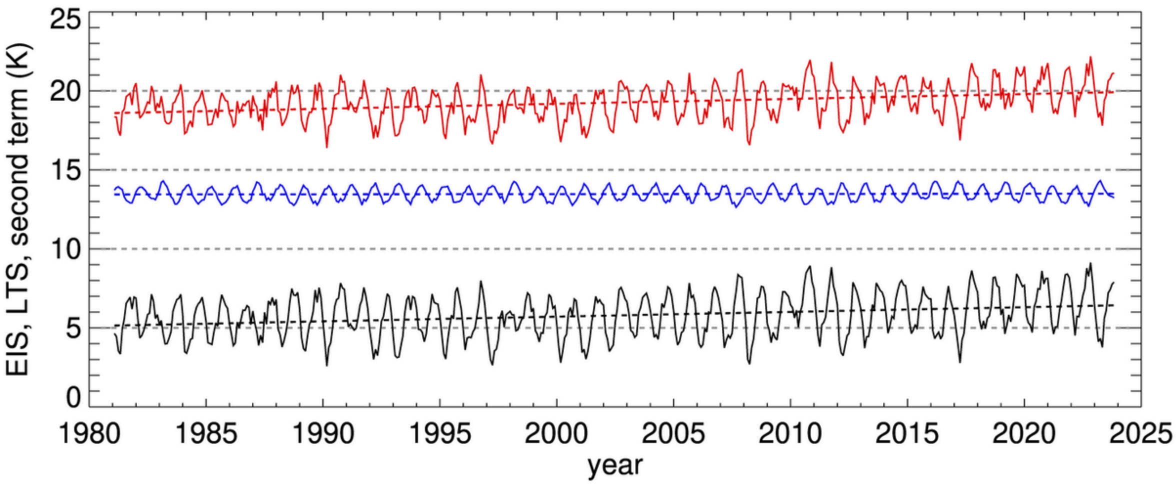

a) EIS: 0.30 K decade^{-1}, **LTS**: 0.31 K decade^{-1}, **Second term**: 0.01 K decade^{-1}

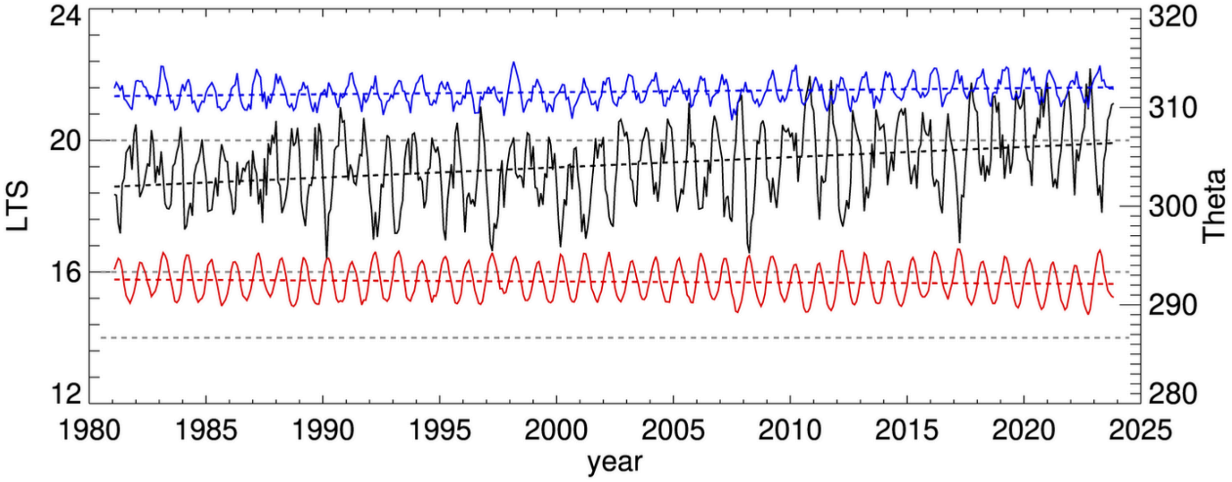

b) LTS: 0.31 K decade^{-1}, **Theta$_{sfc}$**: −0.10 K decade^{-1}, **Theta$_{700\ hPa}$**: 0.21 K decade^{-1}

Figure 4.14. a. Timeseries of mean EIS, LTS, and second term over the study area from 1981 to 2023. b. Timeseries of mean LTS and potential temperature at the surface and 700 hPa from 1981 to 2023.

4.3.3 Map plots

Figure 4.15 shows map plots of the mean and trends of EIS and its components from 1981 to 2023. EIS ranges from 0 to 12, with spatial patterns closely resembling those of water cloud fractions. Higher EIS values are associated with higher water cloud fractions. Over the past four decades, EIS has increased at a maximum rate of 0.44 K per decade. LTS, ranging from 14 to 24, show similar spatial patterns and trends as EIS, with a maximum increase of 0.47 K per decade. The second term of EIS varies with latitude and shows no significant trend. Thus, the increase in EIS is primarily driven by the rise in LTS. LTS is defined as the difference between the potential temperature at 700 hPa and the surface. The potential temperature at the surface ranges from 280 to 300 K and has decreased as a maximum rate of 0.20 K per decade. In contrast, the potential temperature at 700 hPa, ranging from 300 to 315 K, has increased at a maximum rate of 0.35 K per decade. As a result, changes in EIS are driven by the combination of decreasing surface temperature and increasing atmospheric temperature at 700 hPa. This decreasing trend of surface temperatures are also observed from the extended-reconstructed (ERSST) and Hadley Center (HadISST) sea surface temperature dataset from 1979 to 2006 (Falvey and Garreaud, 2009). Among the several large-scale modes of natural variability including the ENSO, the Pacific decadal oscillation, and the southern annular mode, which are known to strongly influence temperatures in this region, the influence of ENSO on these temperature changes is investigated in Appendix B.

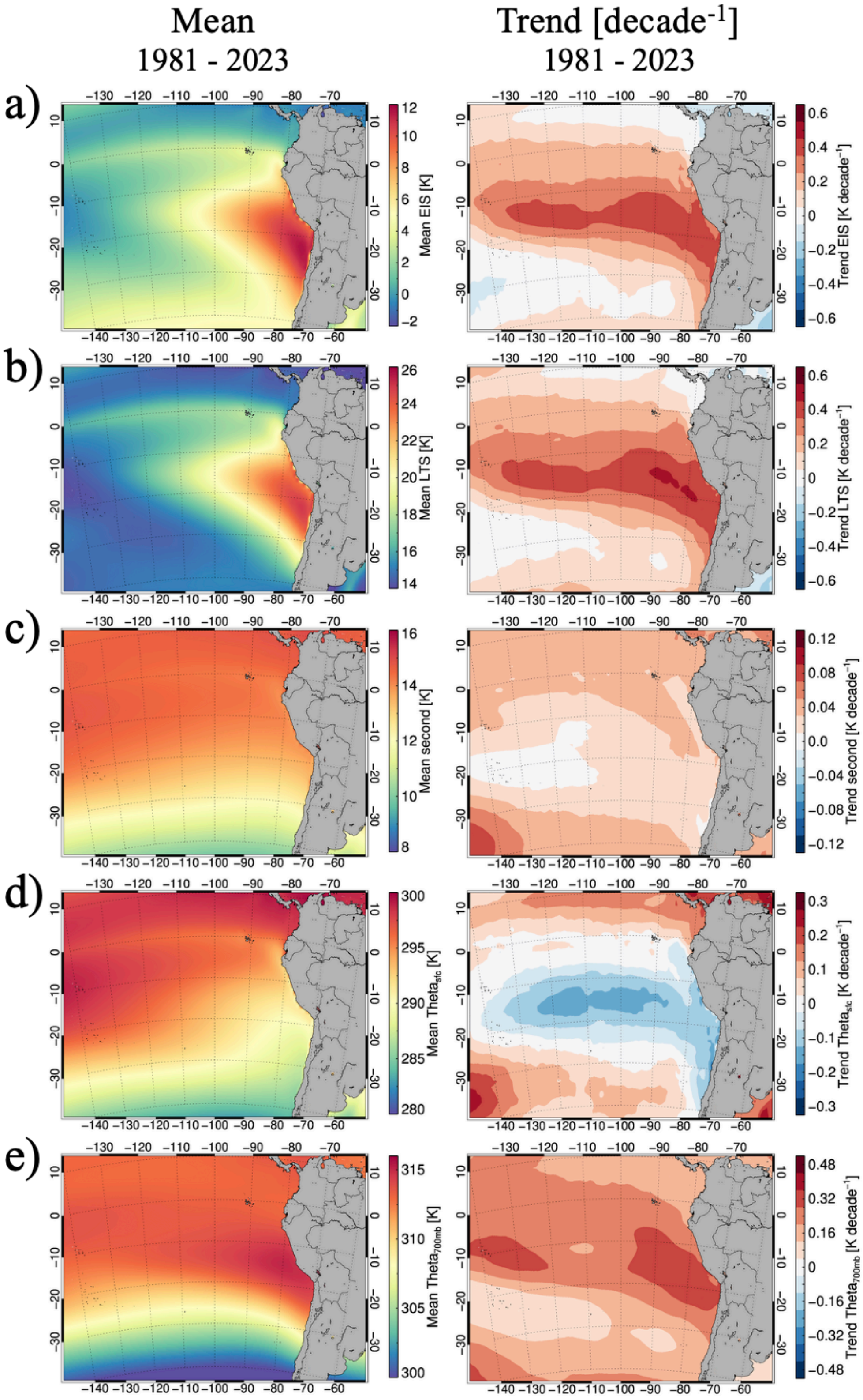

Figure 4.15: Map of mean (left) variables (a: EIS, b: LTS, c: $\Gamma_m^{850}(z_{700} - z_{LCL})$, d: θ_{sfc} and e: θ_{700hPa}) and trend (right) in variables from ERA5 reanalysis dataset from 1981 to 2023.

Chapter 5

Summary

Clouds play a critical role in regulating the Earth's radiative balance through their radiative characteristics, known as cloud radiative effects (CREs). These effects include heat exchange between the atmosphere and the surface via absorption and emission, as well as the regulation of solar energy through reflection and scattering (Arking, 1991; Chen et al., 2000). Recent studies indicate that the observed reduction in planetary albedo is primarily driven by a decline in global cloud fractions (Tselioudis et al. (2024), Weaver et al. (2024), Loeb et al., (2024)). However, certain regions have exhibited an increase in albedo, which enhances the reflection of solar radiation and mitigates surface warming. One prominent example is the southeastern Pacific Ocean, where enhanced cloud cover has contributed to higher albedo (Karlsson et al., 2023). Therefore, gaining a more comprehensive understanding of the physical processes that drive cloud formation in this region is essential for improving the accuracy of climate model predictions, especially in the context of the ongoing global warming crisis.

In this dissertation, several satellite-based observations (PATMOS-x, CLARA-A3, and CERES EBAF), reanalysis datasets (MERRA-2 and ERA-5), and climate models (14 CMIP6 AMIP climate simulations) are used to analyze changes in cloud properties and CREs and investigate physical processes over the southeastern Pacific Ocean.

This dissertation has thoroughly investigated the changes in cloud properties including fraction, top temperature, and optical thickness since 1981 and their influence on changes in CREs since 2000 and find physical processes driving these changes using multilinear regression methods and 14 CCFs. In this final chapter, we summarize the key findings in relation to the research questions introduced in Chapter 1. Additionally, we propose directions for future research on this topic.

5.1 Revisiting Research Questions

1. Have clouds changed significantly over the tropical and subtropical ocean since 1981 using PATMOS-x v6.0? (Focus area for Chapter 2)

In this chapter, PATMOS-x version 6.0 dataset is used to investigate long-term changes in cloud properties, including fractions, top properties, and optical thickness, over the ocean from 60°S to 60°N along with other satellite-based dataset (CLARA-A3 and CERES EBAF) and two reanalysis datasets (ERA-5 and MERRA-2). Monthly mean cloudiness is calculated using generalized additive model backfitting and observational weighting to consider orbital drifts of satellites and different local overpass times between satellites using Pv6.0 level2b dataset. The results show that mean cloud fraction is decreasing by 0.86% per decade, with maximums over the central Pacific Ocean near the equator at 3% per decade and midlatitudes. Over the southeastern Pacific Ocean, the west coast of South America, and the midlatitudes, it shows increasing trends in water clouds. Water clouds are decreasing over the western Pacific Ocean and the subtropical ocean. Ice clouds are decreasing over most ocean areas, except over the western Pacific Ocean. Changes in cloud fractions associated with cloud phase are connected to changes in cloud top heights. Cloud top heights increase over western Pacific Ocean at 0.4 km per decade. Decreases in cloud top heights happen over the southeastern Pacific Ocean as well as at other regions where marine stratocumulus clouds are dominant. These changes in cloud fraction and cloud top assignments both contribute to cloud radiative effect so that changes in radiative transfer process and Earth's radiation budget should be investigated. Both AVHRR-based CDRs (PATMOS-x and CLARA-A3) show noticeable drops in mean cloud fractions beginning in 2000 and stabilizing in 2003. This decrease was not seen in the reanalyzes or CERES records, suggesting there may be an instrumental cause for this shift. It coincides roughly with the transition from the AVHRR/2 to AVHRR/3 instrument, as well as the introduction of the mid-morning orbit, though we have failed to identify a root cause. Further work is needed to better characterize this shift if we want to take full advantage of the 20 years of data provided by the AVHRR cloud records in the 80s and 90s.

2. Have changes in clouds influenced cloud radiative effects? (Focus area for Chapter 3)

Recent studies suggest that ongoing global warming is linked to a reduction in planetary albedo, primarily driven by a decline in global cloud fractions (Tselioudis et al. (2024), Weaver et al. (2024), Loeb et al., (2024)). However, certain regions, such as the southeastern Pacific Ocean, have shown an increase in albedo, which enhances the reflection of solar radiation and mitigates surface warming. This increases is driven by an increase in low cloud fractions, contributing to higher albedos (Karlsson et al., 2023). In this chapter, two satellite-based observations (PATMOS-x v6.0 and CERES EBAF) are used to analyze how changes in clouds influence variations in CREs over the southeastern Pacific Ocean (from 30°S to 10°S, and from 120°W to 70°W). The results show an increase in cloud fractions (0.97% per decade), particularly a rise in water clouds (1.63% per decade), which is strongly correlated with the strengthening of the cooling effects from clouds in this region. The mean cooling effect in the study area has strengthened at a rate of -1.45 Wm^2 per decade. The mean longwave CRE ranges from 11 to 20 Wm^2 and shows weak seasonality. The warming effects of clouds has weakened at a rate of -0.46 Wm^2 per decade. The net CRE ranges from -20 to -60 Wm^2, with a significant decreasing trend of -1.91 Wm^2 per decade.

3. Can we identify physical processes contributing to regional changes in clouds? (Focus area for Chapter 4)

To investigate the physical processes driving changes in clouds, the CCF framework is applied using the ridge regression method, a type of the multilinear regression technique, along with 14 CCFs from ERA5, including thermodynamic properties, wind speed, vertical velocity, and stability indices. The estimated cloud fractions derived from this framework show good agreement with satellite-based observations (Pv6.0). Specifically, the water cloud fractions from the CCF framework show a strong correlation with EIS, with a correlation coefficient of 0.88 and a slope of 3.66 % per K. The box plot showing individual impacts of CCFs suggest that the increase in water clouds is primarily driven by an increase in EIS (0.30 K per decade). The enhanced atmospheric stability is attributed to a combination of decreasing in surface temperature (−0.10 K per decade) and increasing atmospheric temperature at 700 hPa (0.21 K per decade) over the study area.

5.2 Future work

In the future, we plan to investigate the role of clouds in CRE changes, as well as the relationships between cloud fractions and CCFs in different cloud regimes that have shown significant changes over last four decade, including the central and western Pacific Ocean, as shown in Figure 2.3. Especially, the results in Appendix C suggests the importance of investigation of individual role and impacts of CCFs to the model performance. Cloud fractions derived from the CCF framework using the ridge regression technique show strong agreement with observations, as shown in Chapter 4. In contrast, as shown in Chapter 2, climate models show large differences in the mean and trends of cloud fractions, in addition to high variability among them. We will focus on regions with the largest variability between climate models and examine the feasibility of simulating cloud fractions using multilinear regression coefficients derived in this study, along with CCFs in climate models. Additionally, we will explore cloud sensitivity and feedback mechanisms based on these results.

Appendix A

Variability in climate simulations.

Net CRE is strongly influenced by cloud fraction and cloud properties such as temperature and thickness. Therefore, challenges in accurately simulating clouds contribute to the high variability in radiative effects across different climate models. To investigate, 14 Coupled Model Intercomparison Project Phase 6 (CMIP6; O'Neill et al., 2016; Eyring et al., 2016) AMIP climate simulations are used. Specifically, purpose of CMIP6 AMIP simulation is to isolate the atmospheric response to observed sea surface temperature and sea ice using atmosphere-only models including both natural and anthropogenic forcings such as greenhouse gases, aerosols, solar variability, volcanic eruptions, etc. Due the using atmospheric model only, it reduces uncertainty from ocean model biases. Therefore, CMIP6 AMIP climate simulations have been used widely for attribution studies and evaluation of atmospheric studies ().

Figure A1 shows maps of mean net CRE from 14 CMIP6 AMIP climate simulations for the period from 2000 to 2014. The strongest cooling effects of clouds are observed along the west coast of South America, driven by the prevalence of maritime stratocumulus clouds in this region. Additionally, the ITCZ exhibits highly negative net CRE due to the presence of strong convective clouds. However, the magnitude and spatial features differ between climate models and show low similarity with CERES EBAF. For example, GISS-E2-1-G and GISS-E2-2-G underestimate the cooling effects along the west coast of South America. IPSL-CM6A-LR and IPSL-CM6A-MR1 show different spatial pattens of cooling effects in the same region. Lastly, most climate simulations overestimate the cooling effects over the ITCZ region compared to CERES EBAF.

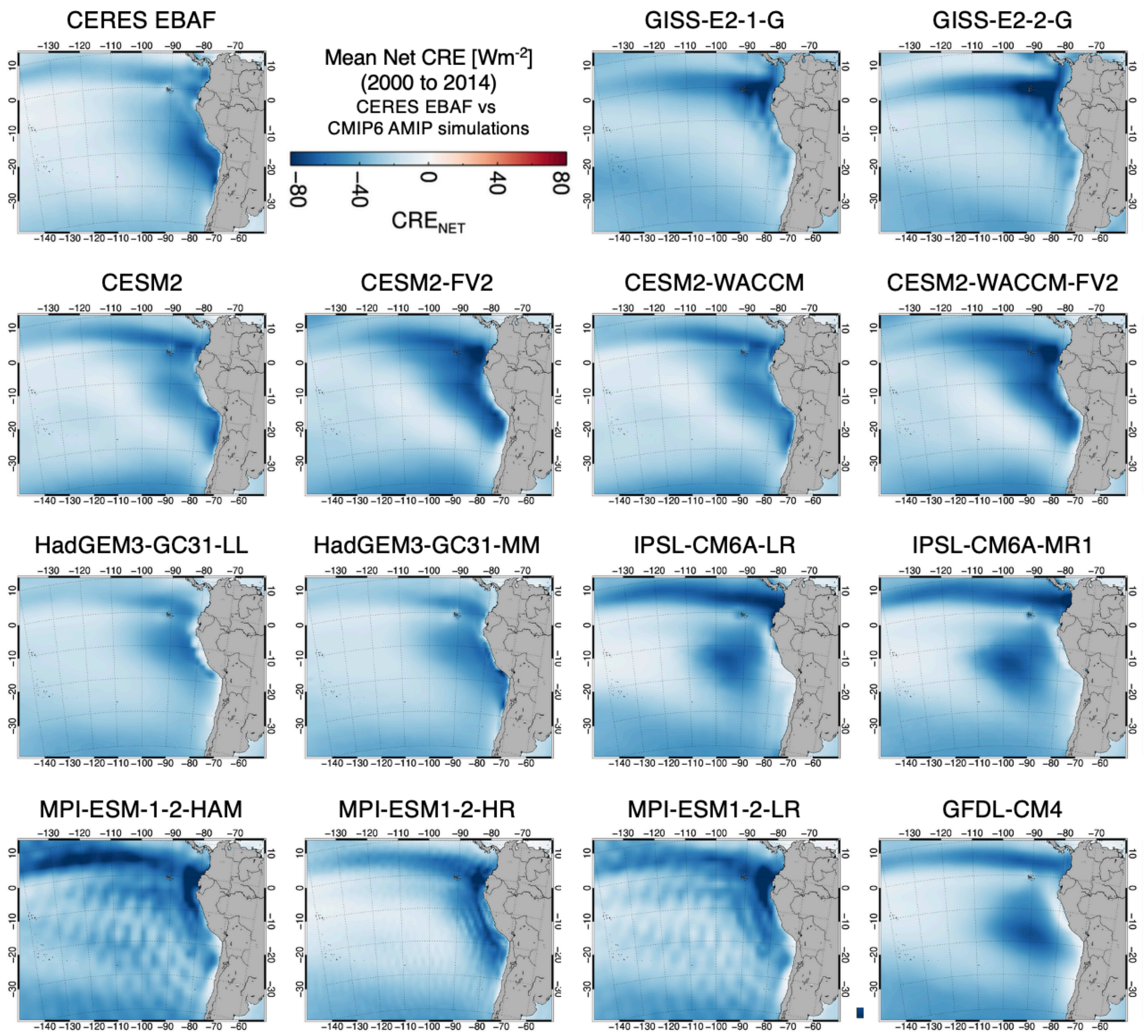

Figure A1: Map of mean net CRE (W·m^{-2}) from CERES EBAF dataset and CMIP6 AMIP climate simulations.

Figure A2 shows maps of root mean squared error (RMSE) of net CRE between CERES EBAF and CMIP6 AMIP climate simulations for the period from 2000 to 2014. The RMSE values between CERES EBAF and climate simulation are calculated using following equation:

$$RMSE = \sqrt{\frac{\sum_i^N \left(y_{ceres,i} - y_{model,i}\right)^2}{N}}$$

where y_{ceres} is net CRE from CERES EBAF and y_{model} is net CRE from climate simulation. All climate simulations show high RMSE values over the study area, with a maximum RMSE exceeding 50 Wm^{-2}. Specifically, CESM2-FV2, CESM2-WACCM-FV2, IPSL-CM6A-LR, IPSM-CM6A-MR1, and MPI-ESM-1-2-HAM show high RMSE values over the ITCZ regions. Most climate simulations, including IPSL-CM6A-LR, IPSL-CM6A-MR1, MPI-ESM1-2-LR, and GFDL-CM4, show high RMSE values over the southeastern Pacific Ocean along the coast of South America.

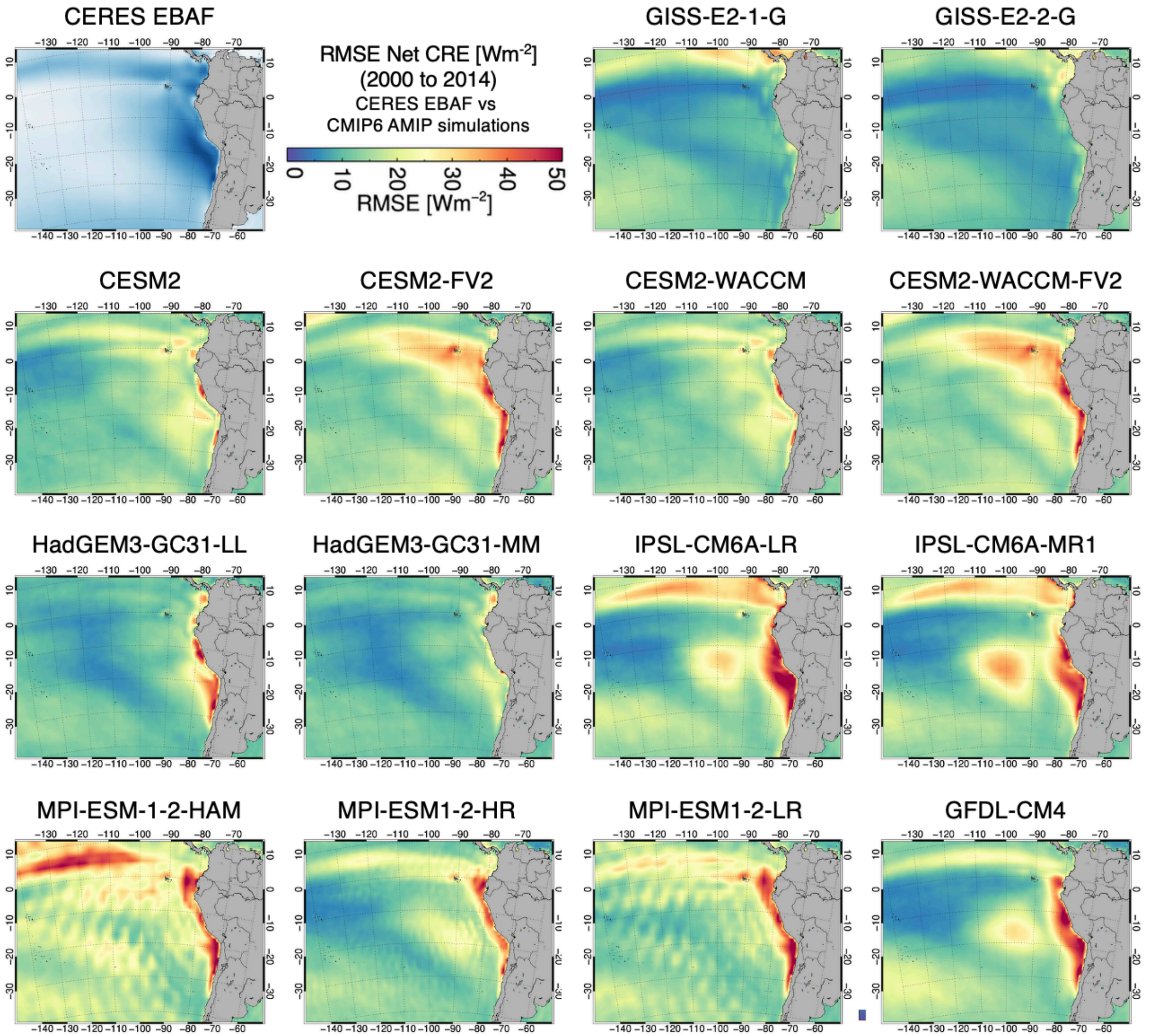

Figure A2: Map of RMSE of net CRE (Wm^{-2}) between CERES EBAF dataset and CMIP6 AMIP climate simulations.

Figure A3 shows maps of net CRE trends from CERES EBAF and CMIP6 AMIP climate simulations for the period from 2000 to 2014. According to CERES EBAF, the dominant trend during this period is a decrease in net CREs, indicating a strengthening of the cooling effects of clouds. This trend is consistent with the patterns observed from 2000 to 2023 in the study area. However, climate simulations reveal different spatial patterns of net CRE trends, with notable variations among them. Many CMIP6 simulations show a predominant increase in net CREs, with a significant rise. Net CRE is closely linked to Earth's energy budget and has a significant impact on surface and atmospheric temperature. Therefore, validation and evaluation climate simulations using observations are crucial for future projections.

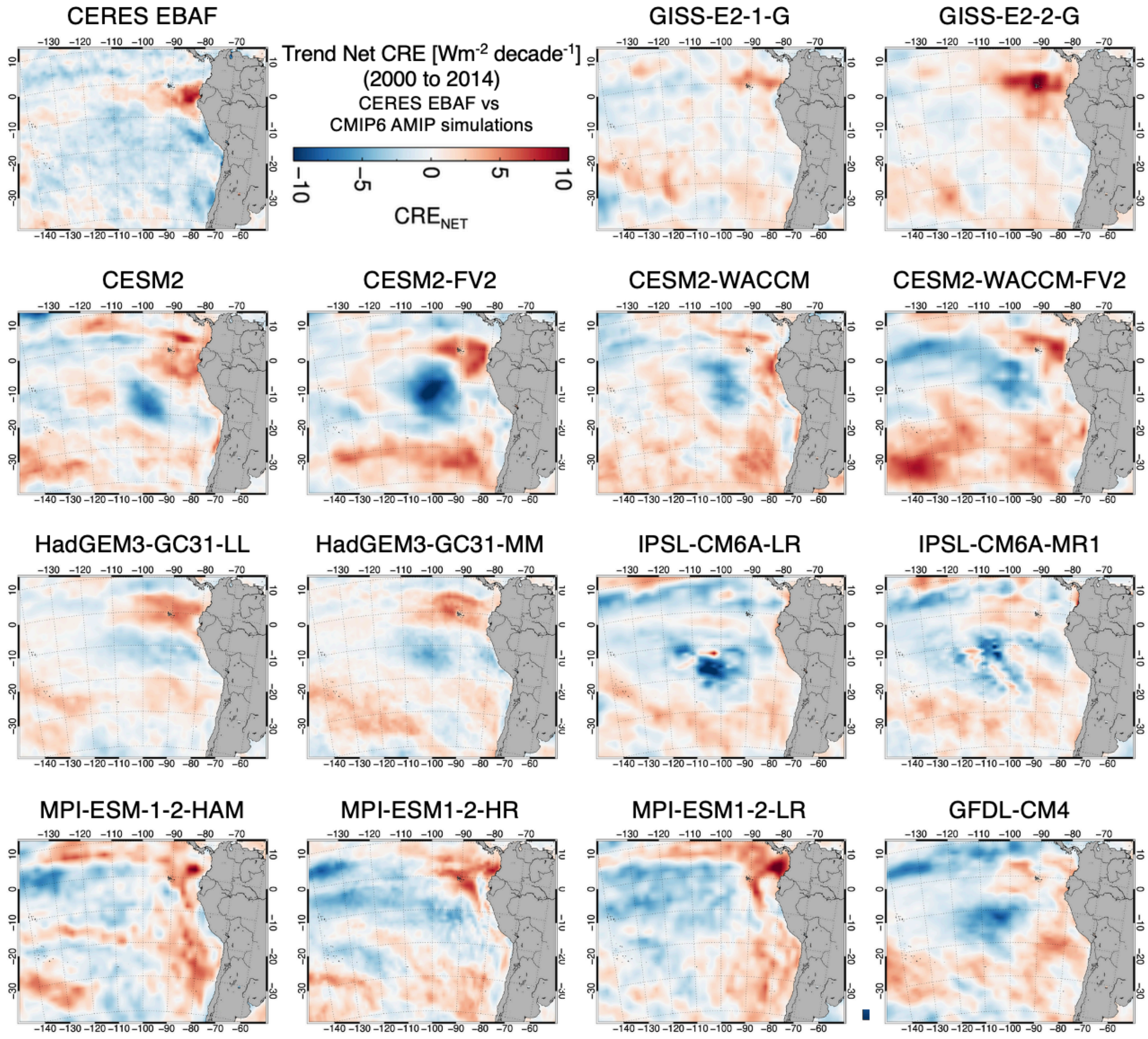

Figure A3: Map of trend in net CRE (Wm^{-2}) between CERES EBAF dataset and CMIP6 AMIP climate simulations.

Figure A4 shows maps of mean cloud fraction, a crucial component of CRE, from Pv6.0 and CMIP6 AMIP climate simulations for the period from 2000 to 2014. Overall, climate simulations tend to underestimate cloud fractions compared to observations over the study area, particularly in regions dominated by maritime stratocumulus clouds. Additionally, magnitudes and spatial features of mean cloud fractions vary across different climate models.

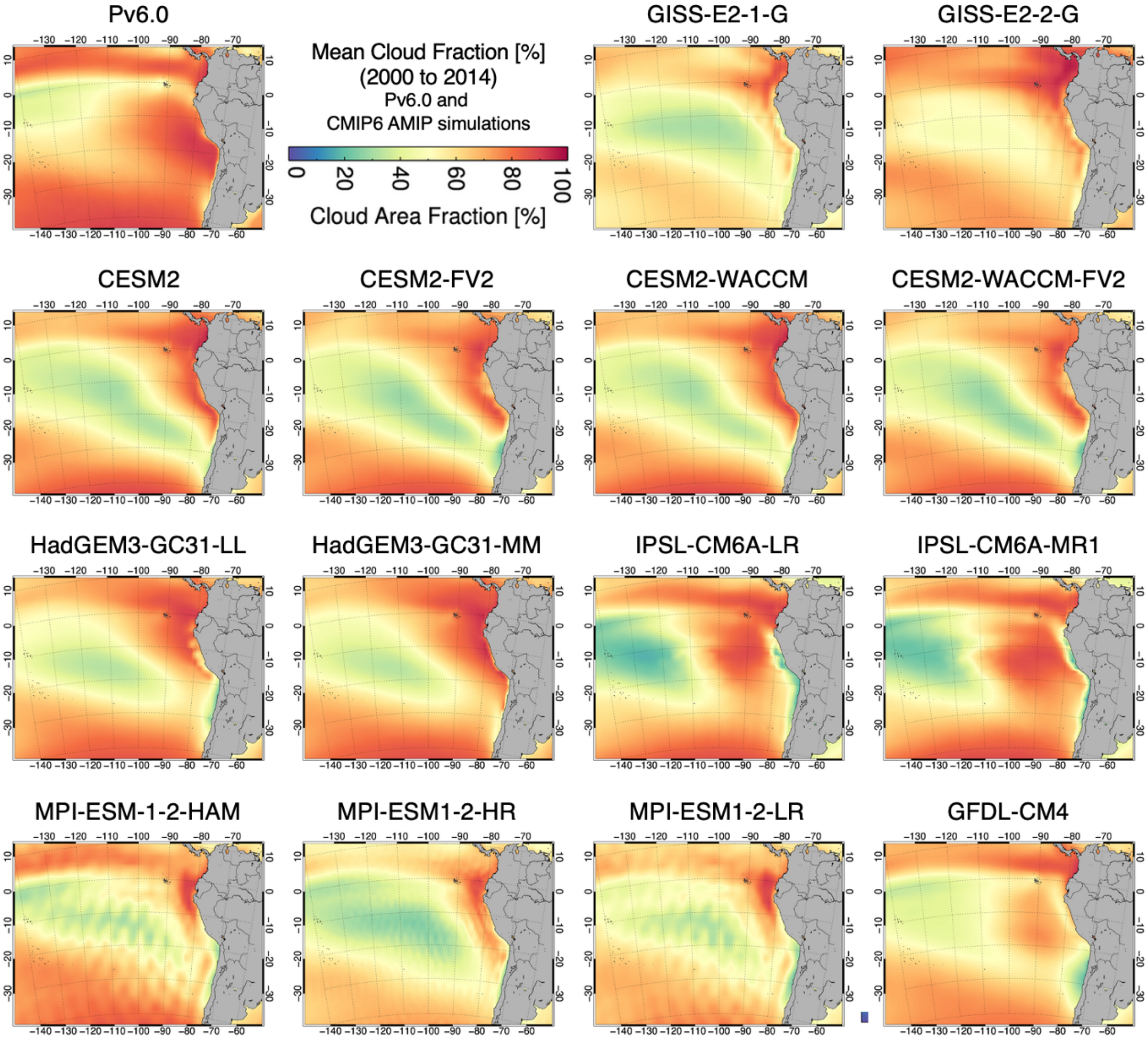

Figure A4: Map of mean cloud fraction (Wm^{-2}) from Pv6.0 dataset and CMIP6 AMIP climate simulations.

Figure A5 shows maps of RMSE of cloud fraction for total clouds between Pv6.0 and CMIP6 AMIP climate simulations for the period from 2000 to 2014. Due to the underestimation of cloud fraction in climate simulations, as shown in Figure A4, RMSE is especially high over the southeastern Pacific Ocean. Most clime models have a maximum RMSE exceeding 50 to 60%. This indicates that net CRE, especially for shortwave, from climate models can differ with observations due to the role of maritime stratocumulus clouds over this area.

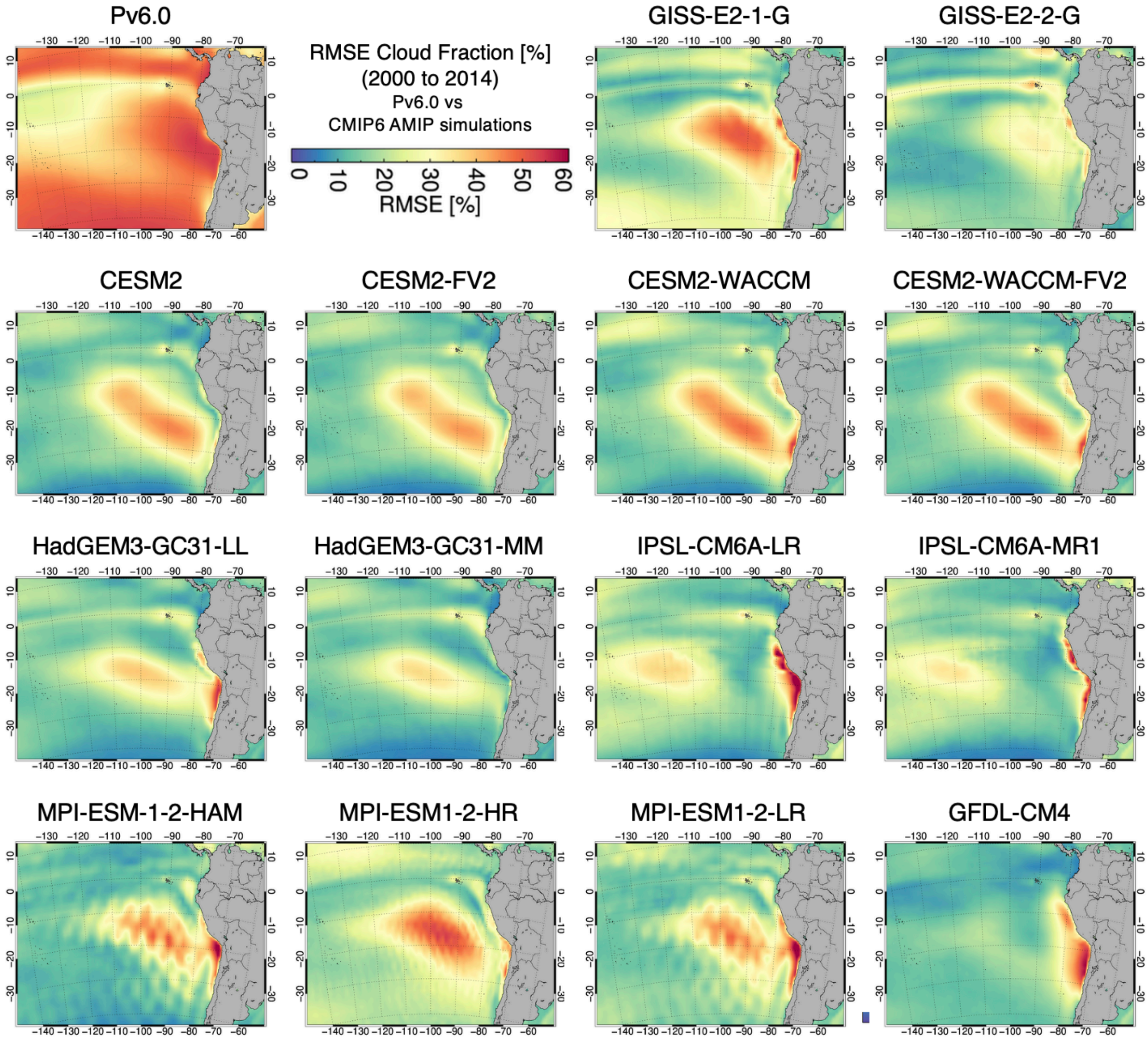

Figure A5: Map of RMSE of cloud fraction (Wm^{-2}) between Pv6.0 dataset and CMIP6 AMIP climate simulations.

Figure A6 shows maps of the trend in cloud fraction from Pv6.0 and CMIP6 AMIP climate simulations for the period from 2000 to 2014. Observations shows increases in total cloud fraction over the ITCZ region and some parts of the southeastern Pacific Ocean. However, most climate models differ from observations from each other in both the magnitude and spatial pattern of increases and decrease. It represents the high uncertainties of estimating cloud fraction from climate simulations because of that clouds must be parametrized to represent physical processes in climate simulations (Myers and Norris, 2016).

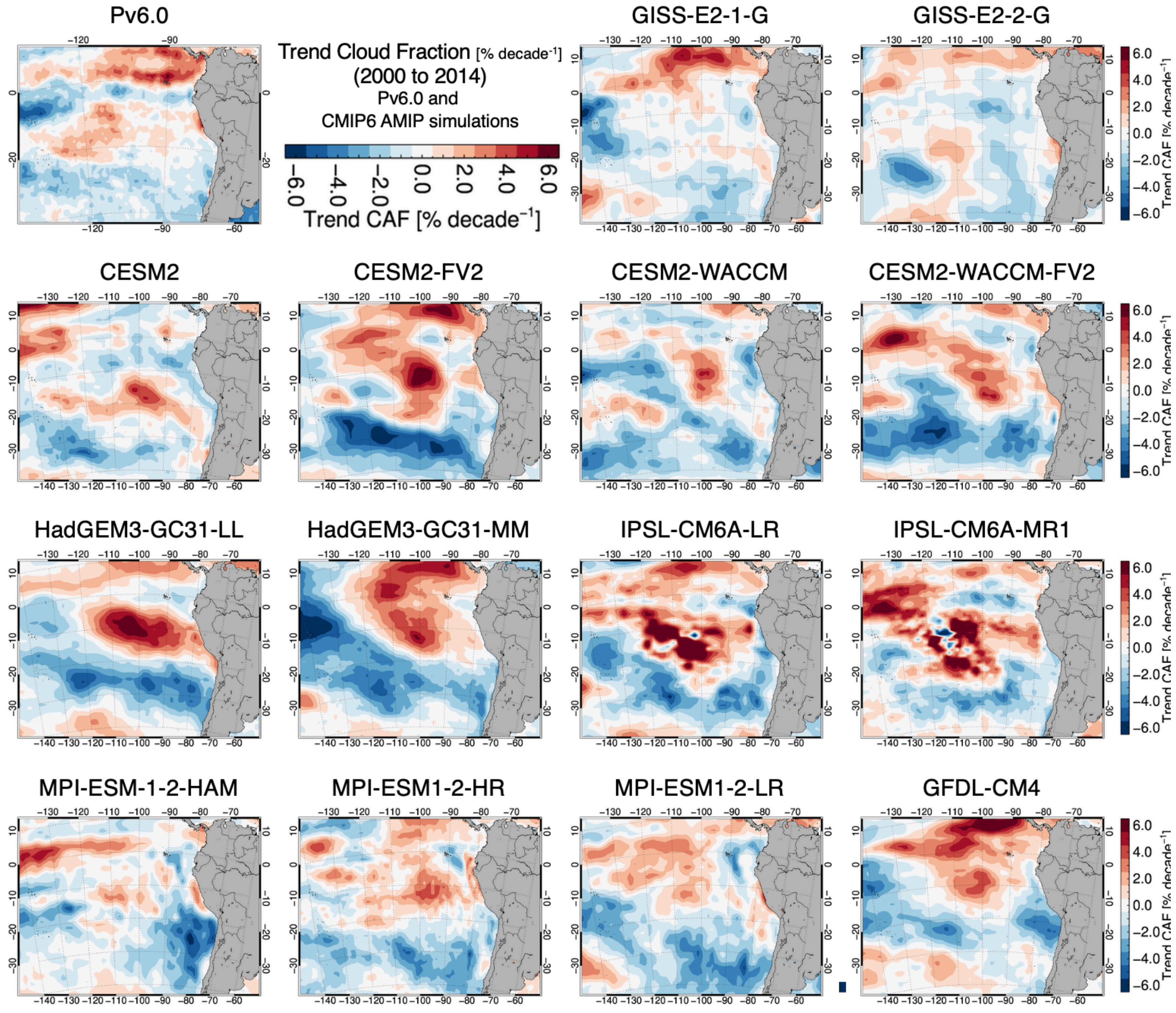

Figure A6: Map of trend in cloud fraction (Wm^{-2}) from Pv6.0 dataset and CMIP6 AMIP climate simulations.

Appendix B

Investigate influence of ENSO on these temperature changes over the southeastern Pacific Ocean.

The ENSO is the primary predictor for global climate distortions. These can persist over several seasons and thereby produce severe regional effect. The bi-monthly Multivariate ENSO index (MEI.v2) is the timeseries of the leading combined Empirical Orthogonal Function (EOF) of five different variables (sea level pressure (SLP), sea surface temperature (SST), zonal and meridional components of the surface wind, and outgoing longwave radiation (OLR)) over the tropical Pacific basin (30S-30N and 100E-70W), as shown in Figure A1. From 1980 to 1998, El Niño events were more frequent, while La Niña have been more dominant since 1999. Key features of composite positive MEI events (warm, El Niño) include anomalously warm SSTs across the east-central equatorial Pacific, anomalously high SLP over Indonesia and the western tropical Pacific and low SLP over the eastern tropical Pacific, reduction or reversal of tropical Pacific easterly winds (trade winds), suppressed tropical convection (positive OLR) over Indonesia and Western Pacific and enhanced convection (negative OLR) over the central Pacific. Key features of composite negative MEI events (cold, La Niña) are of mostly opposite phase.

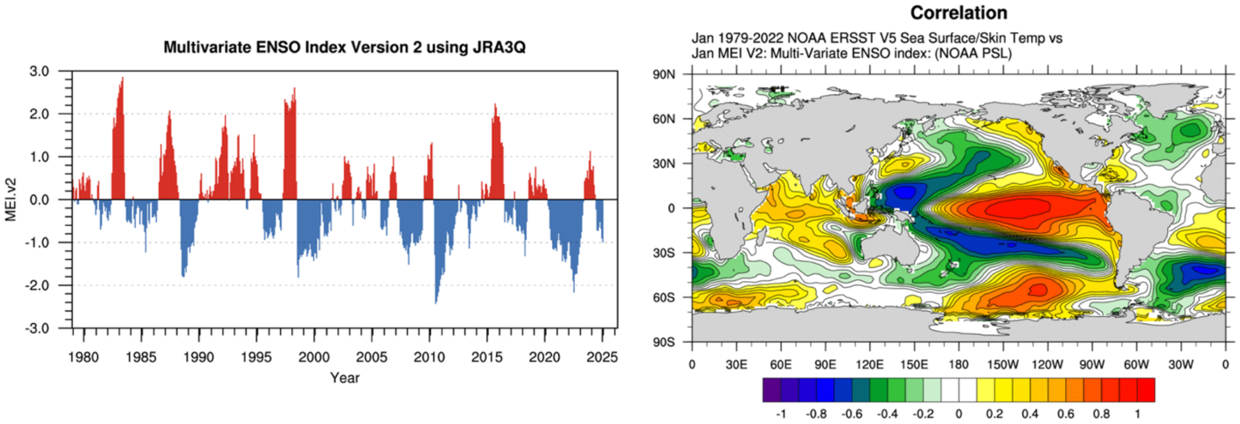

Figure B1: a) timeseries of MEI.v2 from https://psl.noaa.gov/enso/mei/. b) correlation between MEI.v2 and sea surface temperature from https://psl.noaa.gov/data/timeseries/month/DS/MEIV2.

Figure A2 shows the correlation coefficient between MEI.v2 and temperature at the surface and 700 hPa from the ERA5 reanalysis dataset from 1981 to 2023. In the southeastern Pacific Ocean, the correlation between surface temperature and MEI.v2 is positive north of 25°S, indicating an increase in surface temperature during positive MEI.v2 phases (El Niño). Conversely, a negative correlation is observed south of 25°S, where surface temperature decreases during El Niño events. Similarly, the correlation between atmospheric temperature at 700 hPa and MEI.v2 shows a pattern similar to that of surface temperature.

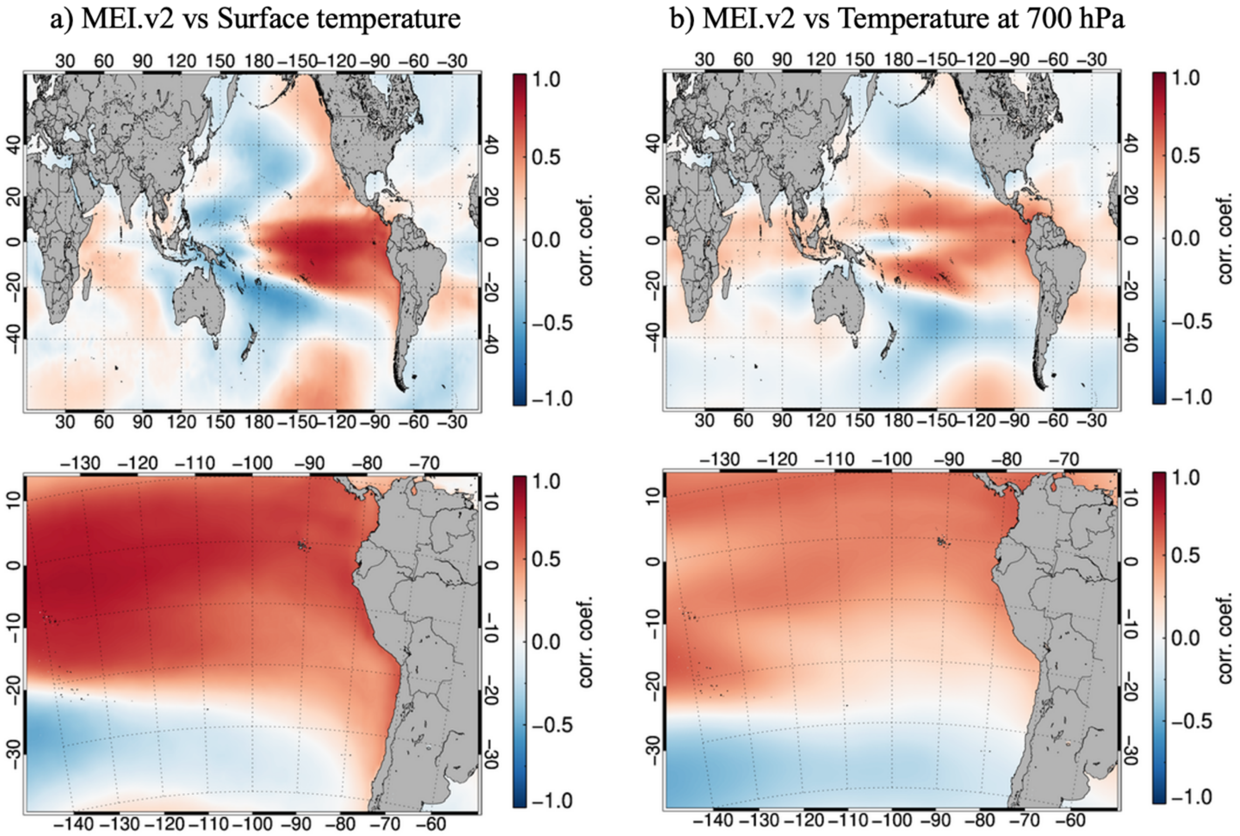

a) MEI.v2 vs Surface temperature

b) MEI.v2 vs Temperature at 700 hPa

Figure B2: a) map plot of correlation coefficient between MEI.v2 and surface temperature from ERA5. b) map plot of correlation coefficient between MEI.v2 and temperature at 700 hPa from ERA5. (Top: Global scale from 60°S to 60°N, Bottom: southeastern Pacific Ocean).

Figure A3 shows map of trends in temperature at the surface and 700 hPa from ERA5, along with trends derived using a linear regression method based on the relationship between ERA5 and MEI.v2 from 1981 to 2023. The trends in surface temperature derived using a linear regression also show decreases, but with a smaller magnitude compared to ERA5. Also, North of 5°S, the trends in surface temperature continue to show decreases, whereas trends from ERA5 indicate an increase. This discrepancy requires further investigation. The trends in atmospheric temperature at 700 hPa derived using a linear regression also show decreases, whereas trends from ERA5 show significant increases. Consequently, ENSO events can partially contribute to the decrease in surface temperature, but they alone cannot fully explain the trends in surface temperature and atmosphere temperature at 700 hPa observed in ERA5.

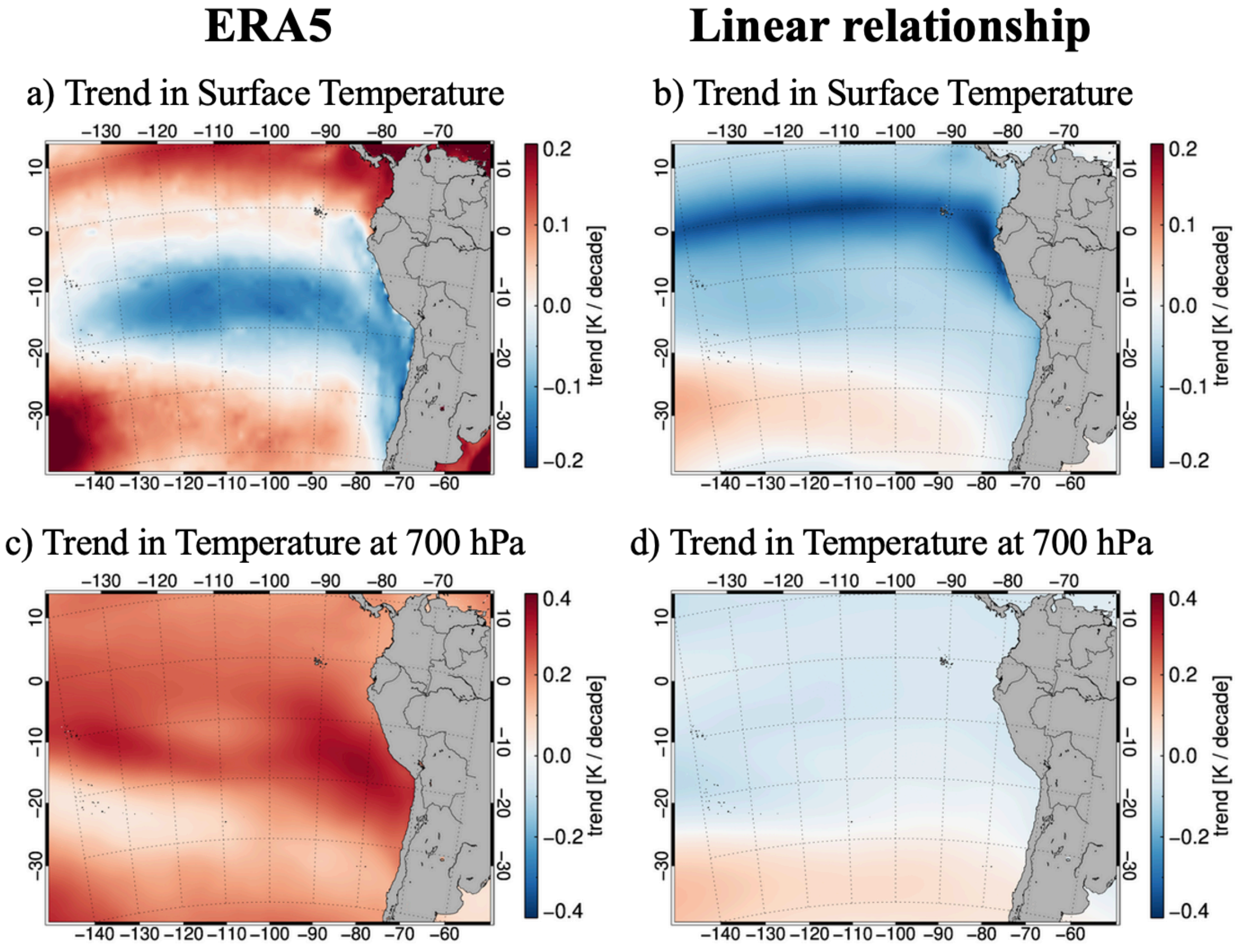

Figure B3: a) map plot of trends in surface temperature (a) and atmospheric temperature at 700 hPa (b) from ERA5, along with surface temperature (c) and atmospheric temperature at 700 hPa (d) derived using a linear relationship between MEI.v2 and ERA5.

Appendix C

Additional cloud controlling factor framework experiment.

This additional experiment was suggested by the Ph.D. committee members during the defense. Vertical velocity is particularly closely associated with relative humidity in high cloud processes over the tropical ocean. As shown in Figure 4.2, the spatial patterns of R-squared values for vertical velocity are similar to those for relative humidity, although the magnitudes are generally lower. Therefore, the main objective of this experiment is to evaluate the performance of the multilinear regression model without vertical velocity variables, in comparison to the model that includes all CCFs.

Figure C1 compares the performane of the multilinear regression model using all CCFs with a modified version that excludes vertical velocity, focusing on the R-squared values, mean cloud fraction, and their trends from 1981 to 2023 for water clouds. The left panels show results from the full model including vertical velocity, while the middle panels show the outputs without vertical velocity, and the right panels display the differences between the two. Removing vertical velocity results in a slight decrease in R-squared values across much of the tropics and subtropics, particularly over the midlatitudes.

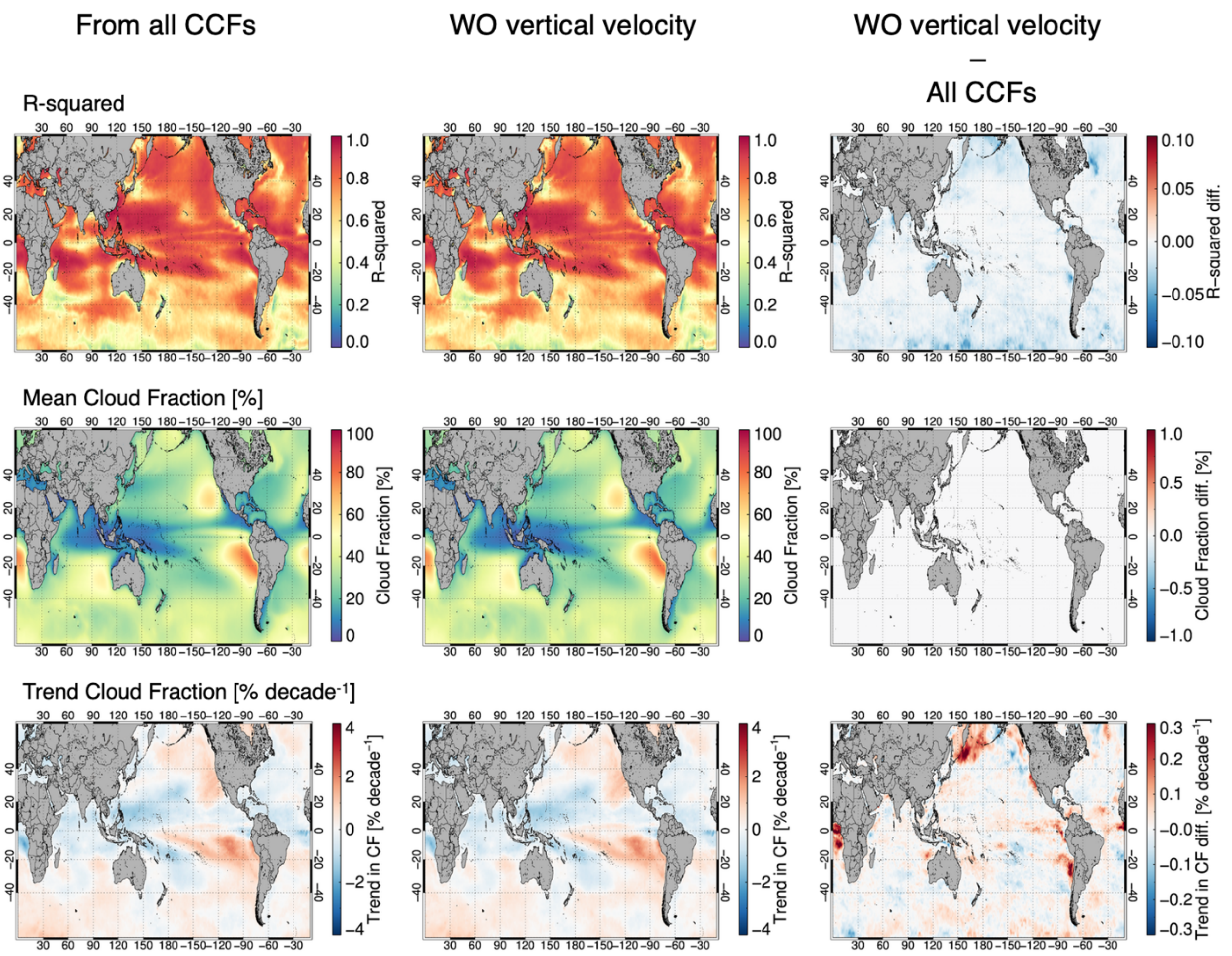

Figure C1: a) map plots of R-squared, mean, and trend of water cloud fractions from the multilinear regression model using all CCFs, all CCFs excluding vertical velocity, and their differences.

The mean cloud fraction fields remain nearly identical between the two models, with differences generally below 1%, implying that vertical velocity does not strongly affect the spatial distribution of average cloud cover. In contrast, the trends in water cloud fraction show more noticeable sensitivity to vertical velocity. The difference map highlights regions, such as the southeastern Pacific and western Indian Ocean, where omitting vertical velocity alters the estimated decadal trend by more than 0.2% per decade. These results suggest that while vertical velocity has a limited impact on mean cloud fraction, it is more influential in capturing regional cloud fraction trends and improving model performance, particularly in dynamically active regions.

Figure C2 presents the R-squared values, mean cloud fractions, and their trends derived from the multilinear regression model using all CCFs, compared to a model excluding vertical velocity, for the period from 1981 to 2023 for ice clouds. The difference maps in the right column highlight the impact of excluding vertical velocity. The R-squared values slightly decrease when vertical velocity is removed, particularly in convectively active regions such as the western Pacific, Indian Ocean, and South America, indicating that vertical motion contributes to explaining ice cloud variability, though its influence is modest compared to moisture-related factors.

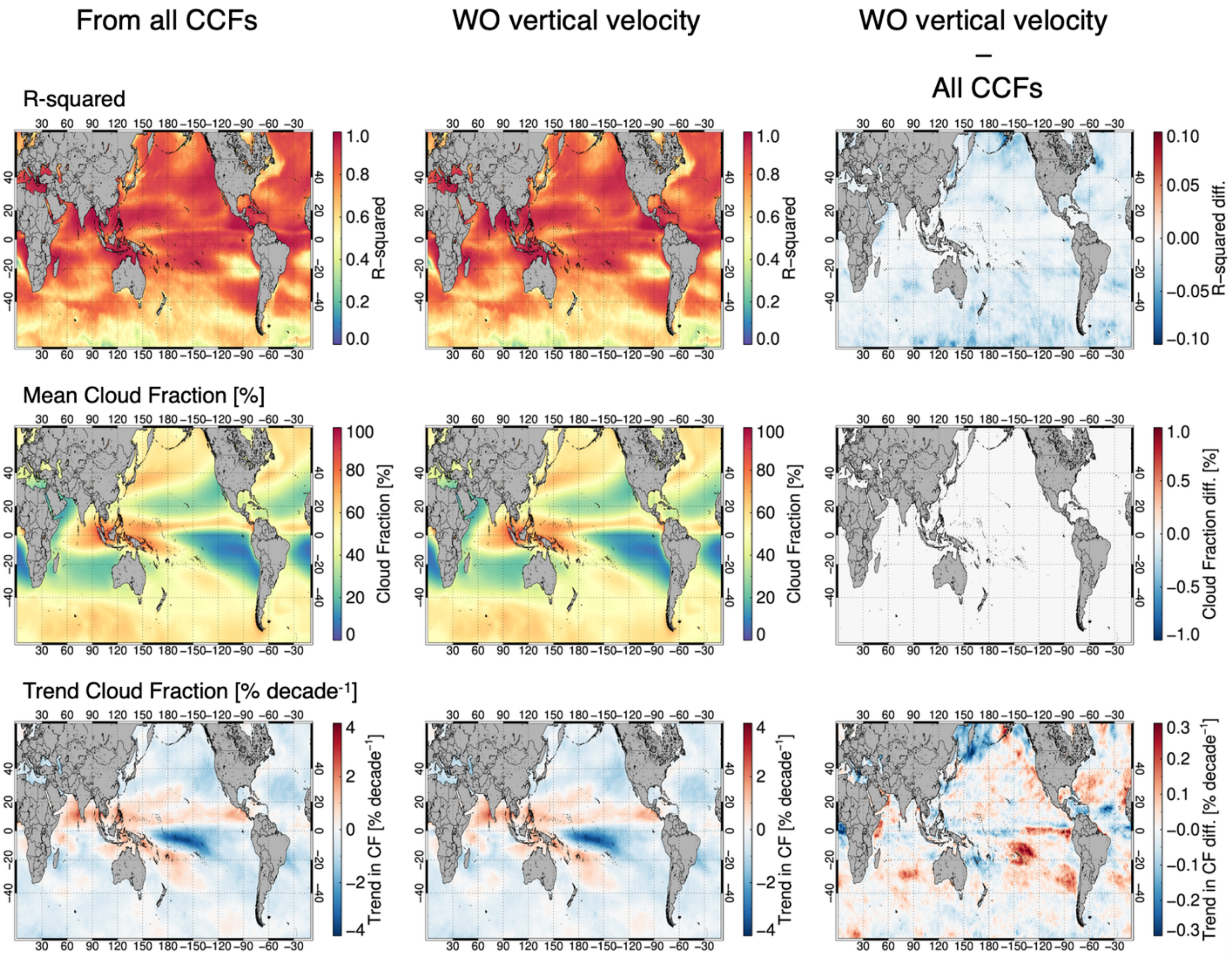

Figure C2: a) map plots of R-squared, mean, and trend of ice cloud fractions from the multilinear regression model using all CCFs, all CCFs excluding vertical velocity, and their differences.

The mean ice cloud fraction fields from both models remain nearly identical, with minimal differences under 1%, suggesting that vertical velocity has little effect on the average spatial distribution of ice clouds. However, the trend maps show more pronounced differences. Regions over the tropical Indian Ocean, the Maritime Continent, and parts of the Pacific exhibit changes in the trend magnitude exceeding ±0.2% per decade. These discrepancies imply that vertical velocity plays a more significant role in modulating temporal changes in ice clouds, likely through its connection to deep convection and large-scale vertical ascent. Overall, while the exclusion of vertical velocity has a limited effect on mean state estimates, it slightly reduces model performance and affects trend estimates in dynamically active regions.

Appendix D

Implementation of CCF frameworks in climate simulations.

Climate simulations are widely used to validate our understanding of atmospheric processes and to investigate future climate changes. They are useful for studying changes in clouds and their impact on Earth's radiation budget under different scenarios. Figure B1 shows a comparison between the satellite-based total cloud fraction from Pv6.0 and the corresponding outputs from the 14 CMIP6 AMIP climate simulations over the period from 1981 to 2014. The top-left panel shows the mean total cloud fraction from Pv6.0, while the middle-left panel presents the ensemble mean from the 14 climate simulations. The spatial distributions are broadly similar, capturing key large-scale patterns. The bottom-left panel shows the RMSE between the ensemble mean of the climate simulations and Pv6.0, highlighting regions of significant model-observation disagreement. RMSE values are particularly high over the maritime stratocumulus cloud regimes including the southeastern Pacific Ocean. This comparison underscores the importance of observational benchmarks for evaluating and constraining cloud simulations in climate models, particularly given the substantial spread in model performance across different regions.

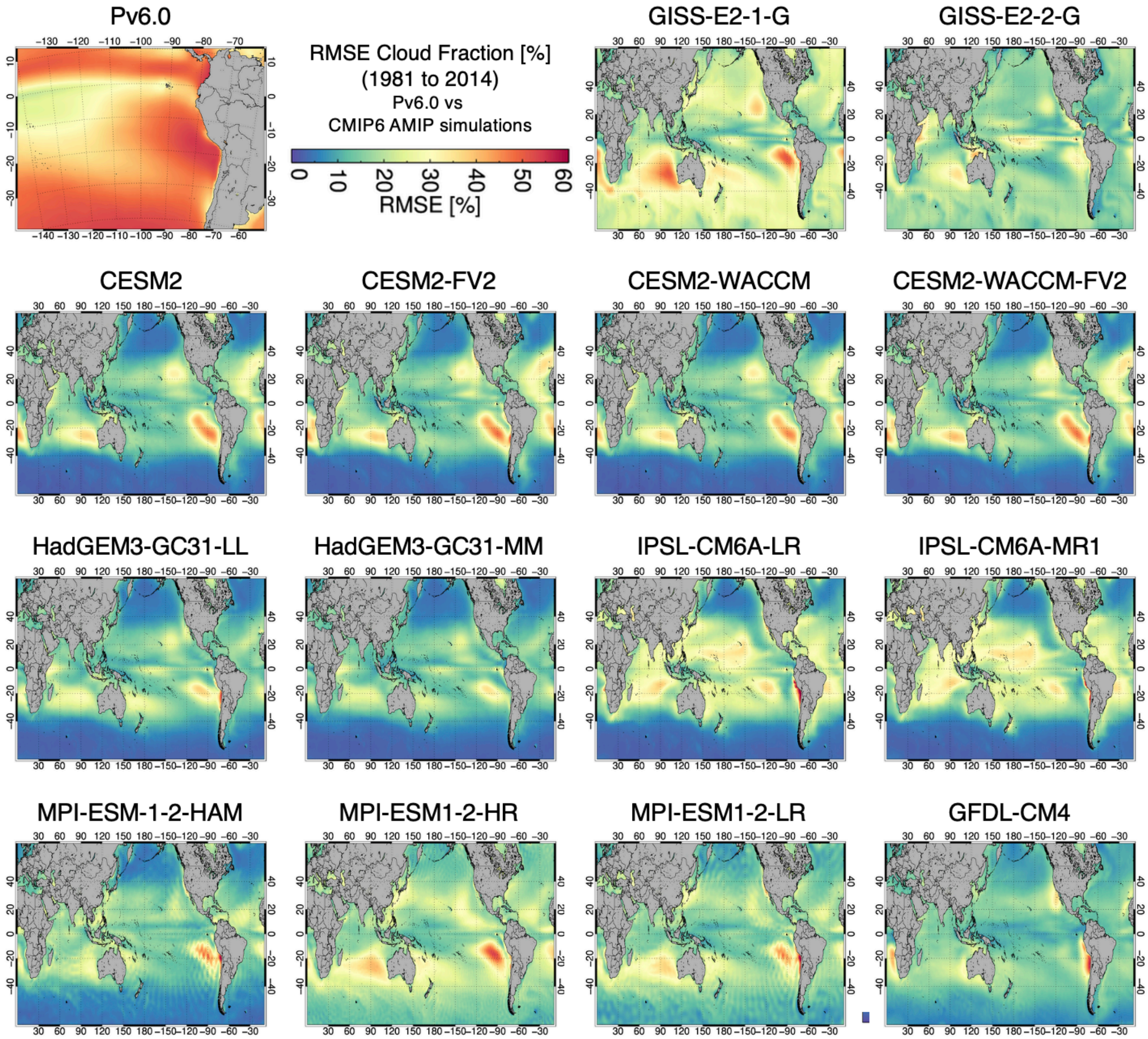

Figure D1: Maps of mean cloud fraction from Pv6.0 and ensemble mean from 14 CMIP6 AMIP climate simulations. Maps of RMSE between Pv6.0 and individual and ensemble mean from 14 climate simulations.

Figure D2 compares the CMIP6 AMIP climate simulations with the highest (Figure D2a) and lowest (Figure D2b) RMSE in total cloud fraction relative to the Pv6.0 dataset. Each colored region represents the model that contributes the most to the RMSE in that area, allowing for the identification of models with systematically poor or strong performance across different regions.

Figure D2a highlights the regions where individual models contribute most strongly to the highest RMSE simulation. Notably, the MPI-ESM1-2-HAM model frequently appears across the tropical oceans and the midlatitude storm tracks, indicating its relatively poor performance in capturing observed cloud fractions in these regions.

In contrast, Figure D2b shows the distribution of dominant model contributions in the simulation with the lowest RMSE. Here, models such as CESM2 and GFDL-ESM4 dominate large areas, particularly in the tropics and subtropics, suggesting their improved ability to replicate observed cloud distributions. These results emphasize the spatial heterogeneity in model performance and underscore the importance of model selection and evaluation when interpreting simulated cloud responses in climate projections. The identification of model-specific strengths and weaknesses can guide future model development and help prioritize regions for targeted improvements in cloud representation.

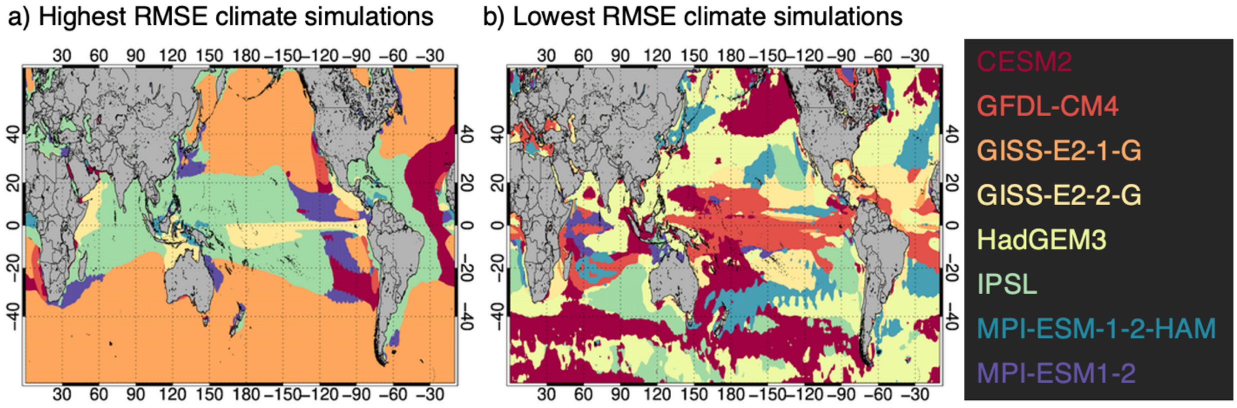

Figure D2: Maps of the CMIP6 climate simulation with the highest (left) and lowest (right) RMSE among the 14 climate simulations.

Figure D3 presents the spatial distribution of dominant CCFs influencing water and ice cloud fractions. Figure B3a and B3b show the CCFs that yield the highest coefficient of determination (R^2) in the multilinear regression models for water and ice clouds, respectively. Figure 3c and 3d display the individual CCFs with the largest absolute contributions to the predicted cloud fractions for water and ice clouds. In Figure B3a, estimated inversion strength (EIS, shown in dark blue) emerges as the dominant explanatory factor for water cloud variability across extensive regions, particularly over the subtropical eastern oceans and midlatitudes. This aligns with the well-established role of atmospheric stability in supporting low-level stratiform clouds. Similarly, Figure 3c confirms EIS as the most influential factor in water cloud fractions in these regions, highlighting its consistent importance both statistically (R^2) and dynamically (via contribution magnitude). Other influential factors include sea surface temperature (Tsfc, red) and lower-tropospheric stability (e.g., vertical velocity, green), particularly over the western Pacific and Indian Oceans.

For ice clouds (Figure D3b and D3d), water vapor and upper-tropospheric stability (UTS, dark blue) play major roles in both explanatory power and contribution magnitude. In tropical and midlatitude convective regions, ice cloud variability is often linked to thermodynamic conditions and large-scale ascent, as reflected by strong influences from vertical velocity and upper-tropospheric variables. This figure underscores the regional variability in dominant cloud-controlling factors and highlights distinct physical mechanisms shaping water and ice cloud distributions. These insights are essential for improving cloud representation in climate models and understanding cloud feedback in a warming climate.

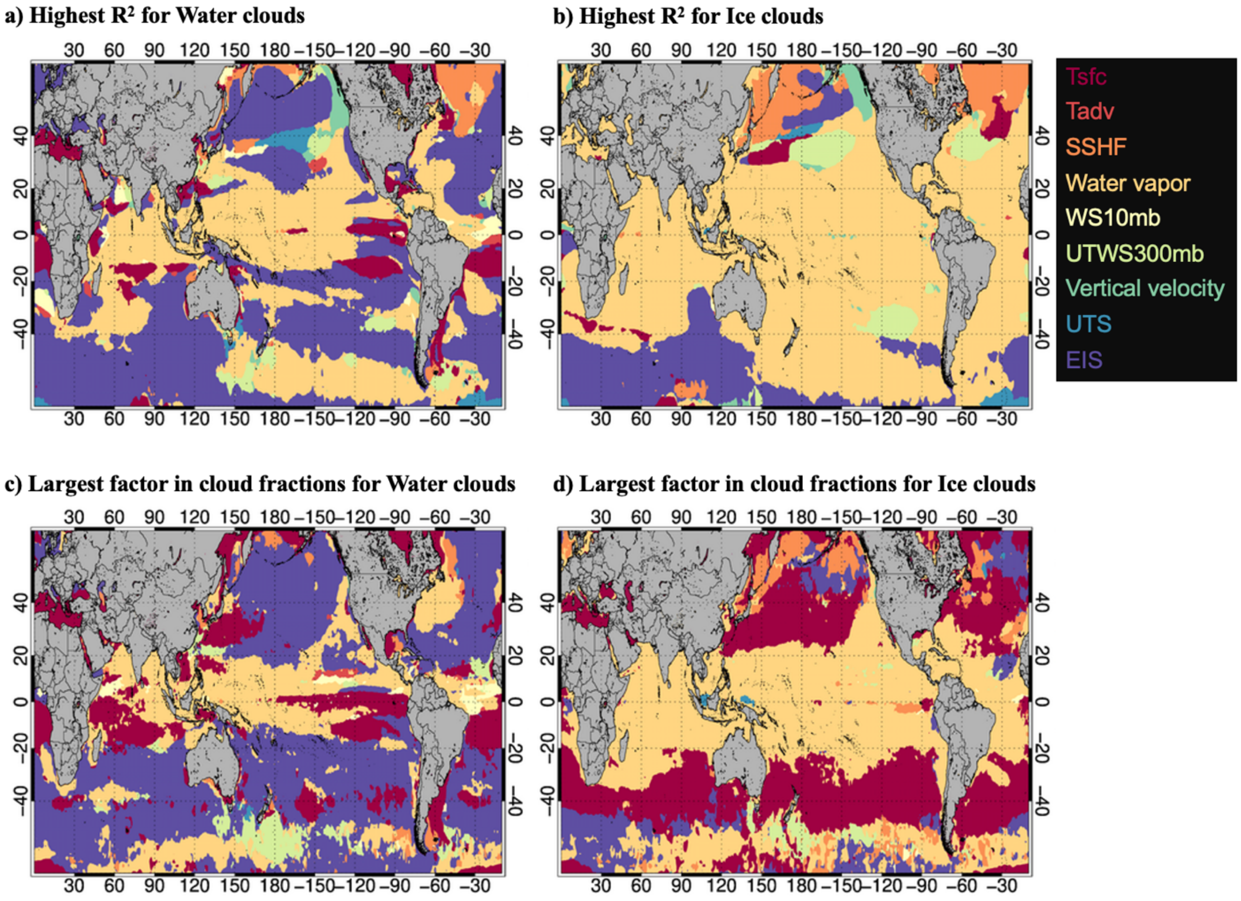
a) Highest R² for Water clouds

b) Highest R² for Ice clouds

c) Largest factor in cloud fractions for Water clouds

d) Largest factor in cloud fractions for Ice clouds

Figure E3: Maps of the CCF with the highest R-squared value (top) and the largest contribution to cloud fraction (bottom) for water clouds (left) and ice clouds (right).

Figure D4 evaluates the performance of a multilinear regression model in estimating cloud fractions based on CCFs from ten CMIP6 AMIP climate simulations, using Pv6.0 as the observational reference. Figure D4a shows the spatial distribution of the mean cloud fraction produced by the regression model, capturing key climatological patterns such as elevated cloudiness in the ITCZ, midlatitude storm tracks, and subtropical stratocumulus regions. Figure D4b presents the RMSE between the regression-based estimates and the observed Pv6.0 cloud fractions. Lower RMSE values are observed over subtropical and midlatitude oceanic regions, indicating that the regression model—driven by physically based CCFs—can effectively reproduce observed cloud distributions in many areas. However, higher RMSEs appear over convective zones such as the western Pacific and Indian Ocean, suggesting limitations in the linear framework for representing complex cloud dynamics in those regions.

The time series in Figure D4c further compares the temporal variability and trends in cloud fractions. The regression-based ensemble mean (red) more closely follows the Pv6.0 observations (black) than the direct CMIP6 AMIP climate simulations ensemble mean (blue), indicating that using CCFs within a regression framework can enhance agreement with observed climatology. The individual realizations (grey for direct CMIP6 output, yellow for regression estimates) show the spread in model variability, which remains large but is partially constrained by the regression approach. Overall, this figure highlights the potential of CCF-based statistical models to bridge gaps between climate model output and satellite observations, improving both spatial and temporal consistency in cloud fraction estimation.

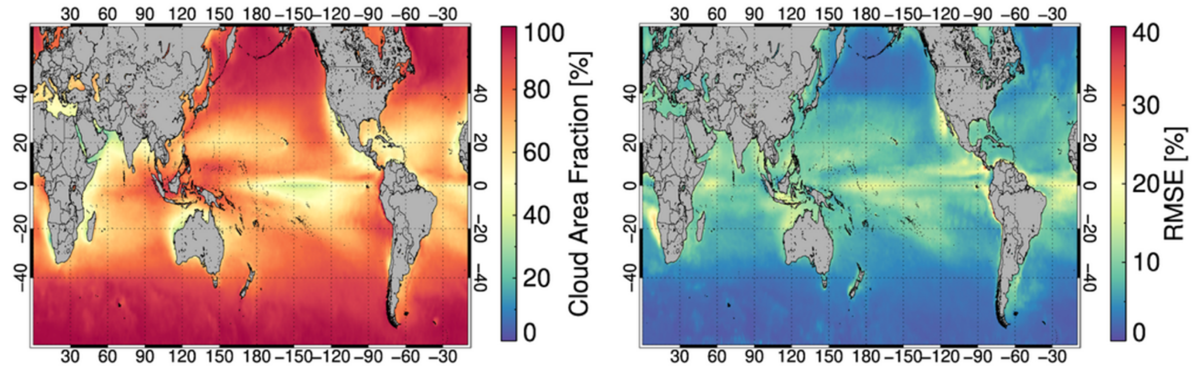

a) Mean Cloud Fraction [%]

b) RMSE [%]

c) Mean Cloud Fraction over the ocean from 60°S to 60°N [%]

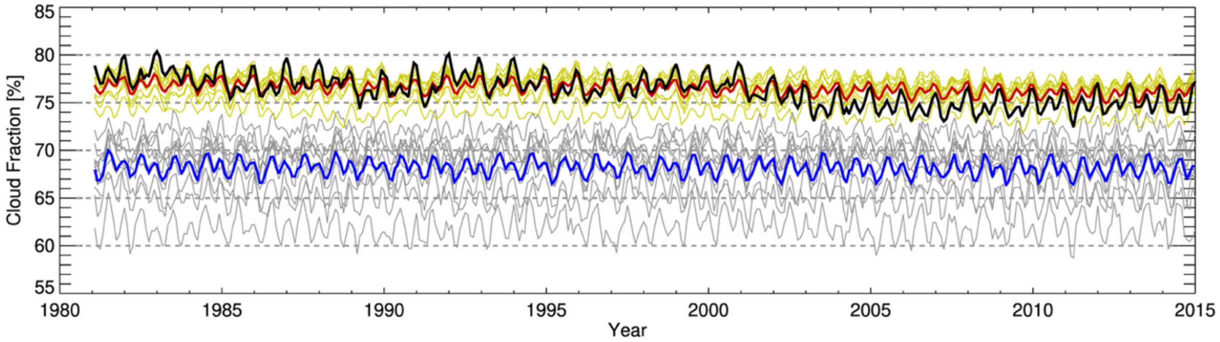

Figure D4: Maps of the mean cloud fraction (a) estimated using the multilinear regression model and CCFs from 14 CMIP6 AMIP climate simulations and RMSE (b) relative to Pv6.0. c: timeseries of mean cloud fraction over the ocean from 60°S to 60°N (Black: Pv6.0, Yello: individual mean cloud fraction estimated using the multilinear regression model and CCFs from 14 climate simulations, Red: ensemble mean of the cloud fraction estimated from the multilinear regression model and CCFs from 14 climate simulations, Blue: ensemble mean of the cloud fraction from the 14 climate simulations, Grey: individual mean cloud fractions from the 14 climate simulations).

Bibliography

Ackerman, S. A., A. K. Heidinger, M. J. Foster, and B. Maddux, 2013: Satellite Regional Cloud Climatology over the Great Lakes. *Remote Sens.*, **5**, 6223-6240, https://doi.org/10.3390/rs5126223.

Anber, U., S. Wang, and A. Sobel, 2014: Response of Atmospheric Convection to Vertical Wind Shear: Cloud-System-Resolving Simulations with Parameterized Large-Scale Circulation. Part I: Specified Radiative Cooling. *Journal of the Atmospheric Sciences*, **71**, 2976-2993, https://doi.org/10.1175/JAS-D-13-0320.1.

Andersen, H., J. Cermak, L. Zipfel, and T. A. Myers, 2022: Attribution of Observed Recent Decrease in Low Clouds Over the Northeastern Pacific to Cloud-Controlling Factors. *Geophysical Research Letters*, **49**, e2021GL096498, https://doi.org/10.1029/2021GL096498.

Andrade, J. M., A. R. Neto, R. L. B. Nobrega, M. A. Rico-Ramirez, and S. M. G. L. Montenegro, 2024: Efficiency of global precipitation datasets in tropical and subtropical catchments revealed by large sampling hydrological modelling. *Journal of Hydrology*, **663**, https://doi.org/10.1016/j.jhydrol.2024.131016.

Arking Albert, 1991: The Radiative Effects of Clouds and their Impact on Climate. *Bull. Amer. Meteor. Soc.*, **72**, 795-814, https://doi.org/10.1175/1520-0477(1991)072<0795:TREOCA>2.0.CO;2.

Barkstrom, B. R., 1984: The Earth Radiation Budget Experiment (ERBE). *Bull. Amer. Meteor. Soc.*, **65**, 1170-1185, https://doi.org/10.1175/1520-0477(1984)065<1170:TERBE>2.0.CO;2.

Bender, F. A.-M., L. Frey, D. T. McCoy, D. P. Grosvenor, and J. K. Mohrmann, 2019: Assessment of aerosol-cloud-radiation correlations in satellite observations, climate models and reanalysis. *Clim. Dyn.*, **52**, 4371-4392, https://doi.org/10.1007/s00382-018-4384-z.

Bi, K., L. Xie, H. Zhang, X. Chen, X. Gu, and Q. Tian, 2023: Accurate medium-range global weather forecasting with 3D neural networks. *Nature*, **619**, 533-538, https://doi.org/10.1038/s41586-023-06185-3.

Bojanowski, J. S., and J. P. Musial, 2020: Dissecting effects of orbital drift of polar-orbiting satellites on accuracy and trends of climate data records of cloud fractional cover. *Atmos. Meas. Tech.*, **13**, 6771-6788, https://doi.org/10.5194/amt-13-6771-2020.

Bony, S., K-M. Lau, and Y. C. Sud, 1997: Sea Surface Temperature and Large-Scale Circulation Influences on Tropical Greenhouse Effect and Cloud Radiative Forcing. *Journal of Climate*, **10**, 2055-2077, https://doi.org/10.1175/1520-0442(1997)010<2055:SSTALS>2.0.CO;2.

Bony, S., and J.-L. Dufresne, 2005: *Geophys. Res. Lett. Atmos.*, **32**, L20805, https://doi.org/10.1029/2005GL023851.

Bony, S., and Coauthors, 2016: Thermodynamic control of anvil cloud amount. *P. Natl. Acad. Sci. USA*, **113**(32), 8927-8932, https://doi.org/10.1073/pnas.1601472113.

Boucher, O., and Coauthors, 2013: Clouds and Aerosols. In: *Climate Change 2013: The Physical Science Basis. Contribution of Working Group I to the Fifth Assessment Report of the Intergovernmental Panel on Climate Change* [Stocker, T. F., D. Qin, G. -K. Plattner, M. Tignor, S. K. Allen, J. Boschung, A. Nauels, Y. Xia, V. Bex and P. M. Midgley (eds.)]. Cambridge University Press, Cambridge, United Kingdom and New York, NY, USA.

Boucher, O., and Coauthors, 2020: Presentation and Evaluation of the IPSL-CM6A-LR Climate Model. *Journal of Advances in Modeling Earth Systems*, **12** (7), e2019MS002010, https://doi.org/10.1029/2019MS002010.

Boutle, I. A., R. J. Beare, S. E. Belcher, A. R. Brown, and R. S. Plant, 2010: The Moist Boundary Layer under a Midlatitude Weather System. *Boundary-Layer Meteorology*, **134**, 367-386, https://doi.org/10.1007/s10546-009-9452-9.

Brient, F., T. Schneider, Z. Tan, S. Bony, X. Qu, and A. Hall, 2016: Shallowness of tropical low clouds as a predictor of climate models' response to warming. *Climate Dynamics*, **47**, 433-449, https://dor.org/10.1007/s00382-015-2846-0.

Ceppi, P., F. Brient, M. D. Zelinka, and D. L. Hartmann, 2017: Cloud feedback mechanisms and their representation in global climate models. *WIREs Climate Change*, **8**, e465, https://doi.org/10.1002/wcc.465.

Ceppi, P., F. and P. Nowack, 2021: Observational evidence that cloud feedback amplifies global warming. Earth, *Atmospheric, and Planetary Sciences*, **118** (30), e2026290118, https://doi.org/10.1073/pnas.2026290118.

Cermak, J., and Coauthors, 2010: Consistency of global satellite-derived aerosol and cloud data sets with recent brightening observations. *Geophys. Res. Lett.*, **37**, L21704, https://doi.org/10.1029/2010GL044632.

Cesana, G., H. Chepfer, 2012: How well do climate models simulate cloud vertical structure? A comparison between CALIPSO-GOCCP satellite observations and CMIP5 models. *Geophys. Res. Lett.*, **39**, L20803, https://doi.org/10.1029/2012GL053153.

Chen, T., W. B. Rossow, and Y. Zhang, 2000: Radiative Effects of Cloud-Type Variations. *Journal of climate*, **13**, 264-286, https://doi.org/10.1175/1520-0442(2000)013<0264:REOCTV>2.0.CO;2.

Cherian, R., and J. Quaas, 2020: Trends in AOD, Clouds, and Cloud Radiative Effects in Satellite Data and CMIP5 and CMIP6 Model Simulations Over Aerosol Source Regions. *Geophysical Research Letters*, **47**, e2020GL087132, https://doi.org/10.1029/2020GL087132.

Curry, J. A., and E. E. Ebert, 1992: Annual Cycle of Radiation Fluxes over the Arctic Ocean: Sensitivity to Cloud Optical Properties. Journal of Climate,

Cutler, L., M. A. Brunke, and X. Zeng, 2022: Re-Evaluation of Low Cloud Amount Relationships With Lower-Tropospheric Stability and Estimated Inversion Strength. *Geophysical Research Letters*, **49**, e2022GL098137, https://doi.org/10.1029/2022GL098137.

Devasthale, A., and K.-G. Karlsson, 2023: Decadal Stability and Trends in the Global Cloud Amount and Cloud Top Temperature in the Satellite-Based Climate Data Records. *Remote. Sens.*, **15**(15), 3819, https://doi.org/10.3390/rs15153819.

Döscher, R., and Coauthors, 2022: The EC-Earth3 Earth system model for the Coupled Model Intercomparison Project 6. *Geoscientific Model Development*, **15** (7), 2973-3020, https://doi.org/10.5194/gmd-15-2973-2022.

Dunne, J. P., and Coauthors, 2020: The GFDL Earth System Model Version 4.1 (GFDL-ESM 4.1): Overall Coupled Model Description and Simulation Characteristics. *Journal of*

Advances in Modeling Earth Systems, **12** (11), e2019MS002015, https://doi.org/10.1029/2019MS002015.

Eliasson, S., S. A. Buehler, M. Milz, P. Eriksson, and V. O. John, 2011: Assessing observed and modelled spatial distributions of ice water path using satellite data. *Atmos. Chem. Phys*., **11**, 375-391, https://doi.org/10.5194/acp-11-375-2011.

Eyring, V., and Coauthors, 2016: Overview of the Coupled Model Intercomparison Project Phase 6 (CMIP6) experimental design and organization. *Geosci. Model Dev*., **9**, 1937-1958, https://doi.org/10.5194/gmd-9-1937-2016.

Falvey, M., and R. D. Garreaud, 2009: Regional cooling in a warming world: Recent temperature trends in the southeast Pacific and along the west coast of subtropical South America (1979-2006). *J. Geophys. Res*., **114**, D04102, https://doi.org/10.1029/2008JD010519.

Fermepin, S., and S. Bony, 2014: Influence of low-cloud radiative effects on tropical circulation and precipitation. *Journal of Advances in Modeling Earth Systems*, **6**, 513-526, https://doi.org/10.1002/2013MS000288.

Foster, J. M., and A. K. Heidinger, 2013: PATMOS-x: Results from a Diurnally Corrected 30-yr Satellite Cloud Climatology. *J. Climate*, **26**, 414-425, https://doi.org/10.1175/JCLI-I-11-00666.1.

Foster, J. M., and Coauthors, 2016: PATMOS-x Cloud Climate Record Trend Sensitivity to Reanalysis Products. *Remote Sens.*, **8**, 424, https://doi.org/10.3390/rs8050424.

Foster, J. M., and Coauthors, 2019: Cloudiness [in "State of the Climate in 2018"]. *Bull. Amer. Meteor. Soc.*, **95**(7), S22-S23, https://doi.org/10.1175/2014BAMSStateoftheClimate.1.

Foster, J. M., C. Phillips, A. K. Heidinger, E. E. Borbas, Y. Li, W. P. Menzel, A. Walther, and E. Weisz, 2023: PATMOS-x Version 6.0: 40 years of Merged AVHRR and HIRS Global Cloud Data. *J. Climate*, **36**, 1143-1160, https://doi.org/10.1175/JCLI-D-22-0147.1.

Frey W. R., and J. E. Kay, 2017: The influence of extratropical cloud phase and amount feedbacks on climate sensitivity. *Climate Dynamics*, **50**, 3097-3116, https://doi.org/10.1007/s00382-017-0396-5.

Ge, J., Z. Wang, C. Wang, X. Yang, Z. Dong, and M. Wang, 2021: Diurnal Variations of global clouds observed from the CATS spaceborne lidar and their links to large-scale meteorological factors. *Climate Dynamics*, **57**, 2637-2651, https://doi.org/10.1007/s00382-021-05829-2.

Gelaro, R., Coauthors, 2017: The Modern-Era Retrospective Analysis for Research and Applications, Version 2 (MERRA-2). *J. Clim*, **30**, 5419-5454, https://doi.org/10.1175/JCLI-D-16-0758.1.

Ghausi, S. A., Y. Tian, E. Zehe, and A. Kleidon, 2023: Radiative controls by clouds and thermodynamics shape surface temperatures and turbulent fluxes over land. *Earth, Atmospheric and Planetary Sciences*, **120 (29)**, e2220400120, https://doi.org/10.1073/pnas.2220400120.

Goessling, H. F., T. Rackow, and T. Jung, 2025: Recent global temperature surge intensified by record-low planetary albedo. *Science*, **387**, 68-73, https://doi.org/10.1126/science.adq7280.

Gordon, N. D., and S. A. Klein, 2014: Low-cloud optical depth feedback in climate models. *Journal of Geophysical Research Atmospheres*, **119**, 6052-6065, https://doi.org/10.1002/2013JD021052.

Grise K. M., and M. K. Kelleher, 2021: Midlatitude Cloud Radiative Effect Sensitivity to Cloud Controlling Factors in Observations and Models: Relationship with Southern Hemisphere Jet Shifts and Climate Sensitivity. *Journal of Climate*, **34**, 5869-5886, https://doi.org/10.1175/JCLI-D-20-0986.1.

Grise K. M., and G. Tselioudis, 2024: Understanding the Relationship between Cloud Controlling Factors and the ISCCP Weather States. *Journal of Climate*, **37**, 5387-5403, https://doi.org/10.1175/JCLI-D-24-0011.1.

Ham, S.-H., and Coauthors, 2017: Cloud occurrences and cloud radiative effects (CREs) from CERES-CALIPSO-CloudSat-MODIS (CCCM) and CloudSat radar-lidar (RL) products. *Journal of Geophysical Research Atmospheres*, **122**, 8852-8884, https://doi.org/10.1002/2017JD026725.

Harrison, E. F., P. Minnis, B. R. Barkstrom, V. Ramanathan, D. Cess., G. G. Gibson, 1990: Seasonal variation of cloud radiative forcing derived from the Earth Radiation Budget

Experiment. *Geophys. Res. Lett., Atmos.*, **95**, 19687-18703, https://doi.org/10.1029/JD095iD11p18687.

Hartmann, D. L., M. E. Ockert-Bell, and M. L. Michelsen, 1992: The Effect of Cloud Type on Earth's Energy Balance: Global Analysis. *J. Climate*, **5**, 1281-1304, https://www.jstor.org/stable/26197118.

Hartmann, D. L., and S. E. Berry, 2017: The balanced radiative effect of tropical anvil clouds. *Journal of Geophysical Research Atmospheres*, **122**, 5003-5020, https://doi.org/10.1002/2017JD026460.

Harrop, B. E., and D. L. Hartmann, 2016: The role of cloud radiative heating within the atmosphere on the high cloud amount and top-of-atmosphere cloud radiative effect. *Journal of Advances in Modeling Earth Systems*, **8**, 1391-1410, https://doi.org/10.1002/2016MS000670.

Heidinger, A. K., C. Cao, and J. T. Sullivan, 2002: Using Moderate Resolution Imaging Spectrometer (MODIS) to calibrate Advanced Very High Resolution Radiometer reflectance channels. *J. Geophys. Res.*, **107**, 4702, https://doi.org/10.1029/2001JD002035.

Heidinger, A. K., J. T. Sullivan, and C. R. Nagaraja Rao, 2003: Calibration of visible and near-infrared channels of the NOAA-12 AVHRR using time series of observations over deserts. *Int. J. Remote Sens*, **24**(18), 3635-3649, https://doi.org/10.1080/0143116021000023907.

Heidinger, A. K., M. D. Goldberg, D. Tarpley, A. Jelenak, and M. J. Pavolonis, 2005: A new AVHRR cloud climatology. Proc. SPIE 5658, Applications with Weather Satellites II, https://doi.org/10.1117/12.579047.

Heidinger, A. K., and M. J. Pavolonis, 2009: Gazing at cirrus clouds for 25 years through a spilt-window. Part I: Methodology. *J. Appl. Meteor. Climatol.*, **28**, 1100-1116, https://doi.org/10.1175/2008JAMC1882.1.

Heidinger, A. K., W. C. Straka, C. C. Molling, J. T. Sullivan, and X. Q. Wu, 2010: Deriving an inter-sensor consistent calibration for the AVHRR solar reflectance data record. *Int. J. Remote Sens.*, **31**, 6493-6517, https://doi.org/10.1080/01431161.2010.496472.

Heidinger, A. K., M. J. Foster, and A. T. Evan, 2012: A CALIPSO derived naïve Bayesian cloud detection scheme for the Pathfinder Atmospheres Extended (PATMOS-x) dataset. *J. Appl. Meteor. Climatol.*, **51**, 1129-1144, https://doi.org/10.1175/JAMC-D-11-02.1.

Heidinger, A. K., M. J. Foster, A. Walther, and X. Zhao, 2014: THE PATHFINDER ATMOSPHERES-EXTENDED AVHRR CLIMATE DATASET. *Bull. Amer. Meteor. Soc.*, **95**, 909-922, https://doi.org/10.1175/BAMS-D-12-00246.1.

Heidinger, A. K., M. J. Foster, D. Botambekov, M. Hiley, A. Walther, and Y. Li, 2016: Using the NASA EOS A-Train to Probe the Performance of the NOAA PATMOS-x Cloud Fraction CDR. *Remote Sens*, **8** (6) 511, https://doi.org/10.3390/rs8060511.

Heidinger, A. K., and Coauthors, 2020: Chapter 6 – ABI Cloud Products from the GOES-R Series. *Elsevier*, pp. 43-62, https://doi.org/10.1016/B978-0-12-814327-8.00006-8.

Henken, C. K., H. Diedrich, R. Preusker, and J. Fischer, 2015: MERIS full-resolution total column water vapor: Observing horizontal convective rolls. *Geophysical Research Letters* ,**42**, 10,074-10,081, https://doi.org/10.1002/2015GL066650.

Hersbach, H., and Coauthors, 2020: The ERA5 global reanalysis. *Royal Meteorol. Soc.*, 146(730), 1999-2049, https://doi.org/10.1002/qj.3803.

Hill, P. G., C. E. Holloway, M. P. Byrne, F. H. Lambert, and M. J. Webb, 2023: Climate models underestimate dynamic cloud feedbacks in the tropics. *Geophys. Res. Lett.*, **50**, e2023GL104573, https://doi.org/10.1029/2023GL104573.

Hong, Y., G. Liu, and J.-L. F. Li, 2016: Assessing the Radiative Effects of Global Ice Clouds Based on *CloudSat* and *CALIPSO* Measurements. *Journal of Climate*, **29**, 7651-7674, https://doi.org/10.1175/JCLI-D-15-0799.1.

Ignatov, A., I. Laszlo, E. D. Harrod, K. B. Kidwell, and G. P. Goodrum, 2004: Equator crossing times for NOAA, ERS and EOS sun-synchronous satellites. *Int. J. Remote Sens.*, **25**, 5255-5266, https://doi.org/10.1080/01431160410001712981.

Illingworth, A. J., and Coauthors, 2007: Continuous Evaluation of Cloud Profiles in Seven Operational Models Using Ground-Based Observations. *Bull. Amer. Meteor. Soc*, **88**, 883-898, https://doi.org/10.1175/BAMS-88-6-883.

Jacobowitz, H., L. L. Stowe, G. Ohring, A. K. Heidinger, K. Knapp, and N. R. Nalli, 2003: The Advanced Very High Resolution Radiometer Pathfinder Atmosphere (PATMOS) climate dataset: A resource for climate research. *Bull. Amer. Meteor. Soc.*, **84**, 785-793, https://doi.org/10.1175/BAMS-84-6-785.

Janowiak, J. E., and P. A. Arkin, 1991: Rainfall variations in the tropics during 1986-1989, as estimated from observations of cloud-top temperature. *Journal of Geophysical Research Oceans*, **96**, 3359-3373, https://doi.org/10.1029/90JD01856.

Jensen, E. J., S. Kinne, and O. B. Toon, 1994: Tropical cirrus cloud radiative forcing: Sensitivity studies. *Geophysical Research Letters*, **21**, 2023-2026, https://doi.org/10.1029/94GL01358.

Jensen, E. J., L. Pfister, and O. B. Toon, 2011: Impact of radiative heating, wind shear, temperature variability, and microphysical processes on the structure and evolution of thin cirrus in the tropical tropopause layer. *Journal of Geophysical Research Atmospheres*,**116**, D12, https://doi.org/10.1029/2010JD015417.

Jian, B., J. Li, G. Wang, Y. Zhao, Y. Li, J. Wang, M. Zhang, and J. Huang, 2021: Evaluation of the CMIP6 marine subtropical stratocumulus cloud albedo and its controlling factors. *Atmospheric Chemistry and Physics*, **21**, 9809-9828, https://doi.org/10.5194/acp-21-9809-2021.

Jones A. D., D. Rastogi, P. Vahmani, A. M. Stansfield, K. A. Reed, T. Thurber, P. A. Ullrich and J. S. Rice, 2023: Continental United States climate projections based on thermodynamic modification of historical weather. *Scientific Data*, **10**, 664, https://doi.org/10.1038/s41597-023-02485-5.

Karagiannidis, A., K. Lagouvardos, S. Lykoudis, V. Kotroni, T. Giannaros, and H.-D. Betz, 2019: Modeling lightning density using cloud top parameters. *Atmospheric Research*, **222**, 163-171, https://doi.org/10.1016/j.atmosres.2019.02.013.

Karl, T. R., and K. E. Trenberth, 2003: Modern Global Climate Change. *Science*, **302**, 1719-1723, https://doi.org/10.1126/science.1090228.

Karlsson, K-G., and N. Håkansson, 2018: Characterization of AVHRR global cloud detection sensitivity based on CALIPSO-CALIOP cloud optical thickness information: demonstration of results based on the CM SAF CLARA-A2 climate data record. *Atmos. Meas. Tech.*, **11**, 633-649, https://doi.org/10.5194/amt-11-633-2018.

Karlsson, K-G., and Coauthors, 2023: CLARA-A3: The third edition of the AVHRR-based CM SAF climate data record on clouds, radiation and surface albedo covering the period 1979 to 2023. *Earth Syst. Sci. Data,* **15**, 4901, 4926, https://doi.org/10.5194/essd-15-4901-2023.

Kawai, H., T. Koshiro, and M. J. Webb, 2017: Interpretation of Factors Controlling Low Cloud Cover and Low Cloud Feedback Using a Unified Predictive Index. *Journal of Climate*, **30**, 9119-9131, https://doi.org/10.1175/JCLI-D-16-0825.1.

Kazantzidis, A., P. Tzoumanikas, A. F. Bais, S. Fotopoulos, and G. Economou, 2012: Cloud detection and classification with the use of whole-sky ground-based images. *Atmospheric Research*, **113**, 80-88, https://doi.org/10.1016/j.atmosres.2012.05.005.

Kemsley, S. W., P. Ceppi, H. Andersen, J. Cermak, P. Stier, and P. Nowack, 2024: A systematic evaluation of high-cloud controlling factors. *Atmospheric Chemistry and Physics*, **24**, 8295-8316, https://doi.org/10.5194/acp-24-8295-2024/.

Klein, S. A., 1997: Synoptic Variability of Low-Cloud Properties and Meteorological Parameters in the Subtropical Trade Wind Boundary Layer. *Journal of Climate*, **10**, 2018-2039, https://doi.org/10.1175/1520-0442(1997)010<2018:SVOLCP>2.0.CO;2.

Klein, S. A., A. Hall, J. R. Norris, and R. Pincus, 2018: Low-Cloud Feedbacks from Cloud-Controlling Factors: A Review. In: Pincus, R., D. Winker, S. Bony, and B. Stevens, (eds) Shallow Clouds, Water Vapor, Circulation, and Climate Sensitivity. Space Sciences Series of ISSI, vol 65. Springer, Cham. https://doi.org/10.1007/978-3-319-77273-8_7.

Koren, I., L. A. Remor, O. Altaratz, J. V. Martins, and A. Davidi, 2010: Aerosol-induced changes of convective cloud anvils produce strong climate warming. *Atmospheric Chemistry and Physics*, **10**, 5001-5010, https://doi.org/10.5194/acp-10-5001-2010.

Lam, R., and Coauthors, 2023: Learning skillful medium-range global weather forecasting. *Science*, **382**, 1416-1421, https://doi.org/10.1126/science.adi2336.

Li, Z., F. Niu, J. Fan, Y. Liu, D. Rosenfeld, and Y. Ding, 2011: Long-term impacts of aerosols on the vertical development of clouds and precipitation. *Nature Geoscience*, **4**, 888-894, https://doi.org/10.1038/ngeo1313.

Li, C., G. Tang, and Y. Hong, 2018: Cross-evaluation of ground-based, multi-satellite and reanalysis precipitation products: Applicability of the Triple Collocation method across Mainland China. *Journal of Hydrology*, **562**, 71-83, https://doi.org/10.1016/j.jhydrol.2018.04.039.

Lin, J.-L., and B. Mapes, 2004: Wind shear effects on cloud-radiation feedback in the western Pacific warm pool. *Geophysical Research Letters*, **31**, L16118, https://doi.org/10.1029/2004GL020199.

Loeb, N. G., and Coauthors, 2018: Clouds and the Earth's Radiant Energy System (CERES) Energy Balanced and Filled (EBAF) Top-of-Atmosphere (TOA) Edition-4.0 Data Product. *J. Clim*., **31**, 895-918, https://doi.org/10.1175/JCLI-D-17-0208.1. *Geophys. Res. Lett*., **48** (13), e2021GL093047, https://doi.org/10.1029/2021GL093047.

Loeb, N. G., G. C. Johnson, T. J. Thorsen, J. M. Lyman, F. G. Rose, and S. Kato, 2021: Satellite and Ocean Data Reveal Marked Increase in Earth's Heating Rate. *Geophys. Res. Lett*., **48**, e2021GL093047, https://doi.org/10.1029/2021GL090347.

Loeb, N. G., and Coauthors, 2024: Observational Assessment of Changes in Earth's Energy Imbalance Since 2000. *Surveys in Geophysics*, **45**, 1757-1783, https://doi.org/10.1007/s10712-024-09838-8.

Loveridge, J., and R. Davies, 2019: Cloud Heterogeneity in the Marine Midlatitudes: Dependence on Large-Scale Meteorology and Implications for General Circulation Models. *Journal of Geophysical Research Atmospheres*, **124**, 3448-3463, https://doi.org/10.1029/2018JD029826.

Naud, C. M., G. S. Elsaesser, and J. F. Booth, 2023: Dominant Cloud Controlling Factors for Low-Level Cloud Fraction: Subtropical Versus Extratropical Oceans. *Geophysical Research Letters*, **50**, e2023GL104496, https://doi.org/10.1029/2023GL104496.

Nielsen, J. K., M. J. Foster, and A. K. Heidinger, 2011: Tropical stratospheric cloud climatology from the PATMOS-x dataset: An assessment of convective contributions to stratospheric water. *Geophys. Res. Lett. Atmos*., **38**, L18801, https://doi.org/10.1029/2011GL049429.

Norris, J. R., and S. A. Klein, 2000: Low Cloud Type Over the Ocean from Surface Observations. Part III: Relationship to Vertical Motion and the Regional Surface Synoptic

Environment. *J. Climate*, **13**, 245-256, https://doi.org/10.1175/1520-0442(2000)013<0245:LCTOTO>2.0.CO;2.

Norris, J. R., and Coauthors, 2016: Evidence for climate change in the satellite cloud record. *Letter*, **536**, 72-75, https://doi.org/10.1038/nature18273.

Molling, C. C., A. K. Heidinger, W. C. Straka, and X. Wu, 2010: Calibrations for AVHRR channels 1 and 2: review and path towards consensus. *Int. J. Remote Sens.,* **31**,6519-6540, https://doi.org/10.1080/01431161.2010.496473.

Monod, A., and P. Carlier, 1999: Impact of clouds on the tropospheric ozone budget: Direct effect of multiphase photochemistry of soluble organic compounds. *Atmospheric Environment*. **33**, 4431-4446, https://doi.org/10.1016/S1352-2310(99)00210-1.

Massie, S. T., A. Heymsfield, C. Schmitt, D. Muller, and P. Seifert, 2007: Aerosol indirect effects as a function of cloud top pressure. *Journal of Geophysical Research Atmospheres*, **112**, D6, https://doi.org/10.1029/2006JD007383,

Matus, A. V., T. S. L'Ecuyer, 2017: The role of cloud phase in Earth's radiation budget. *J. Geophys. Res. Atmos*, **122**, 2559-2579, https://doi.org/10.1002/2016JD025951.

Matsui, T., H. Masunaga, R. A. Pielke Sr., and W.-K. Tao, 2004: Impact of aerosols and atmospheric thermodynamics on cloud properties within the climate system.

Myers, T. A., and J. R. Norris, 2016: Reducing the uncertainty in subtropical cloud feedback. *Geophysical Research Letters*, **43**, 2144-2148, https://doi.org/10.1002/2015GL067416.

Myers, T. A., R. C. Scott, M. D. Zelinka, S. A. Klein, J. R. Norris, and P. M. Caldwall, 2021: Observational constraints on low cloud feedback reduce uncertainty of climate sensitivity. *Nature Climate Change*, **11**, 501-507, https://doi.org/10.1038/s41558-021-01039-0.

Michelle L. M., J. T. M. Lenaerts, C. Shields, and J. D. Wille, 2022: Contribution of Atmospheric Rivers to Antarctic Precipitation. *Research Letters*, **49**, e2022GL100585, https://doi.org/10.1029/2022GL100585.

Myers, T. A., R. C. Scott, M. D. Zelinka, S. A. Klein, J. R. Norris, and P. M. Caldwall, 2021: Observational constraints on low cloud feedback reduce uncertainty of climate sensitivity. *Nature Climate Change*, **11**, 501-507, https://doi.org/10.1038/s41558-021-01039-0.

Ogunjobi, K. O., Y. J. Kim, and Z. He, 2004: Influence of the total atmospheric optical depth and cloud cover on solar irradiance components. *Atmospheric Research*, **70**, 209-227, https://doi.org/10.1016/j.atmosres.2004.01.003.

O'Neill, B. C., and Coauthors, 2016: The Scenario Model Intercomparison Project (ScenarioMIP) for CMIP6. *Geoscientific Model Development*, **9**, 3461, 3482, https://doi.org/10.5194/gmd-9-3461-2016.

Orbe, C., K. Wargan, S. Pawson, and L. D. Oman, 2020: Mechanisms Linked to Recent Ozone Decreases in the Northern Hemisphere Lower Stratosphere. *Journal of Geophysical Research Atmospheres*, **125**, e2019JD031631, https://doi.org/10.1029/2019JD031631.

Prabhakara, C., D. P. Kratz, J.-M. Yoo, G. Dalu, and A. Vernekar, 1993: Optically thin cirrus clouds: Radiative impact on the warm pool. *Journal of Quantitative Spectroscopy and Radiative Transfer*, **49**, 467-483, https://doi.org/10.1016/0022-4073(93)90061-L.

Ramanathan, V., R. D. Cess, E. F. Harisson, P. Minnis, B. R. Barkstrom, E. Ahmad, and D. Hartmann, 1989: Cloud-Radiative Forcing and Climate: Results from the Earth Radiation Budget Experiment. *Science*, **243**, 57-63, https://doi.org/10.1126/science.243.4887.57.

Ramanathan, V., and W. Collins, 1991: Thermodynamic regulation of ocean warming by cirrus clouds deduced from observations of the 1987 El Niño. *Nature*, **351**, 27-32, https://doi.org/10.1038/351027a0.

Rausch, J., A. K. Heidinger, and R. Bennartz, 2010: Regional assessment of microphysical properties of marine boundary layer cloud using the PATMOS-x dataset. *J. Geophys. Res.*, **115**, D23212, https://doi.org/10.1029/2010JD014468.

Riihelä, A., E. Jääskeläinen, and V. Kallio-Myers, 2024: Four decades of global surface albedo estimates in the third edition of the CM SAF cLoud, Albedo and Surface Radiation (CLARA) climate data record. *Earth System Science Data*, **16**, 1007-1028, https://doi.org/10.5194/essd-16-1007-2024.

Rosenfeld, D., and Coauthors, 2014: Global observations of aerosol-cloud-precipitation-climate interaction. *Reviews of Geophysics*, **52**, 750-808, https://doi.org/10.1002/2013RG000441.

Roeckner, E., U. Schlese, J. Biercamp and P. Loewe, 1987: Cloud optical depth feedbacks and climate modelling. *Nature*, **329**, 138-140, https://doi.org/10.1038/329138a0.

Saint-Lu, M., S. Bony, and J.-L. Dufresne, 2022: Clear-sky control of anvils in response to increased CO_2 or surface warming or volcanic eruptions. *npj Clim Atmos Sci*, **5**, 78, https://doi.org/10.1038/s41612-022-00304-z.

Schneider, T., T. Bischoff, and G. H. Haug, 2014: Migrations and dynamics of the intertropical convergence zone. *Nature*, **513**, 45-53, https://doi.org/10.1038/nature13636.

Schuddeboom, A. J., and A. J. McDonald, 2021: The Southern Ocean Radiative Bias, Cloud Compensating Erros, and Equilibrium Climate Sensitivity in CMIP6 Models. *J. Geophys. Res. Atmos*., **126**, e2021JD035310, https://doi.org/10.1029/2021JD035310.

Scott, R. C., T. A. Myers, J. R. Norris, M. D. Zelinka, S. A. Klein, M. Sun, and D. R. Doelling, 2020: Observed Sensitivity of Low-Cloud Radiative Effects to Meteorological Perturbations over the Global Oceans. *Journal of Climate*, **33**, 7717-7734, https://doi.org/10.1175/JCLI-D-19-1028.1.

Sekiguch, M. T. Nakajiman, K. Suzuki, K. Kawamoto, A. Higurashi, D. Rosenfeld, I. Sano, and S. Mukai, 2003: A study of the direct and indirect effects of aerosols using global satellite data sets of aerosol and cloud parameters. *Journal of Geophysical Research Atmospheres*, **108**, D22, 4699, https://doi.org/10.1029/2002JD003359.

Seneviratne, S. I., and Coauthors, 2021: *Weather and climate extreme events in a changing climate*. In: Masson-Delmotte, V. P., Zhai, A., Pirani, S. L. and Connors, C. (eds.) Climate Change 2021: The Physical Science Basis: Working Group I contribution to the Sixth Assessment Report of the Intergovernmental Panel on Climate Change. Cambridge University Press, Cambridge, UK, pp. 1513-1766.

Seo, J., C. Phillips, A. K. Heidinger, D. Loveless, and M. J. Foster, 2025a: Future Satellite-Based Cloud Climate Records: Intercomparison and Consistency between GAC and VGAC. Journal of Applied Meteorology and Climatology, https://doi.org/10.1175/JAMC-D-24-0132.1.

Seo, J., C. Phillips, A. K. Heidinger, and M. J. Foster, 2025b: Cloud changes over the tropical and mid-latitude ocean over the last four decades using PATMOS-x version 6.0. *Journal of Climate*, Accepted.

Seo, J., C. Phillips, A. K. Heidinger, and M. J. Foster, 2025c: Changes in cloud fractions over southeastern Pacific Ocean: cloud radiative effects and cloud controlling factors. *Journal of Climate*, Submitted.

Sherwood, S. C., 1999: On moistening of the tropical troposphere by cirrus clouds. *Journal of Geophysical Research Atmospheres*, **104**, 11949-11960, https://doi.org/10.1029/1999JD900162.

Sherwood, S. C., J.-H. Chae, P. Minnis, and M. McGill, 2004: Underestimation of deep convective cloud tops by thermal imagery. *Geophysical Research Letters*, **31**, L11102, https://doi.org/10.1029/2004GL019699.

Sherwood, S. C., and Coauthors, 2020: An Assessment of Earth's Climate Sensitivity Using Multiple Lines of Evidence. *Reviews of Geophysics*, **58** (4), e2019RG000678, https://doi.org/10.1029/2019RG000678.

Slingo, J. M., 1987: The Development and Verification of A Cloud Prediction Scheme For the ECMWF Model. *Quarterly Journal of the Royal Meteorological Society*. **113**, 899-927, https://doi.org/10.1002/qj.49711347710.

Slingo, A., J. M. Slingo, 1988: The response of a general circulation model to cloud longwave radiative forcing. I: Introduction and initial experiments. *Quarterly Journal of the Royal Meteorological Society*, **114**, 1027-1062, https://doi.org/10.1002/qj.49711448209.

Smith, C. J., and Coauthors, 2020: Effective radiative forcing and adjustments in CMIP6 models. *Atmospheric Chemistry and Physics*, **20** (16), 9591-9618, https://doi.org/10.5194/acp-20-9591-2020.

Stauffer, R. M., A. M. Thompson, L. D. Oman, and S. E. Strahan, 2019: The Effects of a 1998 Observing System Change on MERRA-2-Based Ozone Profile Simulations. *Journal of Geophysical Research Atmospheres*, **124**, 7429-7441, https://doi.org/10.1029/2019JD030257.

Stephens, G. L., 2005: Cloud Feedbacks in the Climate System: A Critical Review. *Journal of Climate*, **18**, 237-273, https://doi.org/10.1175/JCLI-3243.1.

Stowe, L. L., A. M. Ignatov, and R. R. Singh, 1997: Development, validation, and potential enhancements to the second-generation operational aerosol product at the National Environmental Satellite, Data, and Information Service of the National Oceanic and Atmospheric Administration. *Journal of Geophysical Research Atmospheres*, **102**, 16923-16934, https://doi.org/10.1029/96JD02132.

Stowe, L. L., P. A. Davis, and E. P. McClain, 1999: Scientific Basis and Initial Evaluation of the CLAVR-1 Global Clear/Cloud Classification Algorithm for the Advanced Very High Resolution Radiometer. *Journal of Atmospheric and Oceanic Technology*, **16**, 656-681, https://doi.org/10.1175/1520-0426(1999)016<0656:SBAIEO>2.0.CO;2.

Stowe, L. L., H. Jacobowitz, G. Ohring, K. R. Knapp, and N. R. Nalli, 2002: The Advanced Very High Resolution Radiometer (AVHRR) Pathfinder Atmosphere (PATMOS) climate dataset: Initial analyses and evaluations. *J. Climate*, **15**, 1243-1260, https://doi.org/10.1175/1520-0442(2002)015<1243:TAVHRR>2.0.CO;2.

Souza-Echer, M. P., E. B. Pereira, L. S. Bins, and M. A. R. Andrade, 2006: A Simple Method for the Assessment of the Cloud Cover State in High-Latitude Regions by a Ground-Based Digital Camera. *J. Atmos. Oceanic Technol.*, **23**, 437-447, https://doi.org/10.1175/JTECH1833.1.

Stenz, R., X. Dong, B. Xi, Z. Feng, and R. J. Kuligowski, 2016: Improving Satellite Quantitative Precipitation Estimation Using GOES-Retrieved Cloud Optical Depth. *Journal of Hydrometeorology*, **17**, 557-570, https://doi.org/10.1175/JHM-D-15-0057.1.

Stubenrauch, C. J., and Coauthors, 2013: Assessment of global cloud datasets from satellites: Project and database initiated by the GEWEX radiation panel. *Bull. Amer. Meteor. Soc.*, **94**, 1031-1049, https://doi.org/10.1175/BAMS-D-12-00117.1.

Sun, B., and Coauthors, 2015: Variability and Trends in U.S. Cloud Cover: ISCCP, PATMOS-x, and CLARA-A1 Compared to Homogeneity-Adjusted Weather Observations. *J. Climate*, **28**, 4373-4389, https://doi.org/10.1175/JCLI-D-14-00805.1.

Suzuki, S., J.-C. Golza, G. L. Stephens, 2013: Evaluating cloud tuning in a climate model with satellite observations. *Geophys. Res. Lett.*, **40**, 4464-4468, https://doi.org/10.1002/grl.50874.

Tan I. and T. Storelvmo, 2016; Sensitivity study on the influence of Cloud Microphysical Parameters on Mixed-Phase Cloud Thermodynamic Phase Partitioning in CAM5. *Journal of the Atmospheric Sciences*, **73**, 709-728, https://doi.org/10.1175/JAS-D-15-0152.1.

Tao, W.-K., J.-P. Chen, Z. Li, C. Wang, and C. Zhang, 2012: Impact of aerosols on convective clouds and precipitation. *Reviews of Geophysics*, **50**, RG2001, https://doi.org/10.1029/2011RG000369.

Taylor, K. E., M. Crucifix, P. Braconnot, C. D. Hewitt, C. Doutriaux, A. J. Broccoli, J. F. B. Mitchell, and M. J. Webb, 2007: Estimating Shortwave Radiative Forcing and Response in Climate Models. *Journal of Climate*, **20**, 2530-2543, https://doi.org/10.1175/JCLI4143.1.

Tselioudis, G., W. B. Rossow, F. Bender, L. Oreopoulos, and J. Remillard, 2024: Oceanic cloud trends during the satellite era and their radiative signatures. *Climate Dynamics*, **62**, 9319-9332, https://doi.org/ 10.1007/s00382-024-07396-8.

Vignesh, P. P., J. H. Jiang, P. Kishore, H. Su, T. Smay, N. Brighton, and I. Velicogna, 2020: Assessment of CMIP6 Cloud Fraction and Comparison with Satellite Observations. *Earth and Space Science*, **7**, e2019EA000975, https://doi.org/10.1029/2019EA000975.

Walther, A., and A. K. Heidinger, 2012: Implementation of the Daytime Cloud Optical and Microphysical Properties Algorithm (DCOMP) in PATMOS-x. *Journal of Applied Meteorology and Climatology*, **51**, 1371-1390, https://doi.org/10.1175/JAMC-D-11-0108.1.

Warren, S. G., C. J. Hahn, J. London, R. M. Chervin, R. L. Jenne, Colorado University, Boulder, CO, and National Center for Atmospheric Research, Boulder, CO, 1988: Global distribution of total cloud cover and cloud type amounts over the ocean. United States. https://doi.org/10.2172/5415329.

Weatherhead, E. C. and Coauthors, 1988: Factors affecting the detection of trends: Statistical considerations and applications to environmental data. *J. Geophys. Res. Atmos*., **103**, 17149-17161, https://doi.org/10.1029/98JD00995.

Weaver C., D. L. Wu, P. K. Bhartia, G. Labow, D. P. Haffner, L. Borgia, L. McBride, and R. Salawitch., and Coauthors, 2024: Comparison of Proxy-Shortwave Cloud Albedo from SBUV Observations with CMIP6 Models. *J. Clim*., **37**, 3093-3116, https://doi.org/10.1175/JCLI-D-23-0170.1.

Wetzel, M. A., and L. L. Stowe, 1999: Satellite-observed patterns in stratus microphysics, aerosol optical thickness, and shortwave radiative forcing. *Journal of Geophysical Research*, **104**, 31287-31299, https://doi.org/10.1029/1999JD900922.

Wild, M., D. Folini, C. Schar, N. Loeb, E. G. Dutto, and G. Konig-Langlo, 2013: The global energy balance from a surface perspective. *Climate Dynamics*, **40**, 3107-3034, https://doi.org/10.1007/s00382-012-1569-8.

Wodzicki, K. R., and A. D. Rapp, 2016: Long-term characterization of the Pacific ITCZ using TRMM, GPCP, and ERA-Interim. *J. Geophys. Res. Atmos.*, **121**, 3153-3170, https://doi.org/10.1002/2015JD024458.

Wong, J., M. C. Barth, and D. Noone, 2013: Evaluating a lightning parameterization based on cloud-top height for mesoscale numerical model simulations. *Geosci. Model Dev.*, **6**, 429-443, https://doi.org/10.5194/gmd-6-429-2013.

Wood, R., and C. S. Bretherton, 2006: On the relationship between stratiform low cloud cover and lower-tropospheric stability. *J. Clim.*, **19**(24), 6425-6432, https://doi.org/10.1002/2015GL063266.

Wu, W., Y. Liu, M. P. Jensen, T. Toto, M. J. Foster, and C. N. Long, 2014: A comparison of multiscale variations of decade-long cloud fractions from six different platforms over the southern Great Plains in the United States. *J. Geophys. Res. Atmos.*, **119**, 3438-3459, https://doi.org/10.1002/2013JD019813.

Wright, J. S., and Coauthors, 2020: Differences in tropical high clouds among reanalyses: origins and radiative impacts. *Atmospheric Chemistry and Physics*, **20**, 8989-9030, https://doi.org/10.5194/acp-20-8989-2020.

Xian, T. and C. R. Homeyer, 2019: Global tropopause altitudes in radiosondes and reanalyses. *Atmos. Chem. Phys*. **19**, 5661-5678, https://doi.org/10.5194/acp-19-5661-2019.

Yang, Q., Q. Fu, and Y. Hu, 2010: Radiative impacts of clouds in the tropical tropopause layer. *Journal of Geophysical Research Atmospheres*, **115**, D4, https://doi.org/10.1029/2009JD012393.

Yang, Y., D. Kiv, S. Bhatta, M. Ganeshan, X. Lu, and S. Palm, 2023: Diagnosis of Antarctic Blowing Snow Properties Using MERRA-2 Reanalysis with a Machine Learning Model.

Journal of Applied Meteorology and Climatology, **62**, 1055-1068, https://doi.org/10.1175/JAMC-D-23-0004.1.

Young S. A., and M. A. Vaughan, 2009: The Retrieval of Profiles of Particulate Extinction from Cloud-Aerosol Lidar Infrared Pathfinder Satellite Observations (CALIPSO) Data: Algorithm Description. *Journal of Atmospheric and Oceanic Technology*, **26**, 1105-1119, https://doi.org/10.1175/2008JTECHA1221.1.

Yuan, T., Z. Li, R. Zhang, and J. Fan, 2008: Increase of cloud droplet size with aerosol optical depth: An observation and modeling study. *Journal of Geophysical Research Atmospheres*, **113**, D4, https://doi.org/10.1029/2007JD008632.

Yuan, T., and Coauthors, 2023: Observational evidence of strong forcing from aerosol effect on low cloud coverage. *Science Advances*, **9**, 45, https://doi.org/10.1126/sciadv.adh7716.

Zeng, X., 1999: The Relationship among Precipitation, Cloud-Top Temperature, and Precipitable Water over the Tropics. *Journal of Climate*, **12**, 2503-2514, https://doi.org/10.1175/1520-0442(1999)012<2503:TRAPCT>2.0.CO;2.

Zhao, T. X. -P., P. K. Chan, and A. K. Heidinger, 2013: A global survey of the effect of cloud contamination on the aerosol optical thickness and its long-term trend derived from operational AVHRR satellite observations. *J. Geophys. Res. Atmos.*, **118**, 2849-2857, https://doi.org/10.1002/jgrd.50278.

Zhong, Y., M. Notaro, S. J. Vavrus, and M. J. Foster, 2016: Recent accelerated warming of the Laurentian Great Lakes: Physical drivers. *Limnol. Oceanogr.*, **61**, 1762-1786, https://doi.org/10.1002/lno.10331.

Zelinka, M. D., and D. L. Hartmann, 2011: The observed sensitivity of high clouds to mean surface temperature anomalies in the tropics. *Journal of Geophysical Research Atmospheres*, **116**, D23, https://doi.org/10.1029/2011JD016459.

Ziemke, J. R., and Coauthors, 2019: Trends in global tropospheric ozone inferred from a composite record of TOMS/OMI/MLS/OMPS satellite measurements and the MERRA-2 GMI simulation. *Atmos. Chem. Phys.*, **19**, 3257-3269, https://doi.org/10.5194/acp-19-3257-2019.

Zhu, S., Z. Xiao, H. Che, and Q. Chen, 2022: Impact of aerosols on warm clouds over the Sichuan Basin, China in winter based on the MERRA-2 reanalysis dataset. *Atmospheric Pollution Research*, **13**, https://doi.org/10.1016/j.apr.2022.101342.